Stirling Engine for Solar Thermal Electric Generation

Mike Miao He

Electrical Engineering and Computer Sciences
University of California at Berkeley

Technical Report No. UCB/EECS-2018-15
http://www2.eecs.berkeley.edu/Pubs/TechRpts/2018/EECS-2018-15.html

May 1, 2018

Acknowledgement

I would like to thank Professor Seth Sanders for his mentorship and helping me to be a better engineer, for his perpetual good humor and kindness, and for always being available for his students.

I would also like to thank Artin Der Minassians for his guidance and help. Thanks to Aron, Matt, Roger, Sarah, and Shai on the Cleantech-to-Market team for their research on the market viability of the technology. Thanks to Alan, Shong, Kelvin, Alex, and Samir and others for their help.

Stirling Engine for Solar Thermal Electric Generation

by

Mike Miao He

A dissertation submitted in partial satisfaction of the

requirements for the degree of

Doctor of Philosophy

in

Engineering – Electrical Engineering and Computer Sciences

and the Designated Emphasis

in

Energy Science and Technology

in the

Graduate Division

of the

University of California, Berkeley

Committee in charge:

Professor Seth Sanders, Chair
Professor Randy Katz
Professor Dan Kammen

Summer 2016

Stirling Engine for Solar Thermal Electric Generation

Abstract

Stirling Engine for Solar Thermal Electric Generation

by

Mike Miao He

Doctor of Philosophy in Engineering – Electrical Engineering and Computer Sciences

University of California, Berkeley

Professor Seth Sanders, Chair

Addressing the challenge of climate change requires the large-scale development of significant renewable energy generation, but also requires these intermittent energy sources to be balanced by energy storage or demand management to maintain a reliable electric grid. In addition, a centralized generation paradigm fails to capture and utilize thermal energy for combined heat and power, abandoning a large portion of the available value from the primary energy source. A solar thermal electric system utilizing Stirling engines for energy conversion solves both of these shortcomings and has the potential to be a key technology for renewable energy generation. The ability to store thermal energy cheaply and easily allows the reliable generation of output power even during absences of solar input, and operating as distributed generation allows the output thermal stream to be captured for local heating applications. Such a system also can achieve relatively high conversion efficiencies, is fabricated using common and benign materials, and can utilize alternate sources of primary energy in an extended absence of solar input.

This dissertation discusses the design, fabrication, and testing of a Stirling engine as the key component in a solar thermal electric system. In particular, the design addresses the low temperature differential that is attainable with distributed solar with low concentration ratios and is designed for low cost to be competitive in the energy space. The dissertation covers design, fabrication, and testing of a 2.5 kW Stirling Engine with a predicted thermal-to-mechanical efficiency of 20%, representing 60% of Carnot efficiency, operating between 180 °C and 30 °C. The design process and choices of the core components of the engine are discussed in detail, including heat exchangers, regenerator, pistons, and motor/alternator, and the process for modeling, simulation, and optimization in designing the engine. Finally, the dissertation covers the assembly and experimental testing that validates the design in terms of heat exchanger performance, losses, kinematics, and cycle work.

To my wife, Michelle, for loving me and supporting me throughout my graduate career.

Contents

List of Figures

List of Tables

Acknowledgments

I would like to thank Professor Seth Sanders for his mentorship and helping me to be a better engineer, for his perpetual good humor and kindness, and for always being available for his students.

I would also like to thank Artin Der Minassians for his guidance and help. Thanks to Aron, Matt, Roger, Sarah, and Shai on the Cleantech-to-Market team for their research on the market viability of the technology. Thanks to Alan, Shong, Kelvin, Alex, and Samir and others for their help.

Chapter 1

Introduction

Renewable energy is the cornerstone of humankind's urgent endeavor to address the climate change challenge on the technological front. The revolution of fossil energy enabled great advances in technology and society, but precipitated calamitous effects on the environment. To continue the pace of growth enabled thus far by plentiful energy, a new revolution will have to be made toward clean and sustainable sources of power. Such a transition is the inevitable next step in the production of energy - the only question is the magnitude of accrued harm before it occurs.

To address this challenge, all forms of renewable energy should be explored and developed. Solar photovoltaic and wind power already have achieved a high profile and extraordinary improvements in cost and technology. Solar thermal generation has had less development and the technology is less mature, despite possessing a set of potentially crucial advantages, such as energy storage, combined heat and power, and potentially low-cost. This dissertation will discuss the design and development of a prototype Stirling engine for solar thermal energy conversion.

In this research, a full-power single phase Stirling engine prototype was designed, fabricated, and tested. This research builds on previous work in [22] on low-power single and multiphase prototypes. The primary goals were to demonstrate the technical performance and feasibility of this Stirling engine technology for use in commercial energy applications and to validate the design methodology to provide a path for future development.

1.1 System Description

The Stirling Engine is the central component of a distributed combined heat and power system envisioned in this research. The system as conceived is suitable for residential-scale power generation and incorporates energy storage to produce consistent output power from variable solar resources. The rejected heat from the engine can be used for local heating needs, which further improves the total system efficiency.

A diagram of the solar thermal system is shown in Figure 1.1. The key components of the system include a passive solar collector, a hot thermal storage subsystem, the Stirling engine described herein, and an optional waste heat capture component. The system is designed with evacuated tube solar collectors in mind, as they provide the highest temperature input heat and efficiency of inexpensive commercially available collectors. The collectors are non-tracking to reduce component count and lower cost, though passive concentrators were added and tested to improve efficiency. Alternatively, on-site combustion can be used as a thermal energy source in the absence of, or to balance, solar energy. The thermal energy storage system can be realized with inexpensive hot water tanks that are commonly used in residiential settings. Additional components include piping, fluid pumps, and heat exchangers for transferring heat between components and streams.

The majority of the system is designed to be composable from commercially available components to reduce cost and for simplicity. The exception to this is the Stirling engine, which requires significant engineering to achieve high performance at low cost. The Stirling engine is the central component of the system and is the focus of this dissertation.

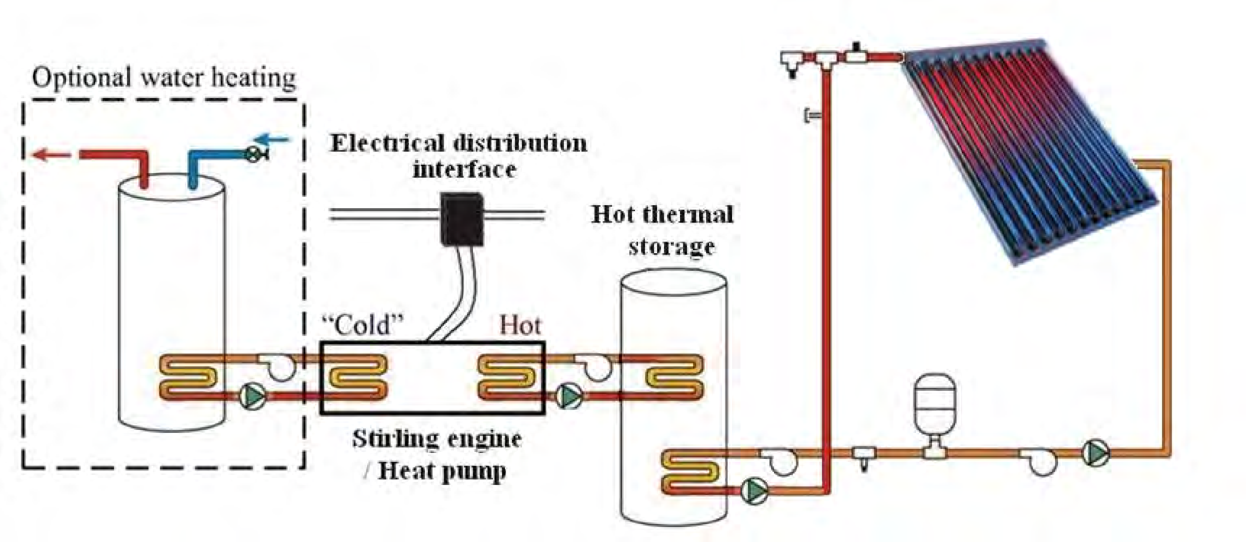

Figure 1.1: System Diagram

1.2 Stirling Engine Background

The Stirling engine is a heat engine that utilizes the Stirling Cycle to convert thermal energy flux into mechanical energy. The engine can also be run in reverse as a heat pump, which causes the inverse conversion. The Stirling Cycle is closed-cycle, which means that the internal working fluid is retained and isolated from the external energy source. This then requires heat exchangers to transfer thermal energy from an external hot-side source into the engine and from the engine to an external cold-side sink.

The Stirling Cycle is a thermodynamic cycle, and as such, is limited in efficiency by the Carnot Efficiency, given in Equation 1.1:

$$\eta = 1 - \frac{T_C}{T_H} \tag{1.1}$$

where η is the maximum theoretical efficiency, T_C is the temperature of the cold-side reservoir, and T_H is the temperature of the hot-side reservoir.

As a gas cycle, the Stirling Cycle is usefully characterized by a P-V diagram, a plot of the internal pressure versus internal volume over a single cycle of the engine. An illustrative P-V diagram is shown in Figure 1.2.

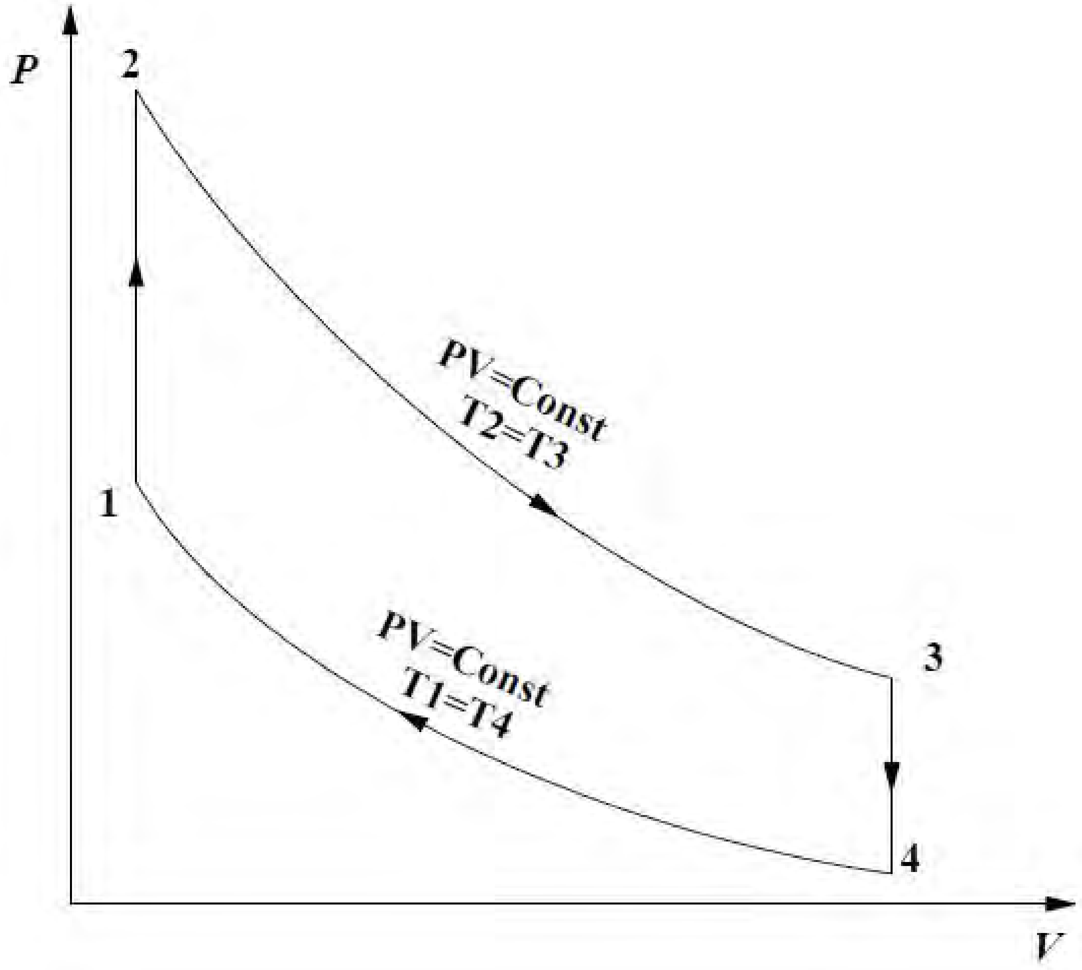

Figure 1.2: Ideal Stirling Cycle P-V Diagram

In the ideal P-V diagram, the trajectory of the engine is modeled as travelling along four ideal curves. These are shown in Figure 1.2 as a progression from point 1 → 2 → 3 → 4 → 1.

These four segments can be described as follows. 1 → 2 is an isometric (equal volume) step wherein the enthalpy of the internal working fluid is increased by displacing gas through the hot-side heat exchanger and therefore imparting heat from the external high temperature source, all while keeping volume constant. The pressure increases during this step due to the Ideal Gas Law. 2 → 3 is an isothermal expansion step wherein work is performed by expanding the internal working fluid, typically in a cylinder-piston subsystem. The temperature is kept constant by heat exchange with the high temperature source. 3 → 4 is another isometric step wherein the enthalpy of the internal working fluid is descreased by displacing gas to the engine cold-side, while volume is kept constant. Finally, 4 → 1 is an isothermal contraction wherein work is performed on the internal working fluid to compress it, typically from the same piston that carried out the expansion earlier.

This represents a highly simplified and idealized description of the thermodynamic processes in a Stirling Cycle. In reality, several important deviations from the prior description must be noted. First, it is vastly more efficient to transfer the enthalpy of the working fluid to a regenerator in step 3 → 4, which is then returned to the working fluid in step 1 → 2. The regenerator is an important component of all real Stirling engines and is necessary for achieving high efficiency. Second, the discrete steps outlined are not traversed in disjoint timeframes, rather the real trajectory of the engine will simultaneously undergo two adjacent processes at each point in time. This leads to an actual P-V curve that resembles an inscribed ellipse within the idealized curves shown in Figure 1.2. Third, the processes themselves are not ideal; for example, there is no practical implementation of a truly isothermal process. In reality, that step is more accurately modeled by an adiabatic process, wherein the enthalpy of the working fluid remains constant.

Given this description of the Stirling Cycle, the Stirling engine is then a mechanical embodiment of the cycle. A Stirling engine can be realized in multiple different ways, but the most common form includes two pistons, hot-side and cold-side chambers and heat exchangers, and a regenerator. One of the pistons is denoted the displacer piston, and is nominally responsible for driving the internal working fluid between the hot and cold chambers during the isometric steps. The other piston is denoted as the power piston, and is nominally responsible for the adiabatic expansion and compression of the working fluid. The hot and cold chambers and heat exchangers serve to allow thermal flux between the working fluid and the external hot and cold sources, respectively. The regenerator is responsible for recapturing enthalpy during one part of the cycle and reimparting that enthalpy back to the working fluid on the opposite half of the cycle. This configuration is a typical embodiment of a Stirling engine, and is in fact the configuration that was developed in this research. It should also be noted that an electric machine is required for conversion between the kinetic energy developed by the engine and electrical energy, and this component is also part of this research.

A detailed discussion of the design and characterization of the components, loss terms, and non-idealities will be presented in Chapter 3.

Chapter 2

Motivation

This chapter will discuss the motivation behind this research into Stirling engines for thermal energy conversion. Additional context on renewable energy and energy storage will be covered, and then discuss potential benefits of this research on the field.

2.1 Broader Context

The endeavor of transforming the world's energy portfolio from fossil-fuel generation to renewable generation in order to mitigate climate change is one of the biggest challenges of the 21st century. Significant technological and societal advances will need to be made in addition to the extensive progress already achieved. Toward this goal, the Stirling engine system proposed in this dissertation offers compelling advantages over many other technologies.

Over the past decade, renewable energy has undergone a period of rapid growth in technology, cost-competitiveness, and production both domestically and worldwide. Not so long ago, renewable energy was considered by many to be prohibitively expensive and impractical as a bulk solution to clean energy. Since then, wind and solar energy have seen exponential growth in installed capacity and continuous decline in prices. Solar photovoltaics are a compelling example, and are also the most direct comparison to the solar thermal technology proposed herein.

The price of solar photovoltaics has plummeted in recent years, driven by a combination of growth in silicon production from China, improvements in fabrication and installation of panels, and changes in business practices such as aggressive vertical integration in pursuit of lower costs. The median installed price of residential solar panels has dropped from \$9.1/W in 2006 to about \$4.3/W in 2014, and non-residential solar prices have dropped from \$8.8/W in 2006 to \$3.9/W for small systems (less than 500kW) and from \$7.8/W to \$2.8/W for large systems (greater than 500kW) [3]. Over this same period of time, falling prices have spurred growth in annual installed capacity from about 110.8 MW in 2006 to about 2380.8 MW in 2014 in the United States alone, with a domestic cumulative capacity of 9392.1 MW [3]. Even then, U.S. still ranks fourth in worldwide solar capacity, with Germany, Italy, and China leading. In 2014, worldwide installed capacity reached 178 GW, with 41 GW being added in 2014 alone [26], and this growth shows no signs of slowing.

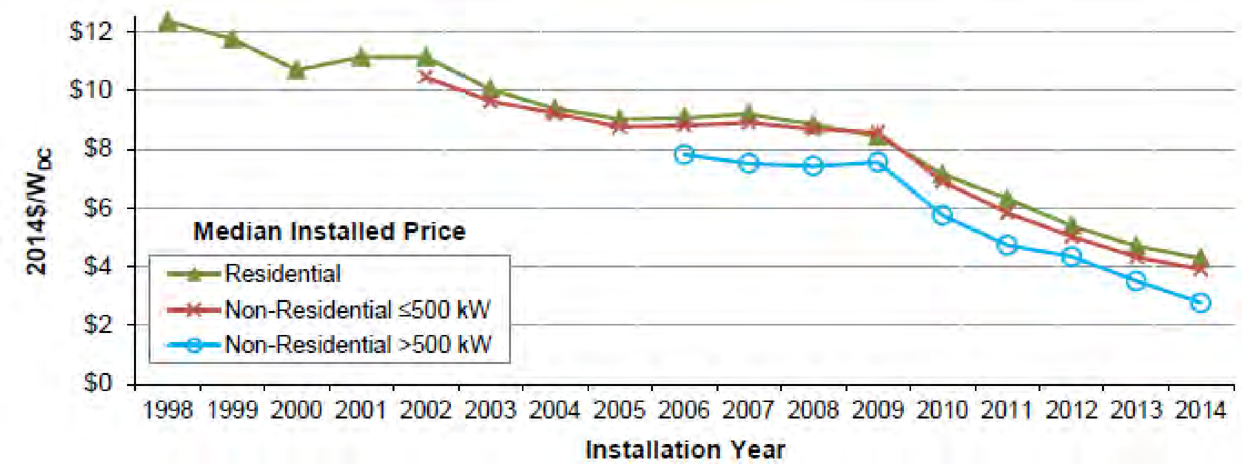

Figure 2.1: Solar photovoltaic installed price in the United States [3].

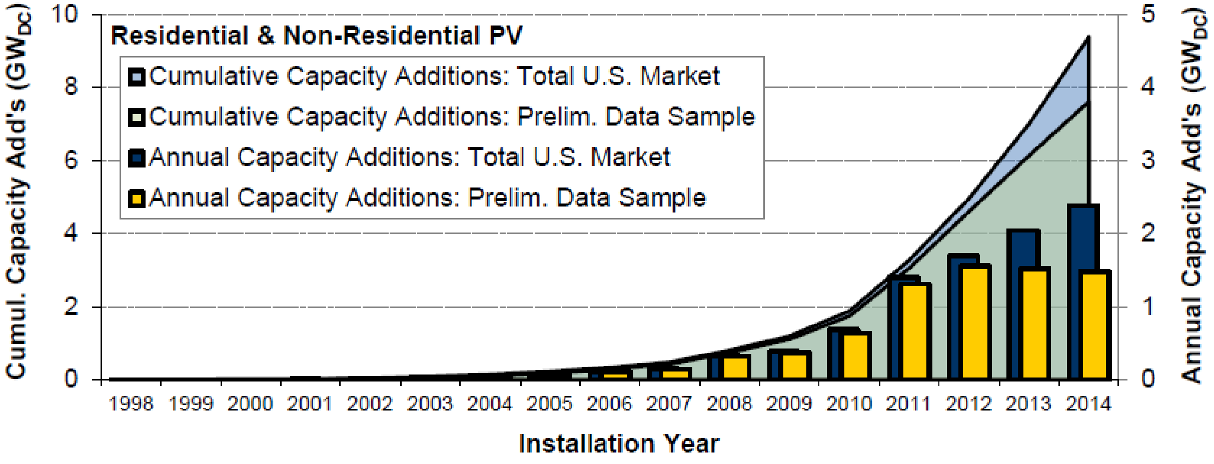

Figure 2.2: Solar photovoltaics annual and cumulative installed capacity by year in the United States since 1998 [3].

With the solar photovoltaic industry already expanding and maturing, it is necessary to motivate the development of solar thermal energy as a compelling alternative technology. To that end, there are a number of fundamental technological advantages offered by solar thermal technology over solar photovoltaics, chief of which is the ability to easily store energy. The primary energy of renewable sources is fundamentally tied to intermittent and variable processes, such as sunlight and wind. As the installed capacity of such renewables grows, so does the degree of uncontrollable and unpredictable generation on the grid. The forthcoming need for energy storage has been widely recognized as a counterbalance to this increasing variability. This energy storage can either come in the form of independent installations of electrical storage systems, such as batteries and flywheels; or it can be derived from developing renewable energy sources that are inherently coupled with energy storage, such as the Stirling engine solar thermal system.

Energy storage in a solar thermal system turns an unreliable resource into a reliable source of electricity, and does so at low cost, low complexity, and fully integrated into installation. Additionally, solar thermal also carries other important benefits, including the simplicity of components and conventionality of fabrication, which would aid in cost-competitiveness and bypassing production bottlenecks and supply chain issues; the potential for combined heat and power, which could significantly increase overall thermal efficiency; and application as a distributed generation system, fulfilling a role not available to technologies that rely on the scale of centralized installations. These motivations will be discussed in further detail.

Energy Storage

As renewable energy achieves higher penetration on the modern electric grid, the intermittency and variability in solar and wind energy become a more significant challenge that must be addressed by the industry. The underlying operation of the electric grid relies on instantaneously fulfilling demand with regulated generation. The addition of large amounts of uncontrollable generation serves to break this contract, upending the way that the grid has operated since the beginning. A certain amount of control must be present in the grid to maintain stability, so this gives rise to two fundamentally different but complementary approaches to integrating renewables.

The first is to add controllable compensation on the supply side in the form of energy storage or responsive fossil fuel generation. This addresses the challenge while serving to keep the existing structure of supply-side control intact - good energy storage would be invisible to the consumer. The second approach is to add controllability and responsiveness to the demand side of the grid. This has the advantage of utilizing the existing untapped flexibility of the demand side to perform the same function of balancing supply and demand, but challenges the entrenched paradigm of supply side control, and requires the introduction of pervasive intelligence and actuation on the demand side[11].

Most likely, both energy storage and controllable demand will be employed to aid in the process of renewable integration. The Stirling engine system as envisioned is potentially a mixture of these two approaches. It incorporates energy storage to produce reliable power generation, but since it is a distributed system designed to be co-located with demand, it can also autonomously balance load on the demand side. This carries advantages over either approach employed independently - the storage available can balance both local generation and demand simultaneously. The technology is also attractive simply due to the fact that it is generation with built-in storage. This enables grid integration with minimal effect on grid stability.

The energy storage potential of the Stirling engine system is a major compelling feature when compared to photovoltaic solar, and dramatically improves its competitiveness. The overall necessity for more storage is unequivocal and unambiguous in the industry, and it is quickly moving to incentivize and demand installation of storage. Examples include mandates for rapid expansion of energy storage capacities, such as California's AB 2514, which as directed by the CPUC will mandate procurement of 1,325 MW of energy storage capacity by the year 2020 [27], which almost doubles worldwide non-hydro storage [24] and is over 50 times California's current installed storage capacity [25].

A Stirling-engine based thermal system contributes in two ways to the storage challenge. First, as a generation technology, its power output is reliable and consistent, presenting it as a technology that does not require additional balancing from storage. Indeed, it is flexible and controllable in its power output, both on short time scales of seconds by varying the frequency of the engine, or on longer time scales of minutes to hours by varying input thermal energy. Second, the Stirling engine process is reversible, allowing it to be used as a pure energy storage mechanism by driving it in heat pump mode from grid energy, then later discharging stored energy in generation mode. In general, deriving a specific monetary value from these advantages is difficult, depending on a number of factors including market structure, composition of generation sources, load profiles, and factors particular to a region. As a reference, NREL estimates that the value of electricity from a utility scale solar thermal is 2.57 times that of electricity from a solar photovoltaic plant given a 40% Renewable Portfolio Standard [15]. This comparison probably cannot be extrapolated directly to the Stirling engine system, but points toward a significant value in reliable generation.

The energy storage market for non-hydro technologies is still relatively young and growing. Energy storage mandates in the public sphere have been typically agnostic of technologies, leaving room for a system such as the Stirling engine solar thermal system to participate. However, typical market structures do not easily accomodate or incentivize a distributed storage and generation technology such as this one. Renewable generation, such as photovoltaics, have mandated incentive structures, such as net metering, that do not provide additional incentives for the reliability of the source, hindering the ability of the consumer to capture the value of storage. However, there are signs that this market structure is changing in recognition of the costs and challenges of the ever-growing share of renewable generation. For instance, PG&E is offering an incentive of up to $1.31/W for generation installations that have energy storage included [7]. Net metering programs have also faced significant challenges in recent years across multiple states, such as Nevada, Maine, Arizona, Hawaii, and California, partly as response to the hidden costs of providing a reliable grid when distributed PV is incentivized with retail electricity rates. A Stirling engine solar thermal system could alleviate some of these tensions between utilities and solar developers by introducing ubiquitous energy storage along with the generation capacity.

One challenge is that monetization of the energy storage component of the Stirling engine system, apart from just providing firm capacity, is difficult in the current market structure. Energy storage is typically procured in the form of large centralized installations, and participates in markets in order to sell storage services such as regulation, load balancing, and reserves. Behind-the-meter energy storage is starting to gain some presence, especially since AB 2514, but is still in its infancy. Storage in the form of a Stirling engine system would have a difficult time participating economically in energy markets in a consistent way across all service territories. As such, the economic value of energy storage from the proposed Stirling engine system would be greatly enhanced if market structures were more universally supportive of distributed storage. This does not diminish the value of research into such a system, however, both in anticipation of market changes and for the intrinsic value from development of a technically advantageous technology.

Combined Heat and Power

Combined heat and power refers to the generation of useful thermal energy in addition to electricity. Combined heat and power enhances the value proposition from any particular technology by utilizing the thermal output of the system, an additional value stream that is typically wasted or underutilized. It is particularly attractive for a thermal-based system, since conversion from thermal energy to electricity requires the rejection of heat as determined by the fundamental laws of thermodynamics.

The benefit derived from the supplementary thermal stream contributes to higher efficiency of the overall system by displacing energy otherwise needed for thermal services. This avoided energy use also provides another revenue stream and improves the economic proposition of the system. Accounting for the impact on efficiency of the supplementary thermal stream in CHP systems must be carefully done. There are in fact two measures of efficiency that can be calculated - an overall system efficiency (thermal efficiency), and an effective electrical efficiency. The two measures of efficiency have different uses. The overall system efficiency is more straightforward and measures the fraction of useful energy produced versus the energy consumed by the system. The effective electrical efficiency is useful to compare a CHP system with other forms of power generation without CHP. As a formula, the overall system efficiency is given by

$$\eta_O = \frac{W_E + \sum Q_O}{Q_I} \tag{2.1}$$

where W_E is the electrical power output of the system, Q_O are the useful thermal outputs of the system, and Q_I is the energy of the total thermal energy input. This measures the total useful output from the system compared to the energy input, and is well-suited for understanding how well the system makes use of its inputs.

The second measure of efficiency, the effective electrical efficiency, is given by the following formula:

$$\eta_E = \frac{W_E}{Q_I - \sum \frac{Q_O}{\alpha}} \tag{2.2}$$

where W_E is the electrical power output of the system, Q_O are the useful thermal outputs of the system, and Q_I, and α is the conversion efficiency of the displaced technology for each usage of the thermal output. For example, α might be the efficiency of a water heater if the output thermal stream serves to heat water. This measure of efficiency accounts for the value of the thermal stream as avoided input energy, taking into account the efficiency of the avoided energy. Therefore, replacing an inefficient end-use of thermal energy is more effective than replacing an efficient one. This measure of efficiency is more useful for direct comparison with other forms of power generation, since it fully accounts for the differences in energy usage due to avoidance between the forms of generation being compared.

Utilizing the thermal stream makes for a very favorable comparison between CHP thermal systems and other systems. For the particular system described herein, which has a conversion efficiency of 20%, these efficiency values can be calculated. If a very conservative estimate is made that 50% of the rejected waste heat can be captured for water heating, this leads to a total system efficiency of 60%. Given that conventional water heaters are approximately 80% - 90% efficient, this would lead to an effective electrical efficiency of 36% - 40%, a value that is significantly better than other renewable technologies and competitive with centralized power generation.

Distributed Generation

Distributed generation is an area with a high potential of growth. By 2020, installed capacity of distributed generation is predicted to reach 15 to 20 GW [5]. Distributed generation conveys several important advantages as well as disadvantages versus centralized power generation. These advantages include the ability to use rejected heat for onsite CHP, reduction in transmission and distribution losses and capacity, and microgrid or islanding capability. The chief disadvantage is the possibility of poor scaling of the technology down to small scale and the lack of economies of scale with respect to manufacturing and deployment. Applied to Stirling engine technology, however, the advantages are highly relevant, while the disadvantages are less adverse, leading these considerations to favor distributed generation for this technology.

Centralized power generation is highly limited in its ability to utilize rejected heat, due to the fact that large power plants are typically not co-located with demand for thermal energy. This energy stream is almost always simply dissipated to the environment, and furthermore is dissipated by consuming large quantities of water. According to [17], electricity generation in 2012 in the United States produced 12.4 Quad of electricity for 25.7 Quad of rejected heat, representing an overall system efficiency of only 32.5%.. If this thermal energy could be utilized in a consistent manner, the overall system efficiency of electric generation could be dramatically improved. This is one of the most important rationale for distributed generation. However, certain technologies are better suited than others for combined heat and power. Since the Stirling engine is a heat engine, it fundamentally must reject heat in order to generate work according to the laws of thermodynamics. This heat is also typically rejected via a thermal fluid stream, rather than dissipatively to the environment. This makes it a good candidate for combined heat and power, especially at the lower input temperatures that are targeted by this project, which necessitate a higher fraction of rejected heat.

The second major advantage of distributed generation is that transmission of power is obviated. This both reduces losses due to transmission inefficiencies and reduces the load on the transmission system. According to the U.S. Energy Information Administration [1], 7% of transmitted energy is lost due to the transmission and distribution system. Distributed generation does not incur this penalty. Perhaps more importantly, expansion of utility-scale intermittent renewable energy will add significantly to transmission and distribution requirements. Capacity of the T&D system must be sized for peak power, not average power, which leads to poor utilization of the capital investment in the grid. The energy storage capabilities of the Stirling engine system help to reduce this burden on transmission and distribution - a controllable and reliable generation source requires less power transfer from the grid than a source that adds to variability. Energy storage also aids in microgrid or islanding capabilities - when there is no stable grid, a generation source with reliable power is extremely beneficial. The alternative is to install fuel-based generation or expensive standalone energy storage systems, such as batteries, to provide reliability.

The main disadvantages of distributed generation are due to scaling. Many technologies, including Rankine cycle or Brayton cycle machines, scale very well upwards, with larger machine size, but scale poorly down to smaller machine sizes. The opposite tends to be true for Stirling engines - they operate at relatively high efficiencies at smaller scales corresponding to distributed generation levels, but do not scale to larger sizes as well. This is primarily due to the difficulty of delivering thermal energy through a heat exchanger as length scales are increased. Note that this scaling discussion refers to changing efficiencies at different power levels for a single machine; Stirling engines could certainly be combined in parallel to achieve higher total power ratings instead of increasing the size of a machine, but this simply scales power linearly and does not improve the overall efficiency in fundamental ways. A technical discussion of scaling of Stirling engines is given in Section 3.9. In contrast, Brayton or Rankine cycles are more efficient as the engine size is scaled up. Therefore, the size and power levels of distributed generation tend to play towards a strength of Stirling generation, namely better efficiency at smaller scales.

Distributed generation is furthermore better suited for electrification in the developing world, compared to large-scale centralized power. In many places, long distance transmission and distribution systems are in poor quality or non-existent, and development of significant T&D capability can be prohibitively expensive. In these cases, distributed generation within microgrids presents a more likely path forward for electrification. Generation units on the scale of a few homes to small neighborhoods are well-suited for these purposes.

2.2 Applications

The Stirling engine's flexibility with respect to thermal input allows the technology to be readily used for multiple types of applications. This section will discuss specific applications and how the previously outlined advantages contribute to the value of the system. Certain combinations of applications can be fulfilled with a single design, though others require a certain amount of redesign and sacrifices to achieve high performance. Two of the most promising applications for the technology will be covered - distributed generation and diesel cogeneration - along with prospects for commercialization and additional design considerations for these applications. Since Stirling engine technology is relatively sparse in most of these application spaces, the discussion is necessarily somewhat speculative.

Distributed solar generation

The original intended application for the Stirling engine system was distributed solar generation. The primary competing technology in this space is rooftop photovoltaics. Photovoltaic technology has major commercial advantages in the forms of industry adoption, manufacturing infrastructure, public familiarity, targeted financing programs, and low cost through maturation on a learning curve. It also has major technical advantages including the simplicity of the technology compared to Stirling - in particular, the absence of plumbing and heat exchangers - and the potential for higher electrical conversion efficiency. These are steep advantages to overcome if distributed Stirling systems are to achieve penetration in the same market segment.

The proposition for Stirling systems in this application space therefore presumes two key factors - that energy storage and combined heat and power will become important advantageous features. As discussed previously, energy storage may become an important enabler and prerequisite for high levels of renewable generation from intermittent primary energy sources. This may manifest concretely in the form of regulations or financial incentives that promote energy storage with distributed generation. Additionally, there may be consumer demand for reliable renewable power for certain customers or end-uses. The ability to fully power one's home without drawing from the grid, including during cloudy weather or at night, can be an appealing feature. Industrial or commercial facilities that wish to employ renewable energy may find reliable generation sources much more appealing for critical applications, or for financial reasons like avoiding high demand charges. Possibly more importantly, the ability to generate reliable power is extremely relevant to electrification in the developing world.

Likewise, the combined heat and power capabilities of the Stirling system add value by displacing a certain amount of thermal energy consumption, such as natural gas heating. This could allow users to fully supply their energy needs without purchasing any energy services from a utility, given proper design and sizing of the system components for the particular building. Two considerations should be noted. The first is that the ratio of thermal output to electric output of the Stirling system is typically higher than the ratio of thermal demand to electric demand in a typical modern U.S. household. [23] Excess thermal output can also be more effectively utilized by redesigning certain energy services. Heat can be used for cooling and refrigeration by use of absorption chillers, for example. The second is that thermal energy demand can vary greatly based on climate; such a system may be well suited to particular locations and seasons but poorly suited to others.

Though PV systems can have battery storage systems installed, this is typically prohibitively costly, especially on a distributed scale. For combined heat and power, PV systems can be fitted with heat capture technology, which also serves to improve the performance of the PV cells by lowering their temperature. [23] However, this adds additional cost, and the quality and quantity of thermal energy recoverable is not comparable to Stirling engine system. To offer the complete feature set that the Stirling engine system offers, PV systems lose their cost-competitiveness while still not equaling Stirling systems in each area. However, it is important to point out that the two technologies are not mutually exclusive; Stirling systems may cover important niches where energy storage and thermal output are valuable features, while photovoltaics continue to dominate in more typical applications.

Central to the market potential of the Stirling engine system is its cost. Since a full-scale prototype was fabricted in the course of this project, a final production cost for the engine and system can be predicted with a reasonable amount of accuracy. This is based on a combination of costs for commercially available components and predictions for costs of custom-machined components at higher production quantities. To determine the economic viability of the Stirling engine technology, the costs and price of the 2.5 kW system were evaluated. Table 2.1 lists component prices for manufacturing the Stirling engine at moderate scale. For commercially-available components, costs are taken by averaging the top 10 vendors for that component. For custom machined components, the costs are quoted from machine shops. The balance of system is estimated at 40% of total engine cost, a typical value for this type of machine. A 30% margin is also accounted for, given by the industry practice for small generators or turbines. This gives the final price of \$3.10/W for the 2.5 kW engine.

The Stirling engine must be compared to a comparable distributed photovoltaic system to gain insight into its market competitiveness. Table 2.2 gives a comparison between distributed Stirling generation, as laid out in this dissertation, compared to distributed photovoltaic generation. The capital price of the Stirling system from Table 2.1 is entered on the first line in this table. The price of PV panels listed is the 2014 median price for installations under 10 kW [3]. Additionally, the Stirling system requires the purchase of commercially-available evacuated tube collectors, which has been priced at \$0.70/W by directly talking to suppliers. This component does not apply to PV panels, which perform both functions of collection and conversion. PV installations have both a module-price component, which is listed in the first line, and non-module balance of system prices. The balance of system includes inverters, mounting hardware, labor, permitting and fees, overhead, taxes, and installer profit. The balance of system costs for the Stirling engine system are remarkably similar - each of these components are likewise necessary. The installation of collectors on the rooftop is parallel to the installation of the PV panels themselves. Additionally, the installation of the engine itself, along with plumbing, storage tanks, and pumps are necessary for the Stirling engine. These additional costs were included in the price of the engine previously, in Table 2.1. Therefore, balance of system costs for PV installations are good proxies for the remaining balance of system for Stirling systems, and are assumed to be the same in this analysis.

Hardware Components	Cost per engine	$ per watt
Alternator	$245	
Crankshaft	$250	
Piston Lubrication	$10	
Heat Exchanger Mesh	$50	
Custom Machined Components	$1372	
Other Components	$1400	
Assembly (20hrs $20/hr)	$400	
Shipping	$30	
Pressure Vessel	$500	
Engine Total	$4257	$1.70
	Balance of System	$0.70
	30% margin	$0.70
	Final Price	$3.10

Table 2.1: Breakdown of engine capital costs for Stirling engine converter [16].

Component	Stirling Engine	Distributed PV [3]
Engine System	$3.10/W	$0.70/W
Collector	$0.70/W	
Balance of System	$3.60/W	$3.60/W
Total	$7.40/W	$4.30/W

Table 2.2: Installed price comparison between distributed Stirling system and distributed PV system [3]. Balance of System includes all non-module prices in an installation, and is assumed to be the same between the systems.

As can be seen in this table, the Stirling engine system is not cost competitive with modern distributed photovoltaic systems on this basis alone. In 2006, at the beginning of this project, distributed solar PV module prices were approximately \$4/W, leading to a installed cost of \$8.60/W. This made for a much more favorable comparison, especially with the additional benefits of energy storage and combined heat and power. Additionally, PV is continuing its aggressive reduction in prices year after year. For example, from 2011 to 2012, installed PV prices fell by \$0.90/W (14%). As it stands currently, the Stirling engine system is not a viable competitor for direct generation on this basis. However, this is method of comparison does not capture all the value streams in a Stirling engine, since the Stirling system is more feature rich than the PV system, incorporating CHP and energy storage.

A more favorable, and more technologically even, comparison is given by including the benefits from energy storage and CHP. Energy storage can be accounted for by including the price of a commensurate battery storage system with the price of the PV system. The battery system is sized to be equivalent to the storage in a representative design of the Stirling engine, providing 4 hours of storage, a modest level of storage. Battery prices vary widely based on chemistry, manufacturing, and usage. There is no consensus cost for a residential battery storage system, given that it is still a niche product. As a representative number, SolarCity has made potentially the most competitive play for residential battery storage and has priced its system at $\$2000\,\mathrm{kW^{-1}\,h}$ [14]. With 4 hours of storage as the comparison point, this equates to an additional cost of \$8/W. Storage in the Stirling engine system requires only additional storage tanks, up to the quantity of storage desired, and a pump with controller. Most of the other necessary components are already included in the base Stirling system. These components only add minimal cost to the system for additional storage.

To account for the benefit from CHP, the value of the thermal stream must be determined along with an equivalent electrical value. The most direct comparison is to account for the energy displaced by the thermal stream, including the conversion efficiency of energy displaced. Fortunately, this is precisely what the effective electrical efficiency for a CHP system measures, as discussed in Section 2.1. In this accounting, the effective efficiency of the Stirling converter becomes approximately 36% if the thermal stream is used for a ubiquitous application such as water heating. This effectively increases the rated capacity of the system, and lowers the \$ per watt inversely proportionally by the same amount. Accounting for these storage and CHP value streams in the Stirling engine system, a new comparison can be made, as show in in Table 2.3.

The Stirling engine solar thermal system has a major advantage when the full cost of energy storage is included in a photovoltaic system. There are additional factors that favor the Stirling engine. Battery storage systems have a shorter cycle lifetime than thermal storage tanks, and must be replaced at some point in the lifetime of the system, adding NPV cost. This comparison is made based on 4 hours of storage, a small quantity sufficient for basic energy shifting of peak solar input times to peak demand times. If storage capacity were expanded to cover a full day, the calculus is even more in favor of the Stirling engine, since per-kWh costs for thermal storage are far less than for batteries. This level of storage

Component	Stirling Engine	Distributed PV [3]
Engine System	\$3.10/W	\$0.70/W
Collector	\$0.70/W	
Energy Storage	\$0.50/W	\$8.00/W
Balance of System	\$3.60/W	\$3.60/W
Total	\$7.9/W	\$12.30/W

Table 2.3: Installed price comparison between distributed Stirling system and distributed PV system, accounting for the full value of CHP and energy storage. Energy storage is accounted for by additional battery storage in the PV system while CHP is accounted for by using the effective electrical efficiency of the Stirling engine.

might be desirable for microgrids for long duration islanding capability.

The main barrier to realizing this advantage in this application space is the lack of a market structure to fully incentivize the energy storage. A more likely path forward for Stirling engine technology used as distributed generation is in the developing world. In particular, the advantages of Stirling engines in CHP and energy storage are well-suited for microgrids or off-grid applications. Here, built-in energy storage presents itself as especially appealing without stable or reliable central grids to connect to. The installation of batteries with PV as an alternative energy storage mechanism is not as attractive, due to the difficulty of manufacturing and disposal of batteries and the complexity of electrical hardware and controls. Thermal energy storage for the Stirling engine, on the other hand, is decidedly low-tech and simple to implement, taking the form of storage tanks, pipes and pumps. The thermal output of the engine is also potentially highly useful for water heating where alternatives like gas heating may not have existing infrastructure. Additionally, the fuel flexibility of Stirling engines enables the use of fuel as supplementary or backup energy, adding further flexibilty and reliability in its utilization. This is an area where the strengths of this technology may be valuable enough to overcome the basic cost advantage of photovoltaic technology.

Waste Heat Capture

Waste heat capture is another important application space for Stirling engines. The term encompasses a very broad spectrum of possible applications, with sometimes very different requirements and characteristics, different waste heat temperatures, power quantities, and ambient constraints. Some examples of potential applications include capturing industrial waste heat byproducts, as a bottoming cycle for other generation systems, and capturing otherwise unusable energy at remote sites such as offshore oil wells. Since the application space is so broad, it is difficult to characterize the applicability of Stirling engines in a general

	Small	Medium	Large
Engine capacity	36 kW	90 kW	1000 kW
Exhaust Waste heat	51 kW	160 kW	1024 kW
Other Waste heat	10.2 kW	59.5 kW	829.7 kW
Capacity premium with Stirling	51%	64%	37%

Table 2.4: Diesel generator specifications and waste heat potential for commercial generators at different capacity sizes [12]. The capacity premium is assuming an appropriately-sized Stirling bottoming cycle operating at 60% of Carnot efficiency.

way. Instead, the focus will be on a particularly promising application - diesel waste heat generation. With the renewable generation space being highly competitive, diesel waste heat generation presents a plausible commercial path forward for initial market penetration. Commercialization considerations will be discussed in detail, and explain why this area seems the most promising for initial commercialization of the Stirling engine. This material is based on a report produced by the Cleantech to Market team for this project.

Diesel Waste Heat

Diesel generation still comprises a surprising fraction of worldwide electricity generation, estimated at 5% or 1 TW h per year [2], but dominates in off-grid generation, comprising 95% of total generation at 25 GW to 30 GW [9]. Fuel costs for distributed or off-grid diesel gensets are significantly higher than in other settings, and supply chain issues amplify the desirability of lower fuel use. A Stirling engine converter can be used to generate additional electricity from otherwise discarded waste heat, thereby reducing fuel usage and increasing efficiency. The economic value in this application is the reduced cost of fuel consumed for the same amount of electricity produced.

Diesel generation is used worldwide both as backup power and primary power. For the Stirling engine system to be cost-effective, a high level of utilization must be achieved. This limits the market to diesel-based primary generation, which still accounts for 10-15% of generator sales in the developed world and 15-20% of sales in the developing world. Generators reject heat through several mechanisms, including combustion exhaust gases, cooling loops, and radiative dissipation. Of these, exhaust gases provide the highest quality thermal stream, having higher temperature and thermal power. It is also common to all generator types, and therefore a better target for designing an engine for waste heat capture.

Table 2.4 gives specifications for commercially-available diesel generators at the small, medium, and large size ranges. These generators have varying amounts of usable exhaust waste heat. Assuming a bottoming Stirling engine that converts at 60% of Carnot efficiency, these generators all would see substantial boosts in capacity. This capacity premium can equivalently be translated into reduced fuel use - the advantage provided by the Stirling engine can be designated on a continuum from lowered fuel usage at a constant capacity rating to higher capacity rating at a constant fuel usage.

The economic value of the Stirling engine co-system is heavily influenced by the cost of the diesel fuel. The range of applications and corresponding fuel prices is wide - in the United States and other highly-developed countries, the cost of diesel fuel is approximately $\$1\,\mathrm{L}^{-1}$; in developing countries, the cost of diesel is double that at $\$2\,\mathrm{L}^{-1}$; and in remote or supply-chain-sensitive applications such as military installations, the cost of disel is over $\$5\,\mathrm{L}^{-1}$ [4]. Based on these prices, Figure 2.3 shows payback periods in each of these applications, with additional sensitivity analysis for scenarios where the Stirling engine final price is $2/W, $3/W, and $6/W. These payback periods were calculated assuming 20 hours of operation per day, which is appropriate for diesel used as prime power. The Levelized-Cost-of-Electricity listed in the Figure is derived by calculating the marginal cost of electricity produced by installing the Stirling engine.

The base case price of the Stirling engine is projected to be $3/W, as seen previously in Table 2.1. However, for a full understanding of market risk, the sensitivity analysis at the lower and higher price points is highly important. The base case predicted price is calculated given the best available knowledge at this point, but could easily be higher because of unforeseen design modifications, supply chain problems, or legal or regulatory issues. Likewise, the price could come in lower due to advancements in design or manufacturing processes. Therefore, included in the payback analysis are scenarios for 33% reduction in price, at $5/W, and doubled price, at $6/W. It should be noted that the base case cost analysis ($3/W) discussed previously in the context of distributed generation is actually, by design, specified fully-configured for diesel cogeneration - it includes the engine itself as well as plumbing, balance of system, and installation of the engine that is appropriate for both applications. Costs that are particular to distributed solar generation were included and discussed separately.

As can be seen in Figure 2.3, payback period at $3/W is very attractive over the range of diesel prices. In high-end military applications, the payback period is a short 4 months long, and even for mundane developing world applications, the payback period is about a year and a half. Even if Stirling engine prices were double the projected value, at $6/W, the payback period is still highly competetive at 7 months for military applications and three years for developing world applications. Even the worst case in this set of scenarios, with a payback of three years, is compelling in economic terms.

Besides cost effectiveness, the other necessary component of profitability is sufficient market size. The space of this application is already limited to prime diesel cogeneration. However, this sector represents a reasonably large market segment. As shown in Figure 2.4, even limiting the space to high-end applications where the cost of diesel fuel is high enables a market size of roughly $2.5 billion. This figure shows the various market segments for this type of Stirling application, organized by the cost of diesel fuel and the barrier to entry in that market. Different market segments are scaled by available market size. The prime applications are therefore military and off-grid telecom, represented at $800 million and $1.5

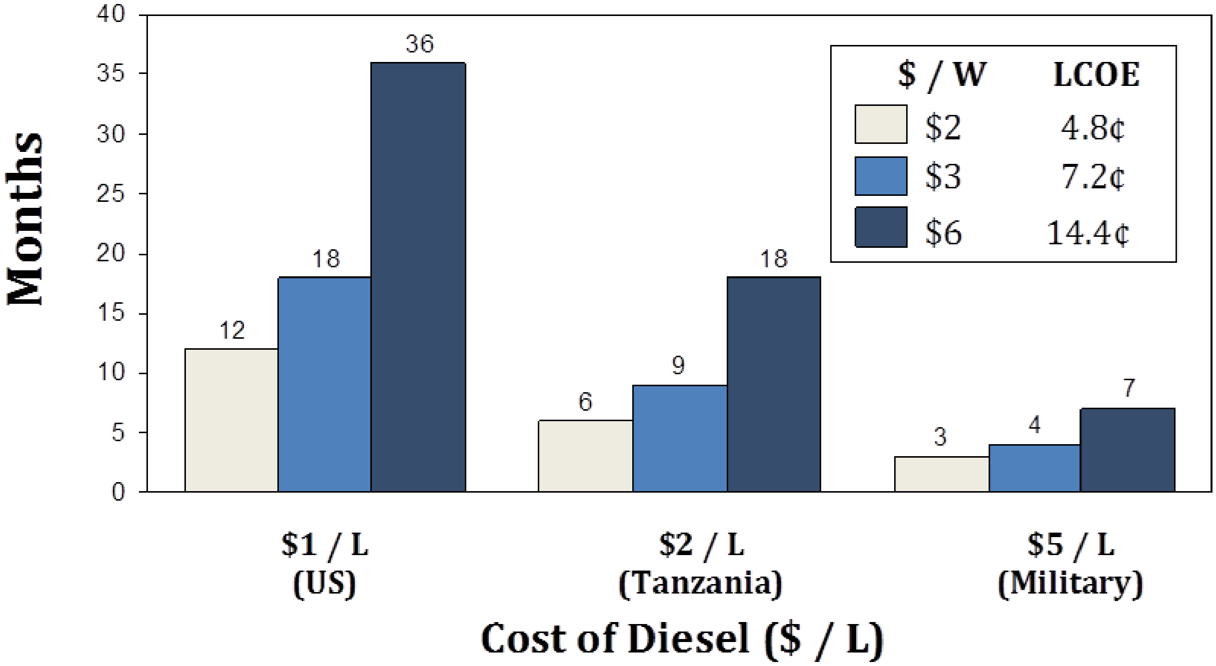

Figure 2.3: Payback periods associated with Stirling engine diesel cogeneration in different markets, with sensitivty to price per watt included.

billion, respectively. For military applications, reduction of diesel fuel usage is especially attractive, as the fully-burdened cost of fuel reaches $\$100\,\mathrm{L}^{-1}$ [8]. Micrograms are also an appealing area for second-phase growth. Once commercial and manufacturing infrastructure for the technology has been established, further expansion into grid applications or commercial microgrids is available.

Summary

In this chapter, the current state of renewable energy was discussed in order to provide context for and to motivate the development of the Stirling engine solar thermal system. It is imperative to transform the electric grid to one based on clean, renewable generation to address the environmental challenges of modern civilization. With such a change, the impending need for storage and reliability that accompanies the growth of intermittent generation poses a deep challenge that solar thermal systems, such as the one proposed herein this disseration, are uniquely poised to address. The technological and economic advantages were discussed and shown to be highly compelling, given the proper market structure and incentives. In particular, two applications have been covered which hold the greatest potential: distributed generation and waste heat recovery. These application areas are selected for technological and economic competitivness and are the most likely path forward for the technology.

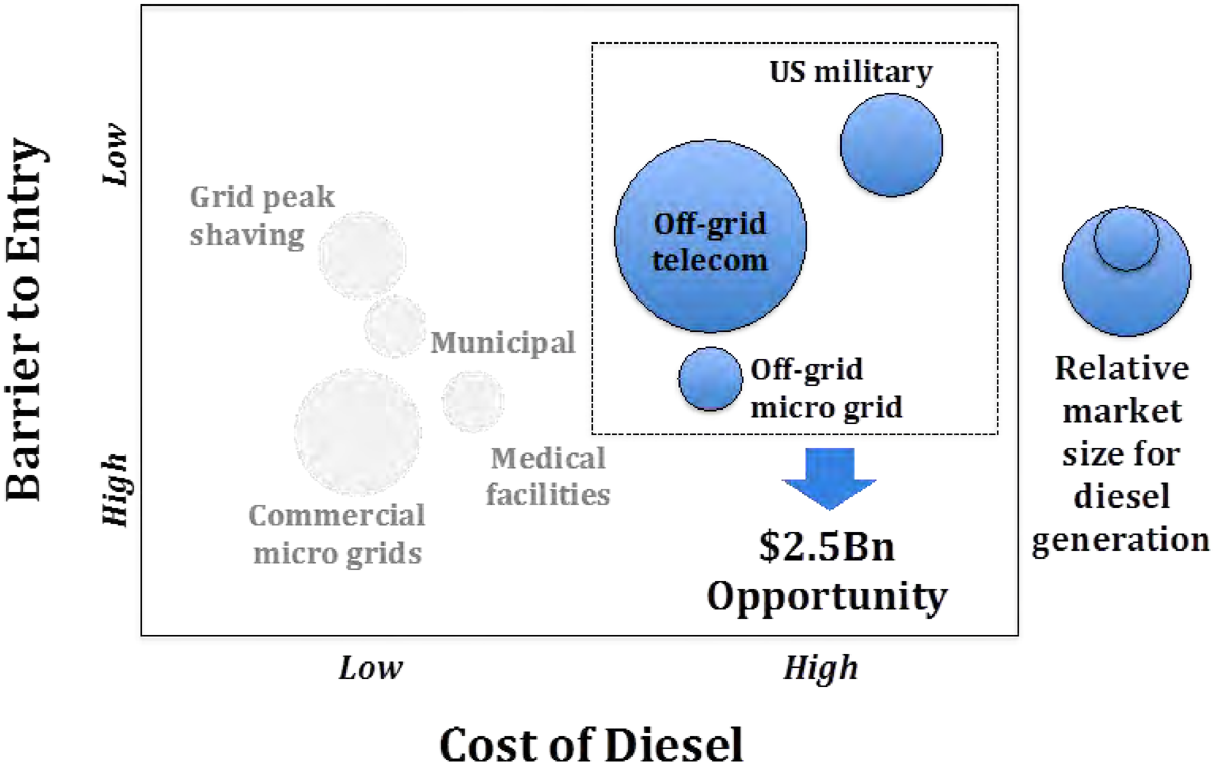

Figure 2.4: Market segments for the Stirling engine as prime diesel cogeneration, organized according to cost of diesel fuel and barrier to entry [16].

The rest of the dissertation will discuss the technical details of the design, development, and testing of the prototype Stirling engine that forms the central component of the overall system. This research serves to demonstrate the technological basis for the Stirling engine system as a promising piece of the renewable energy revolution.

Chapter 3

Design and Optimization

This chapter will cover the detailed design of the Stirling engine converter. The goal is to create a design for a Stirling engine that can operate at relatively high efficiency at a low system cost, while remaining simple to fabricate. This work builds on previous work in [22], while targeting much higher power levels and expanding that work with more detailed physical models and design procedures. The design process incorporates models from multiple physical disciplines, such as heat exchanger analysis, fluid flow models, and kinematic simulations, and also utilizes different methods of analysis, such as static model-based characterization, dynamic simulation, and system-wide parameter optimization. This chapter covers the mechanical portion of the design; electrical conversion and control will be covered in Chapter 4.

3.1 Design Overview

An extensive effort was performed to optimally design a Stirling engine for its intended application. This process consisted both of numerical analysis and optimization as well as mechanical design with considerations toward cost-effectiveness and practicality. In particular, extensive design is needed in order to achieve good performance while meeting the important constraints of low input-temperature and low-cost. These factors differentiate the Stirling engine in question from the typical modern Stirling engine. As will be seen, the design and optimization process leads to an engine with a considerably different physical configuration.

The use of solar collectors with no concentration or low concentration means that input temperature to the Stirling engine can realistically only reach approximately 200 °C. This presents the most significant constraint and challenge to the design of the engine. Typical Stirling engines can utilize input temperatures in the range of 300 °C to 500 °C from primary energy sources such as fuel combustion and radio-isotopes. Lower input temperatures imply a lower maximal Carnot efficiency, but in addition imply that sources of loss or inefficiency are all relatively more detrimental to the overall performance of the engine. Temperature drops across heat exchangers use up a much greater fraction of the available exergy of the input heat, and losses such as friction and compression loss comprise a larger fraction of the overall available work output. Thus, the design of a Stirling engine under these conditions leads to an exceptional effort to reduce losses, even at the expense of lower power rating.

The cost-competitiveness of the energy generation application space also places stringent requirements on the system. This requires the modification of several important Stirling engine standbys. Exotic materials are often used for the hot-side heat exchanger, such as Inconel for its strength and corrosion resistance at high temperatures, but add significantly to engine cost. A very different approach has been taken with the heat exchanger in this engine. The regenerator of a Stirling engine - one of the most important components in terms of conversion efficiency - is usually engineered for very high performance but is one of the costliest components. However, a different approach must be taken in the design of this engine in the pursuit of low cost. The regenerator instead is optimized for high performance with low-cost materials. The details of these components and optimization will be discussed.

In addition to careful design of individual components, comprehensive holistic design of the engine must be performed. Different components in a Stirling engine are remarkably interdependent and interconnected. Modifications to the heat exchanger design can greatly impact the optimal motion of the displacer piston, for example. This is due in part to the fact that the Stirling engine is a tightly packaged, enclosed system with a working fluid that moves through the components repeatedly over each cycle. The components must also be designed to fit together well physically, as excess dead space reduces developed pressure, and excess material increases thermal losses and cost.

The rest of the chapter will cover the process of analysis and optimization, details of specific components, design choices and tradeoffs, and the mechanical design through CAD drawings and component specifications.

3.2 Analytical Design and Optimization

A detailed analytical multi-physical model was written that spanned all the important components in the Stirling engine. This model was designed to predict as accurately as possible the performance of a Stirling engine design, and drew upon previous experience in Stirling engines and well-established research or domain knowledge on characteristics such as thermal transfer, losses, mechanical behaviors, etc. By incorporating these disparate elements into a unified design package, an end-to-end design is enabled that can achieve the performance desired for the intended application.

The Stirling engine design procedure can be categorized into three steps of evaluation, each taking the previous as input: analytical models of a variety of components or physical behaviors of the engine, such as heat exchangers, fluid flows, and other losses; an adiabatic dynamic simulation to evaluate the thermodynamic cycle performance of the engine; finally, an optimization step to guide design parameters for improving the design. The optimization step was used to improve the set of easily-adjustable design parameters for each evaluation, but significant modal changes, such as evaluating the engine for an entirely different working fluid, required separate runs of the procedure. These three steps were run over a variety of interesting design choices, and evaluated along with considerations of cost and practicality, to settle on a final example design for fabrication. The following discussion will mirror this order, beginning with the most important components in the engine.

3.3 Heat Exchangers

One of the most critical components in terms of achieving high performance are the hot and cold heat exchangers. This is especially true with lower temperature differentials, as is the case with low-to-non concentrating solar collectors, since every degree of temperature drop across the heat exchangers represents a larger fraction lost of the available exergy.

The primary tradeoff in the design of heat exchangers is between cost, frictional losses, and heat transfer efficiency. Generally speaking, a heat exchanger can transfer more heat by some combination of increasing the total wetted surface area and reducing the feature size of the contacting components, such as fins, meshes, or tubes. This improves the heat transfer characteristics, but results in higher frictional losses from motion of the fluid and furthermore can increase the cost of the components. This tradeoff cannot be evaluated as a standalone choice - the effect of temperature drop and frictional losses can only be fully accounted for by running the adiabatic simulation of the Stirling cycle.

Another important characteristic is the flow arrangement of the two fluid streams. Parallel flow heat exchangers are inherently less effective, since the temperature of the two streams converge along the flow path and therefore the quantity of heat exchanged is greatly reduced. Counterflow and crossflow heat exchangers maintain higher average temperature differentials through the flow path, leading to improved overall transfer. This design settled on a crossflow arrangement, with the external liquid running circumferentially through the heat exchanger, while the internal working gas flows along radial lines.

The final design of the heat exchanger used as its core a single disc of aluminum, with external liquid heat exchange implemented on one side of the disc (the exterior), and internal working gas heat exchange implemented on the other side (the interior). Aluminum was chosen as a body because it combines high thermal conductivity, low cost, and good structural strength. An inner circle of the aluminum disc is designated as space for the displacer piston, rather than heat exchange. The exterior side of the disc has machined circumferential channels for flowing the external heat transfer fluid, with the bulk of the heat transfer accomplished by convective contact with the aluminum. The interior has machined radial channels for gas flow - the gas flows from the displacer circle and is dispersed across the annular region via these channels. Heat transfer on this side is accomplished with a fine copper mesh, attached on to the channel walls. There are two heat exchangers in the Stirling engine - one for transferring heat into the system, and one for rejecting lower-temperature heat out of the system. Both are identical in this design for simplicity.

Top and bottom views of the heat exchanger body are shown in Figure 3.1 and an isometric top view of the complete heat exchanger is shown in Figure 3.2.

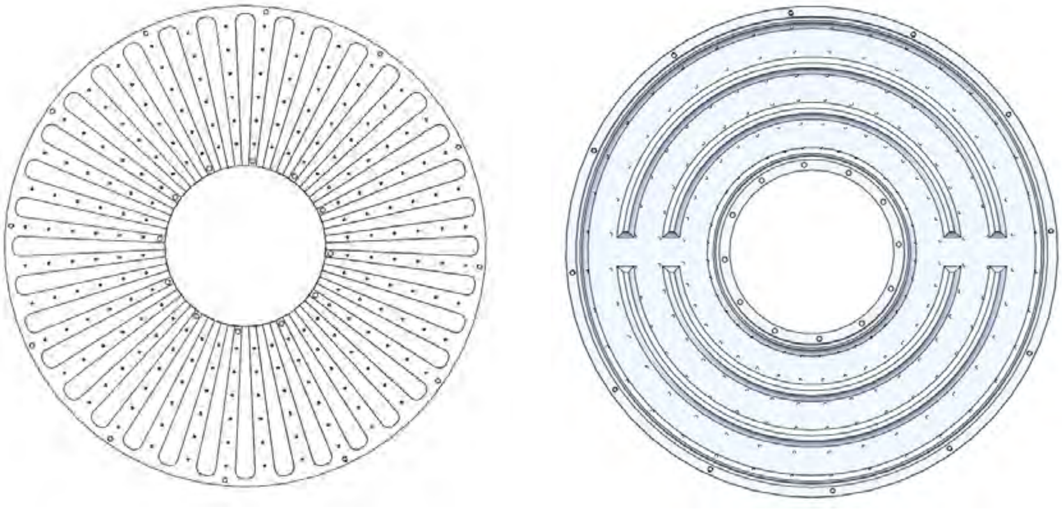

(a) Top view

(b) Bottom view

Figure 3.1: Top and bottom CAD view of heat exchanger body.

The typical method of evaluating the performance of heat exchangers is called the NTU method, and uses the nondimensional metric NTU, or Number of Transfer Units. The NTU method gives a measure of maximum heat transfer that can be achieved between two fluids in a heat exchanger. Even though the NTU method is commonly used for heat exchanger design, this method of evaluation is not ideal for evaluating the Stirling engine for the following reasons. First, the NTU method requires a ratio of heat capacity flux in the two fluid streams; however, this ratio is not an independent variable in the Stirling engine as is the case in simple heat exchangers, but is rather determined by design choices. Second, the fluid flow rate is oscillatory for the internal gas half of the heat exchangers, which complicates the use of the NTU method.

Instead, the heat exchangers were modeled as a network of lumped thermal resistances. This allows the heat exchanger model to be incorporated into the adiabatic simulation and cohesively model the thermal components along with the thermodynamic processes. A thermal resistance is fundamentally a measure of the temperature difference required to drive a certain quantity of heat flux. A component can be modeled as a thermal resistance as long one can define two terminal surfaces and a thermal path, and heat flux is linearly proportional to temperature drop. The terminal surfaces are assumed to be uniform in temperature and heat flow through the path is assumed to be adiabatic. To the extent that these conditions are true, the thermal resistance model is accurate. Otherwise, components may be further subdivided into additional thermal resistances. The definition of a thermal resistance of a component is given by:

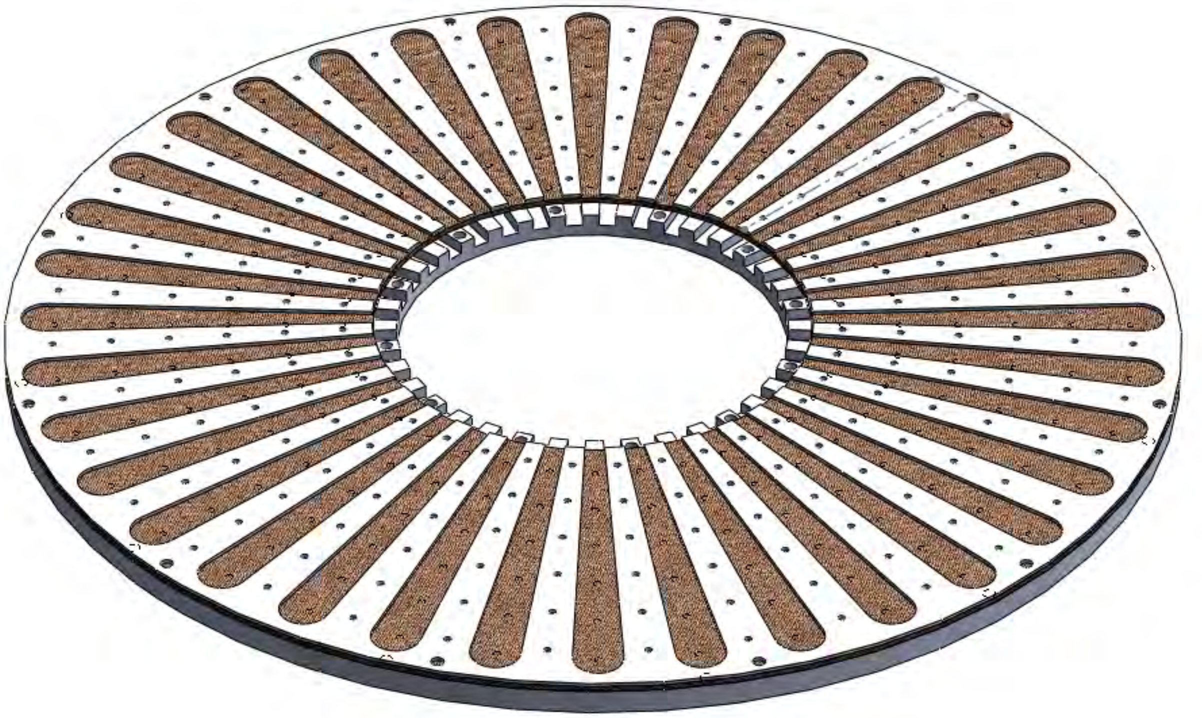

Figure 3.2: Complete heat exchanger shown from a top isometric view. The copper mesh can be seen.

$$R_{thermal} = \frac{\Delta T}{\Phi_q} \tag{3.1}$$

where ΔT is the temperature drop across the component (between the two surfaces) and Φ_q is the heat flux through the component (through the path). Since it is important to minimize temperature drops in this low-temperature regime of the Stirling engine, the goal is to minimize thermal resistances. It should be noted that thermal resistances can be commonly defined as either an intensive or extensive property - i.e. as per unit area or as a total quantity for a body. The latter definition holds for the following discussions in order to characterize the overall behavior of the components.

Thermal resistances are analogous to electrical resistances for the purposes of analytical manipulation - they can be combined in parallel or in series to obtain lumped resistances. As can be seen from Equation 3.1, temperature drop is analogous to voltage drop in this model, while heat flux is analogous to current. In order to calculate the value of the thermal resistance of a component, the particular geometry and physics of that component must be taken into account. For a simple solid extruded body, such as the aluminum body of the heat exchanger, the thermal resistance is given by:

Path Type	Value
In-plane Resistance	$3.97 \times 10^{-5}\,^{\circ}\mathrm{C\,W^{-1}}$
Out-of-plane Resistance	$3.44 \times 10^{-8}\,^{\circ}\mathrm{C\,W^{-1}}$

Table 3.1: Mesh longest path thermal resistances.

$$R_{thermal} = \frac{L}{\sigma A} \tag{3.2}$$

where L is the thermal path length through the body, A is the cross-sectional area, and σ is the thermal conductivity for the material. Here, the contact surfaces with the external liquid loop and the internal working gas are approximately maintained at the same temperature, due to the fact that lateral heat transfer across the surface is easier than heat exchange into the fluid. The path is nearly linear, and has leakage surfaces only at the outer and inner diameter, which comprise only a small fraction of the path cross-sectional area. Therefore, the thermal resistance model is justified along this component.

Heat transfer from the aluminum body throughout the copper mesh in the in-plane (x, y) and out-of-plane (z) directions is important for distributing and maintaining an even temperature at the working gas interface. If this thermal resistance is too large, then heat transfer from the copper mesh to air is compromised by smaller temperature differentials at portions of the mesh further away from the aluminum body. Effective conductivities in these two directions have been determined both analytically and empirically in [18, 29]. The thermal resistances along the maximal-length path in both of these directions are therefore calculated in Table 3.1.

Note that the out-of-plane thermal resistance is negligibly smaller than any other thermal resistance in the system. This is intended, since the copper mesh stack was chosen to be sufficiently thin to elicit an even temperature distribution. The in-plane thermal resistance is still small, compared to the mesh-to-air resistance, at about 14%. This is added to the mesh-to-air resistance, even though it only represents the longest path, in order to design conservatively against the worst case.

Heat transfer from the copper mesh to the internal working gas is significantly more complex. Analytical determination of heat transfer from a mesh to fluids would require complicated dynamic fluid modeling. Complicating the analysis is the fact that air flow through the mesh is oscillatory and alternating, not constant. Prevalent models of fluid flow are based on constant, uni-directional flow and do not apply easily. For example, one could attempt to determine the effective heat transfer by taking uni-directional flow models and averaging over a range of positive and negative gas flow velocities, but alternating flow incurs significant non-idealities such as turbulence. Instead, heat transfer is more easily and accurately predicted by using existing empirically-verified formula for these particular geometries and flow regimes to calculate the Nusselt number, from which the mesh-to-gas thermal resistance can be calculated. The empirical correlation for woven mesh and oscillating fluid flow[20] is given by:

$$Nu = (C_1 + C_2(RePr)^{C_3})(1 - C_4(1 - e)); \tag{3.3}$$

where Re is the Reynolds number, Pr is the Prandtl number, e is the mesh porosity, and the coefficients $C1, C2, C3, C4$ are determined empirically to be

$$C_1 = 0; C_2 = 0.42; C_3 = 0.67; C_4 = 0; \tag{3.4}$$

The Reynolds Number and Prandtl Number are given by the following equations:

$$Re = \frac{vL}{\nu} \tag{3.5}$$

$$Pr = \frac{\nu}{\alpha} \tag{3.6}$$

where v is the velocity of fluid at the location in consideration; L is the characteristic length scale of the geometry, which is typically a hydraulic diameter; ν is the kinematic viscosity of the fluid, and α is the thermal diffusivity of the fluid. Since the flow of gas is oscillating, it must be noted that the velocity u used in calculating the Reynolds number is the root-mean-square velocity.

From this, the thermal resistance can be determined by the following two equations:

$$h = Nuk/D_h \tag{3.7}$$

$$R = \frac{1}{hA_w}; \tag{3.8}$$

where Nu is the Nusselt Number, k is the conductivity of the fluid, D_h is the hydraulic diameter of the mesh, and A_w is the wetted area of the mesh.

Heat transfer from the copper mesh to the air is the most thermally resistive piece of the overall heat transfer path. This is true of heat exchangers in general - transfer from a solid to gas is typically the most challenging component and requires the most design care. In this design, the most important design decisions for this heat transfer component are the characteristics of the mesh - its hydraulic diameter and stack length. As can be seen in Equation 3.7, the hydraulic diameter directly affects the heat transfer performance, and is lowered by choosing finer, more tightly packed mesh. The stack length of the mesh directly determines the volume of mesh that the working fluid travels through, and therefore improves heat transfer in the same way that a longer heat exchanger would in typical applications. Choosing a mesh to optimize the performance of this component will be discussed later. The working fluid side of the heat exchanger along with the mesh are shown in Figure 3.2.

Even though gas flow at the mesh is oscillatory, and by extension heat flux from the mesh-to-air, the heat transfer calculations discussed previously do not have to be modified for oscillatory behavior. This is because, as noted previously, thermal resistance through the mesh material and through the aluminum body are a fraction of the mesh-to-air resistance. Therefore, the temperature drop in these components is small, and combined with the thermal mass of the material, allows the use of a static model with sufficient accuracy.

To reach the copper mesh, the air is pushed by the displacer piston down radial transport channels throughout the aluminum plate. In order to achieve the heat exchange performance as designed in the mesh, these air channels cannot significantly restrict air flow through either excessive length or undersized cross-sectional area. An FEA was performed on fluid flow down the air channels to determine the distribution of gas flow through the channel and mesh, and guided the design of these channels to achieve a high level of uniformity. The FEA results show uniform axial flow into the channel and negligible flow resistance down the length of the channel, confirming its effectiveness in fluid transport. An FEA graph for the example design is shown in Figure 3.3.

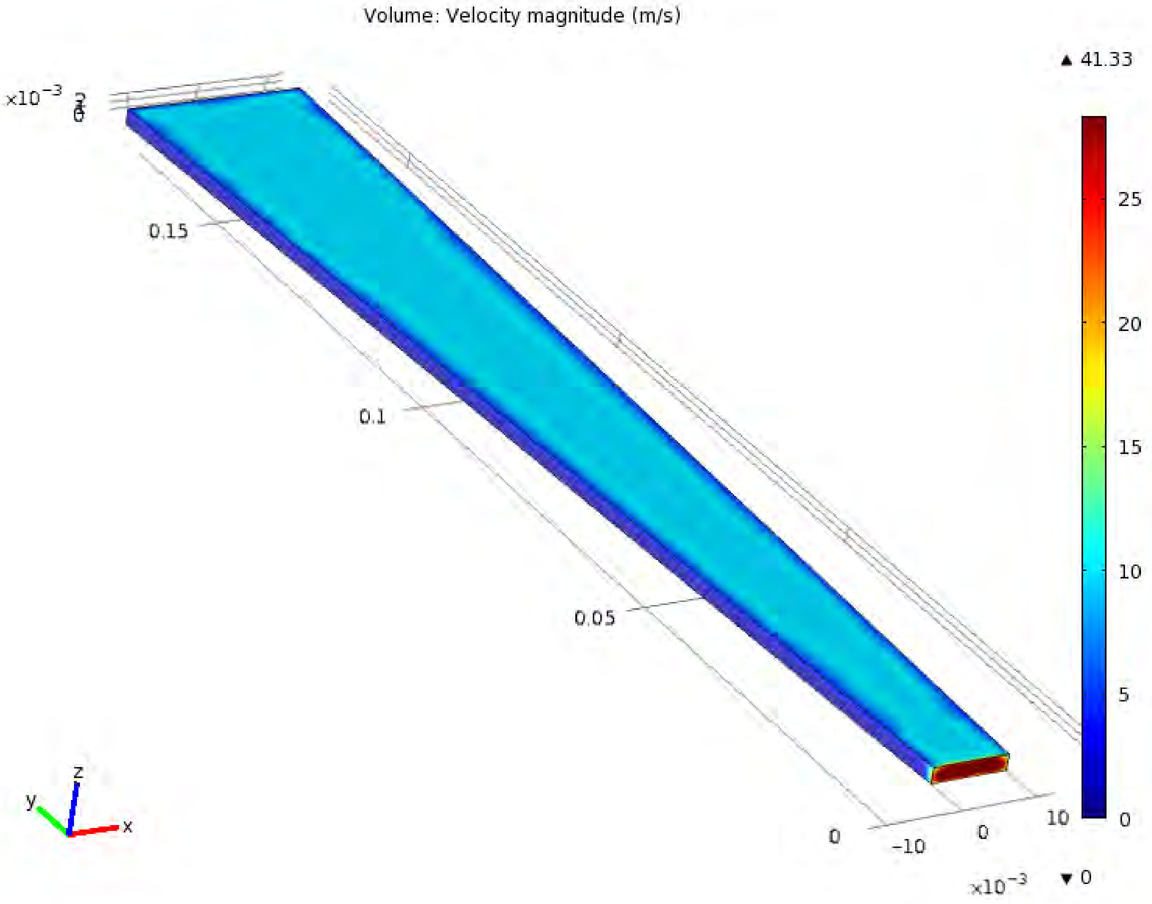

Figure 3.3: Results of an FEA showing flow velocities throughout the transport channel for the working fluid.

The final piece is the heat transfer from the external fluid to the aluminum body. This

Resistance Component	Hot side	Cold side
External fluid to body	$9.91 \times 10^{-5}\,°\mathrm{C\,W^{-1}}$	$1.75 \times 10^{-4}\,°\mathrm{C\,W^{-1}}$
Body path	$5.51 \times 10^{-5}\,°\mathrm{C\,W^{-1}}$	$5.51 \times 10^{-5}\,°\mathrm{C\,W^{-1}}$
Body to mesh (longest path)	$3.97 \times 10^{-5}\,°\mathrm{C\,W^{-1}}$	$3.97 \times 10^{-5}\,°\mathrm{C\,W^{-1}}$
Mesh to working gas	$2.70 \times 10^{-4}\,°\mathrm{C\,W^{-1}}$	$2.33 \times 10^{-4}\,°\mathrm{C\,W^{-1}}$
Total	$4.64 \times 10^{-4}\,°\mathrm{C\,W^{-1}}$	$5.03 \times 10^{-4}\,°\mathrm{C\,W^{-1}}$

Table 3.2: Heat exchanger thermal resistances.

heat transfer occurs on the opposite side of the working fluid heat transfer. The external heat transfer fluid is pumped through a series of flat, wide channels machined into the aluminum body, as shown in Figure 3.4. The flow surface is separated into three distinct flow channels by ridges. The differentiation of the channel into three channels is not to improve heat transfer characteristics, which are only marginally improved, but rather to reinforce the structural integrity of the channel. Without the ridges, the wide channel would bend or buckle under the high forces from the engine pressurization. An FEA was performed to determine the structural support needed in the channel. A graph of the resultant design of the channel is shown in Figure 3.5, which shows the significantly higher body stresses at the locations where the ridges are not present (at the fluid inlet and outlet ports). Without the supporting ridges throughout the rest of the body, the structure would deform significantly and likely fail.

The heat transfer behavior of the external fluid on the aluminum body is one of a constant flow fluid past a flat metal surface, a problem that is well-characterized. This requires first calculating the Nusselt number and from that the heat transfer coefficient, which gives the thermal resistance as in Equation 3.7 and Equation 3.8. The Nusselt number formula for this configuration is well-established in [13] and is given by the following empirical equations:

$$f = (0.79 \ln(Re) - 1.64)^{-2} \tag{3.9}$$

$$Nu = \frac{f}{8}\left(\frac{Re\,Pr}{1.07 + 12.7(\frac{f}{8})^{\frac{1}{2}}(Pr^{\frac{2}{3}} - 1)}\right) \tag{3.10}$$

where f is the friction factor, Re is the Reynolds number, and Pr is the Prandtl number, as defined in Equation 3.5 and Equation 3.6.

The complete set of thermal resistances from the external heat-transfer fluid to the internal working gas is listed in Table 3.2. Some values differ slightly between the hot and cold side heat exchangers due to differing bulk gas properties at the hot and cold chamber temperatures. The difference is relatively small, however.

Thermal resistances determine the temperature drop required to achieve a desired heat flux. The temperature drop across these components is the most important metric for the

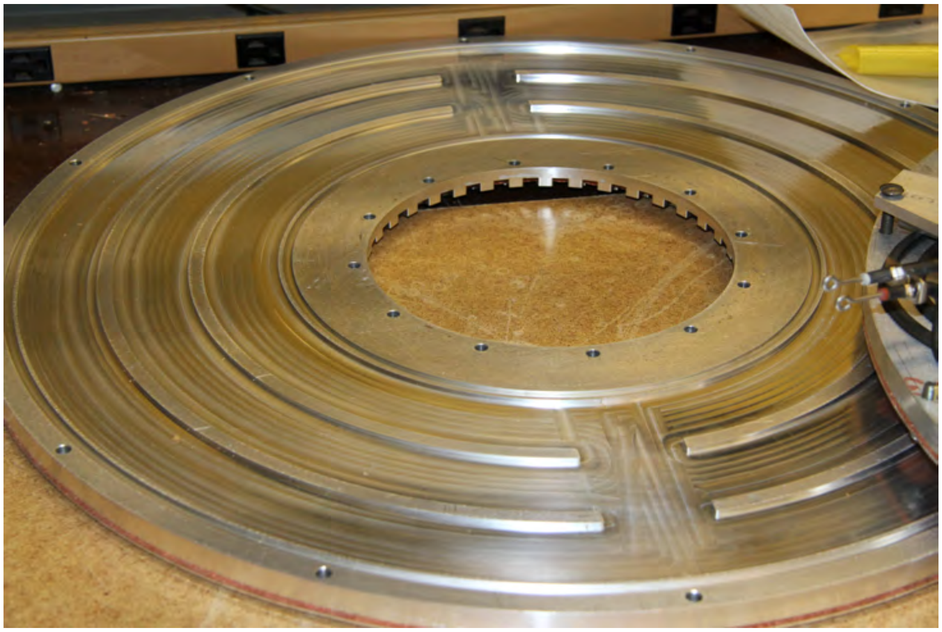

Figure 3.4: External fluid channel for delivering heat into the engine.

Component	Hot side	Cold side
External fluid to body	1.24 K	1.75 K
Body path	0.69 K	0.55 K
Body to mesh (longest path)	0.50 K	0.40 K
Mesh to working gas	3.38 K	2.33 K
Total	5.80 K	5.03 K

Table 3.3: Heat exchanger temperature drops.

purposes of the Stirling engine, as that determines the amount of exergy available for the Stirling thermodynamic cycle. The corresponding temperature drops across these components are therefore listed in Table 3.3.

The temperature drops listed are comparatively low for heat exchangers, and this was by design. As discussed previously, low temperature drops are critical for maximizing the available exergy at the thermodynamic cycle step of the conversion process. Temperature drops are minimized in the aluminum body in accordance with Equation 3.2 by increasing cross-sectional area and reducing path length. The conductivity is constrained by material choices; in this case, aluminum provides high conductivity with sufficient structural support. Temperature drop from the mesh to air is minimized most directly by reducing the hydraulic diameter - in other words, reducing the gap between wires in the mesh. A large surface area

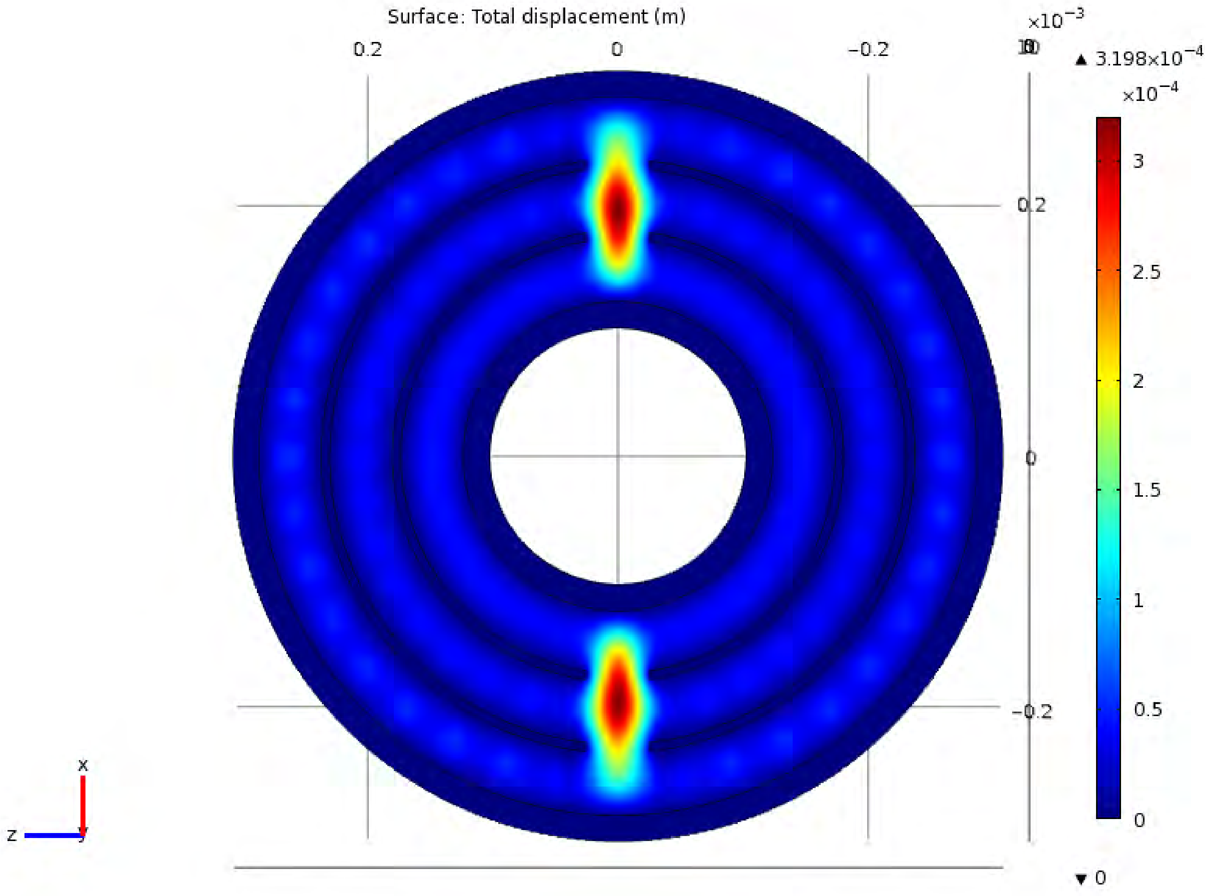

Figure 3.5: Structural simulation of the external fluid channel under pressurization forces.

(called wetted area) is also necessary, and this is achieved both by packing a sufficient quantity of mesh in the availabale volume and by reducing hydraulic diameter, which increases surface area per volume. Given the geometry of the mesh, further lowering the temperature drop from the external liquid to the metal body is achieved primarily by increasing flow speed; sufficient flow speed was chosen in this case to achieve acceptable temperature drops while trading off against flow friction loss.

The design of the heat exchanger went through several iterations, but the final design is the single flat disc of aluminum shown previously. The single-piece design only requires a single milling step on both sides, which helps reduce the cost compared to traditional heat exchangers with precision parts such as tubes or fins. The aluminum plate also has a very low-profile, which allows it to be made from common stock material. More importantly, the flat profile allows for highly parallel heat transfer due to a high cross-sectional area and low path length, allowing much more efficient heat transfer and lower loss.

Further reduction in temperature drops can be achieved by reducing hydraulic diameter or increasing the quantity of the active region - adding more mesh, or lengthening flow path, for example. However, this must be balanced against the additional losses incurred, which will be described in greater detail. This tradeoff is the primary exercise of the optimization of the heat exchanger. The heat exchanger design described here achieves low temperature drops, but is actually not the most significant heat exchange component. The regenerator is responsible for a much greater quantity of heat transfer over each cycle of the engine, and will be described next. The design process for the regenerator used much of the same formulas and concepts as the heat exchanger.

3.4 Regenerator

The regenerator serves a critical role in the Stirling engine. It acts as a thermal reservoir, storing thermal energy during one part of the cycle and reimparting that energy into the working gas in the rest of the cycle. In the absence of a regenerator, gas that flows from the hot side to the cold side would lose a large portion of its enthalpy and would have to be heated up when flowing back to the hot side, leading to poor efficiency. The regenerator is involved in storing and transferring greater amounts of thermal energy than the heat exchangers, and therefore must be highly effective if the Stirling engine is to be efficient at conversion. An ideal regenerator would cool the working gas completely down to the cold-side temperature when flowing from hot to cold, and heat the gas up completely to the hot-side temperature when flowing from cold to hot. The measure of regenerator performance is the degree to which this can be accomplished. Any uncaptured residual heat in the hot-to-cold gas flow must be rejected by the cold-side heat exchanger, and vice versa.

The regenerator often is an expensive component in the engine. Modern designs include the use of a sintered metal matrix or microfabricated honeycomb structures. These provide high effectiveness, but are expensive. In the pursuit of a low-cost technology, a design with a fiberglass mesh was selected that is extremely low-cost. A high effectiveness is achieved with this material in spite of its simplicity by the fact that the material has extremely fine fibers, and therefore a very low hydraulic diameter, and by an extremely high total wetted area, due to the fact that surface area increases as fiber features are made smaller while keeping total mass constant. The fiberglass mesh is also significantly compressed to form a compact matrix, to ensure a low hydraulic diameter and good contact with passing working fluid. The native porosity of the fiberglass is approximately 96%, whereas an 86% porosity was determined to be ideal. This required a compression factor of about 3.5 to reduce the fiberglass to the desired form factor, forming a relatively dense matrix as a result. The heat exchange capability of the material thus organized is very good. Properties of the regenerator are listed in Table 3.4.

The thermal resistance of the regenerator is calculated based on the oscillating flow correlation in Equation 3.3. For the regenerator, an NTU can be calculated with the following equation:

Property	Value
Thermal Conductivity	$0.044\,\mathrm{W\,m^{-1}\,K}$
Porosity	0.86%
Fiber Diamter	$10.9 \times 10^{-6}\,\mathrm{m}$
Stack Height	3.5 cm
Hydraulic Diameter	$6.70 \times 10^{-5}\,\mathrm{m}$
Wetted Surface Area	$467\,\mathrm{m}^2$
Effectiveness	99.8%

Table 3.4: Important regenerator properties.

$$NTU = \frac{1}{Rc_p\dot{m}} \tag{3.11}$$

where R is the thermal resistance, c_p is the constant-pressure heat capacity of the gas, and $\dot{m}$ is the mass flow rate. A heat exchanger effectiveness can be calculated based on the NTU by:

$$\epsilon = \frac{NTU}{NTU + 1} \tag{3.12}$$

The effectiveness of a heat exchanger is typically defined as the ratio of the quantity of heat transfered over a specified period of time to the theoretical maximum quantity of heat that could be transferred in that time. This definition needs a slight clarification for the regenerator, which is defined to be:

$$\epsilon = \frac{Q_{transferred}}{Q_{adia}} \tag{3.13}$$

where $Q_{transferred}$ is the quantity of heat transferred to the regenerator in a single pass through the regenerator, and Q_{adia} is the theoretical maximum that could be transferred in the Adiabatic Model. Therefore, the effectiveness represents the fraction of energy stored from one part of the cycle for use in the next. An ideal regenerator would have an effectivness of unity and would ensure that any working fluid that left or entered the hot or cold chamber would be at exactly the temperature of that chamber. The deviation from ideal effectiveness equates to a deviation in temperature from this ideal, and requires additional input heat on the hot side or additional rejected heat on the cold side. The effectiveness of both the storage step and the regeneration step can be assumed equivalent as long as the temperature deviation is small - the only difference lies in temperature-dependent properties of the working fluid, which typically does not vary except over larger temperature ranges.

A regenerator comprised of random fibers compressed into a geometry is not a new concept. One notable problem with fiberglass wool material for a regenerator is that its fibers can become loose and clog parts of the machine. This design mitigates the problem by using the copper mesh of the heat exchangers as a filter and containment structure for the regenerator. The small hydaulic diameter of the mesh serve to keep regenerator fibers from entering the hot or cold gas spaces. Indeed, during testing, the fiberglass material was observed to be well-contained.

3.5 Displacer Piston

The displacer piston is responsible for shuttling the working gas between the hot and cold chambers. In this design, it resides in the central circular region of the engine. The working gas is pushed radially outwards, then azimuthally through the heat exchanger mesh and the regenerator matrix, then radially inwards back to the displacer region. Since the displacer piston is not involved in the extraction of power from the cycle, it experiences significantly lower forces and stress, only having to overcome the pressure drop due to frictional drag of the working gas. However, the displacer piston contacts both the hot and cold chamber, and therefore experiences a temperature gradient that must be accounted for. This leads to several important design choices. First, the displacer piston is hollow and light. This helps reduce conduction loss through the displacer. Since it does not experience high forces, it does need the same structural strength as the power piston, but it is reinforced with circle of six interior standoffs to maintain structural integrity. There is a 0.003 inches of clearance between the displacer and its cylinder, which gives sufficient room between the skirt of the piston and the cylinder wall to allow thermal expansion without scraping.

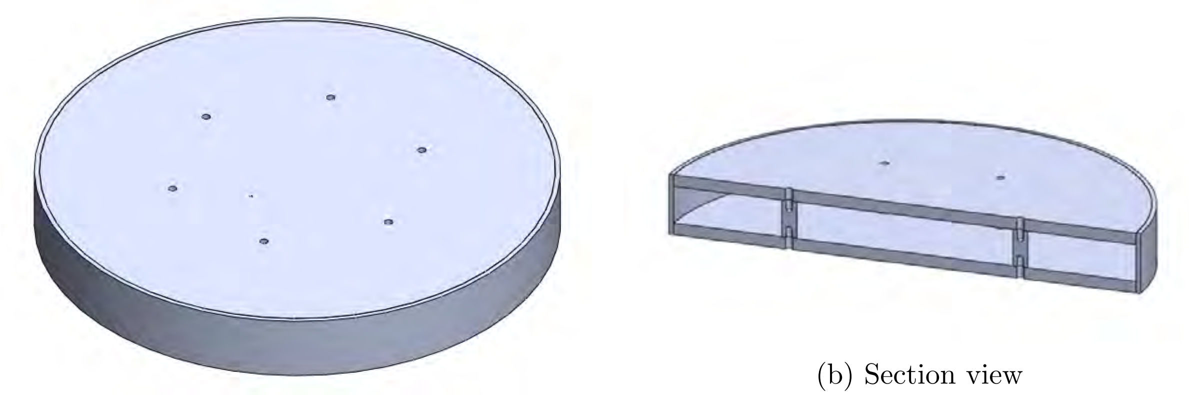

(a) Isometric view

(b) Section view

Figure 3.6: Displacer isometric and section view, showing hollow design and interior supports.

The displacer design is shown in Figure 3.6. Properties of the displacer are shown in Table 3.5. The displacer consists of parallel top and bottom plates press-fit into a shelf on a thin piston wall. Six steel spacers reinforce an otherwise hollow interior. By being hollow, conduction through the piston is eliminated except for through the wall and spacers. A tiny bleed-hole allows the internal pressure to equilibrate with the engine pressure, but at a much slower rate than the cycle itself to prevent interactions with the gas pressure waveform. The position of the displacer piston determines the volume in each of the hot chamber and the cold chamber, and its motion drives gas between the two chambers. The volume displacement due to the displacer is given by:

$$V_{d,swept} = A_d x_{d,max} \sin(\omega t) \tag{3.14}$$

where A_d is the piston head area of the displacer, $x_{d,max}$ is the maximum amplitude of displacer motion, and ω is the frequency. This gives the following volume variations in the hot and cold chambers, without including the component due to the power piston:

$$V_c = V_{clc} + A_d x_{d,max} \sin(\omega t) \tag{3.15}$$

$$V_e = V_{cle} - A_d x_{d,max} \sin(\omega t) \tag{3.16}$$

where V_c and V_e are the volumes in the compression (cold) chamber and expansion (hot) chamber, V_{clc} and V_{cle} are the clearance (dead) volumes in the compression and expansion spaces, respectively, and ω is the cycle frequency.

The displacer piston can be designed as a free-piston, or as a kinematically linked component to the power piston via a crankshaft or other mechanism. There are advantages and disadvantages to each approach. A free piston design typically utilizes flexures, diaphragms, or a magnetic spring to constrain the motion of the piston and provide a restoring spring force, with an electromagnetic acuator to drive it. The use a of free piston design typically reduces losses, allows dynamic actuation and adjustment of amplitudes, and allows independent operation from the power piston. However, it adds complexity in the design and control of the piston and requires a separate input of power to be driven. A direct kinematic linkage via a crankshaft constrains the piston to a specific amplitude and phase angle, and is significantly simpler to design. The displacer piston in this case is driven by power developed by the power piston, so no additional drive is needed. While previous research by this group [21] has used a resonant free piston, for this design, a crankshaft was chosen to simplify actuation and controls.

Since the displacer is hollow, care must be taken to ensure that the structure is stable under pressure. While the displacer will equilibrate with the average pressure of the engine, the engine produces a pressure waveform that exerts pressure across the top and bottom of the displacer. The exact amplitude of this pressure fluctuation can only be determined at a later step in the design process, as part of the adiabatic simulation. An analysis using classical plate deflection was performed on the displacer to calculate plate deflection under the maximum pressure deviation developed. The spacers were assumed to be anchor points, since the top and bottom plates are rigidly attached with bolts at those points. The press fit at the outer diameter of the plates was not assumed to provide any support in order

Property	Value
Material Type	Stainless Steel
Bore Diameter	20.3 cm (8 Inches)
Skirt Length	2.57 cm
OD Clearance	3 thousandths
Top and bottom plate thickness	5 mm
Wall thickness	2 mm
Peak-to-peak stroke	2.8 cm
Conduction loss	11.85 W K^{-1}
Mass	2.8 kg

Table 3.5: Displacer properties

to design conservatively, as thermal expansion could compromise the structural support of the press fit. The analysis determined a plate thickness of 5 mm, which gives a maximum deflection of approximately 0.32 mm at the OD, or about 6.4% of the plate thickness. The deflection along the radius of the displacer is showin in Figure 3.7.

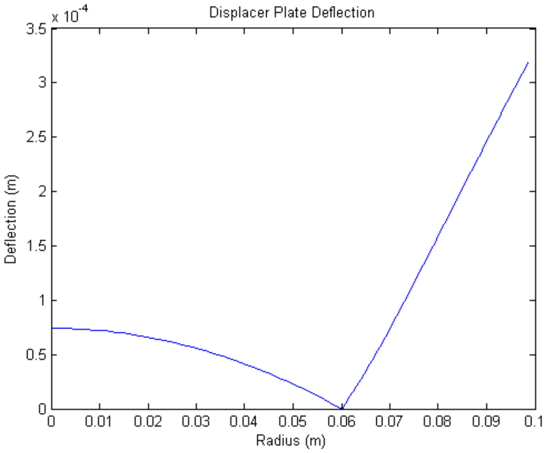

Figure 3.7: Deflection vs radius of the top and bottom displacer plates at rated pressure.

3.6 Power Piston

The power piston is responsible for the expansion and compression strokes of the engine. As such, it experiences high forces and has to be more substantially built than the displacer piston. In this design, the power piston is a solid steel cylinder with a hollowed out inner circle, as shown in Figure 3.8. The piston is located on the cold side of the engine, and as such does not need to be designed against any significant thermal expansion. The power piston compresses and expands the total volume of working fluid inside the Stirling engine, extracting power during operation. The volumes in the hot and cold chambers due to the power piston, along with the displacer volume variations, is given in the following equations:

$$V_c = V_{clc} + A_d x_{d,max} \sin(\omega t) + A_p x_{p,max} \sin(\omega t - \phi) \tag{3.17}$$

$$V_e = V_{cle} - A_d x_{d,max} \sin(\omega t) \tag{3.18}$$

where A_p is the power piston head area, V_c and V_e are the volumes in the compression (cold) chamber and expansion (hot) chamber, V_{clc} and V_{cle} are the clearance (dead) volumes in the compression and expansion space, $x_{d,max}$ and $x_{p,max}$ are the amplitudes of displacer and power piston stroke, and ω is the cycle frequency.

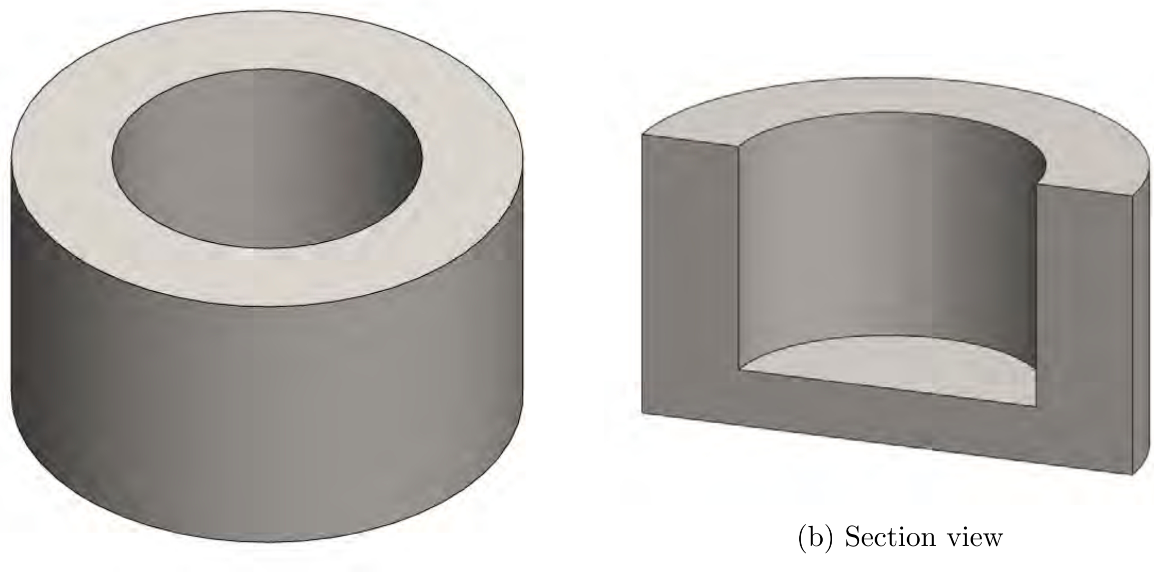

(a) Isometric view

(b) Section view

Figure 3.8: Power piston isometric and section view.

The power piston experiences high forces during the compression and expansion strokes, which require reactive drive power. The pressurization of the working fluid increases the compression forces experienced per unit of volume change. These forces can easily become excessive. One approach to mitigating this is to treat the internal working fluid as a gas spring and to design the power piston mass such that at the rated pressure and motion, the piston moves at the resonance of the mass-spring system. This allows the gas spring to take up most of the reactive power required to drive the piston in steady-state sinusoidal motion.

To achieve a particular mass, the only relevant geometry of the power piston to the gas cycle is the interior face of the piston. This face, along with the motion of the piston, determine the effect of the power piston on gas motion and compression. In light of this, material can be removed from the power piston on the exterior face to achieve the desired mass without affecting the internal cycle. In this design, a cylinder is bored out from the exterior face to achieve resonance with the gas spring. The intended resonant mass is given by the following equations:

$$k = \frac{\gamma p A_p^2}{V} \tag{3.19}$$

$$m = \frac{k}{\omega^2} \tag{3.20}$$

where γ is the gas heat capacity ratio $\frac{c_p}{c_v}$, p is the gas pressure, A_p is the cross-sectional area of the piston that faces the gas, V is the volume of the gas spring, and ω is the angular cycle frequency of the engine. The designed mass of the power piston to achieve resonance at 20 Hz is 14 kg.

The power piston sits at an interface between the internal working fluid and the crank space, which in this design is pressurized to the mean working gas pressure. As the internal pressure oscillates around the mean, this pressure differential can cause leakage flow, which imposes a loss on the engine in the form of lost P-V work. This interface must be sufficiently sealed to prevent excessive leakage of gas to or from the ambient environment. In this engine configuration, this interface is entirely present on the cold-side of the engine, unlike in certain other Stirling engine configurations, which greatly simplifies the sealing. In this design, sealing is achieved simply with a tight clearance fit between the power piston and its cylinder housing. The skirt of the piston was designed with a clearance of 1 thousandths to the piston cylinder, achieved by an initial machined clearance of 2 thousandths, then filled with a coating down to 1 thousandths in a precision spray-on process.

Since this is a contacting surface, it also serves as a bearing surface between the power piston and the rest of the engine. The lubrication of this surface is also achieved with the coating, which is a Xylan 1620 dry-film lubricant. The Xylan material was chosen for its low coefficient of dynamic friction (about 0.02) over a wide range of surface pressures, and good wear resistance and corrosion protection. With this coating, the piston achieves both low friction in motion and adequate sealing of the working fluid.

Property	Value
Material Type	Steel
Bore Diameter	17.78 cm (7 Inches)
Skirt Length	10 cm
OD Clearance	1 thousandths (after coating)
Coating	Xylan 1620
Peak-to-peak stroke	9 cm
Mass	14 kg

Table 3.6: Power Piston properties

3.7 Adiabatic Simulation and Optimization

A thorough evaluation of the performance of a Stirling engine design can be performed with a dynamic simulation using the Adiabatic Stirling Model, developed in [28]. The primary eponymous assumption of the model is that the compression and expansion cycles are fast compared to the thermal transfer time constants in the hot or cold chamber - in essense, the working fluid does not lose or gain a significant amount of thermal energy during those steps. This equates to an adiabatic trajectory on a thermodynamic diagram. This model is incorporated with the collection of multiphysical losses and inefficiencies in the engine to develop a simulation that can accurately predict the resulting efficiency and output power. These losses and inefficiences will be described in detail in a subsequent section.

The outputs of the adiabatic model are the thermodynamic work developed during the cycle, the internal pressure over the cycle, and heat flows between each of the regenerator, hot and cold chambers, and hot and cold heat exchangers. Losses are subtracted from the output to determine performance. This information allows evaluation of the expected engine performance for the given design. An important output of the adiabatic model is the predicted internal pressure and working fluid volume waveforms. Combining these waveforms gives a pV diagram, which is a trace of the thermodynamic cycle in terms of pressure and volume. The shape of the pV diagram provides insight into the Stirling cycle output, and comparison with a trace of an ideal pV curve shows the non-idealities of the engine in the form of lost pV area. The pV diagram produced by the adiabatic simulation is shown in Figure 3.9, along with an illustrative trace of an ideal isothermal Stirling cycle, which is comprised of isometric steps at either side and isothermal curves through the middle. This illustrates that the actual thermodynamic performance only sweeps a fraction of the ideal case.

The results from the adiabatic model are fed into an optimization program to search over a parameter space of design values. The entirety of models and the adiabatic simulation are combined with a cost function for the optimization routine, which essentially is the cycle

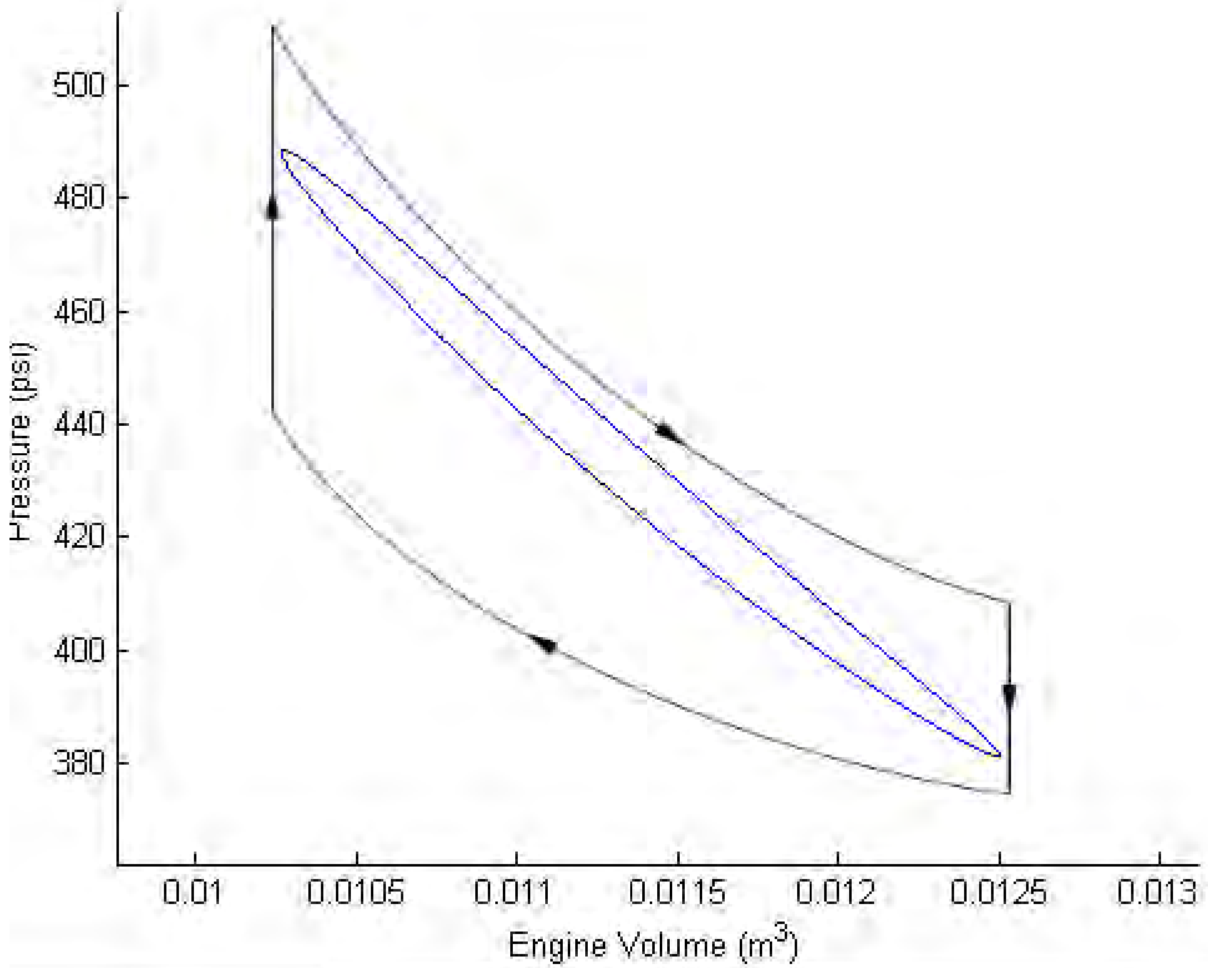

Figure 3.9: The P-V diagram produced by adiabatic simulation is shown, along with an illustrative diagram for the ideal Stirling cycle.

efficiency. The procedure searches the space of a specified set of parameters for the optimal design point. The most important parameters for the search step include the displacer and piston swept volumes, the regenerator dimensions and packing factor, and the heat exchanger mesh dimensions. Other free parameters, such as the phase angle between the pistons, were tested with the optimization procedure, but did not lead to noticeable cost-function changes.

The central tradeoffs for regenerator optimization are between heat transfer effectiveness and fluid flow losses. The displacer piston swept volume, in relation to the dead volume, determines the average temperature and pressure changes during the cycle, and therefore the work available each cycle at the cost of frictional flow loss. For the power piston, swept volume determines the compression and expansion ratio, and therefore the power developed each cycle at the cost of increased compression loss. Both pistons therefore have a swept volume tradeoff between power and efficiency. The search over both swept volumes allows selection of a design that matches the design power output with optimal efficiency.

Figure 3.10 shows contour plots of conversion efficiency and output power as function of the stroke length, which is a proxy for the swept volume. Design candidates were adjusted to reach the desired power level within the maximum efficiency region, as shown in this graph. As can be seen, higher swept volumes correspond to higher output power, but can reduce conversion efficiency due to increased flow friction and other losses. Figure 3.11 shows a sweep of various regenerator stack lengths at the selected piston stroke lengths. The conversion efficiency with respect to this parameter is maximized at a design point that balances regenerator effectiveness and flow loss. Similar optimizations were performed for heat exchanger stack lengths. The overall engine design was refined by optimizing each of these parameters in turn iteratively.

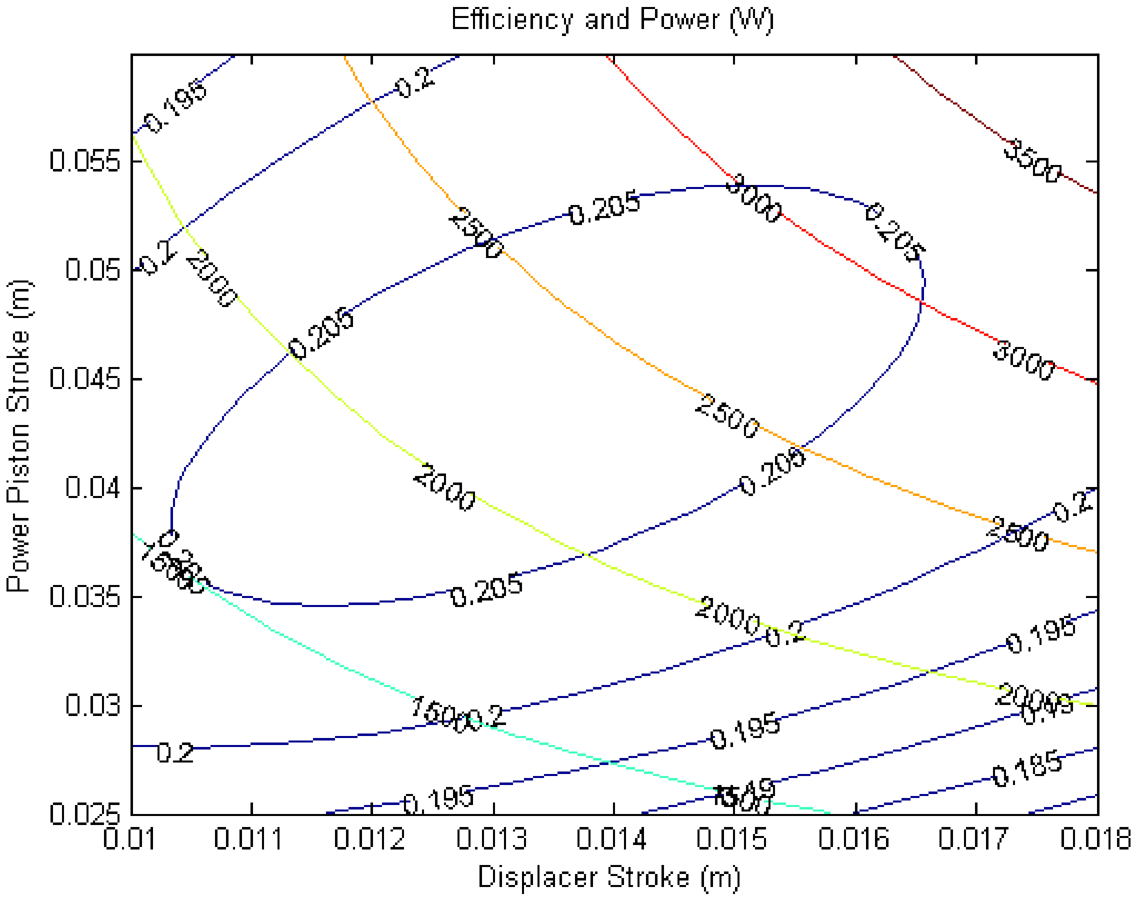

Figure 3.10: Optimization sweep over piston strokes, showing contour plots of efficiency and power level.

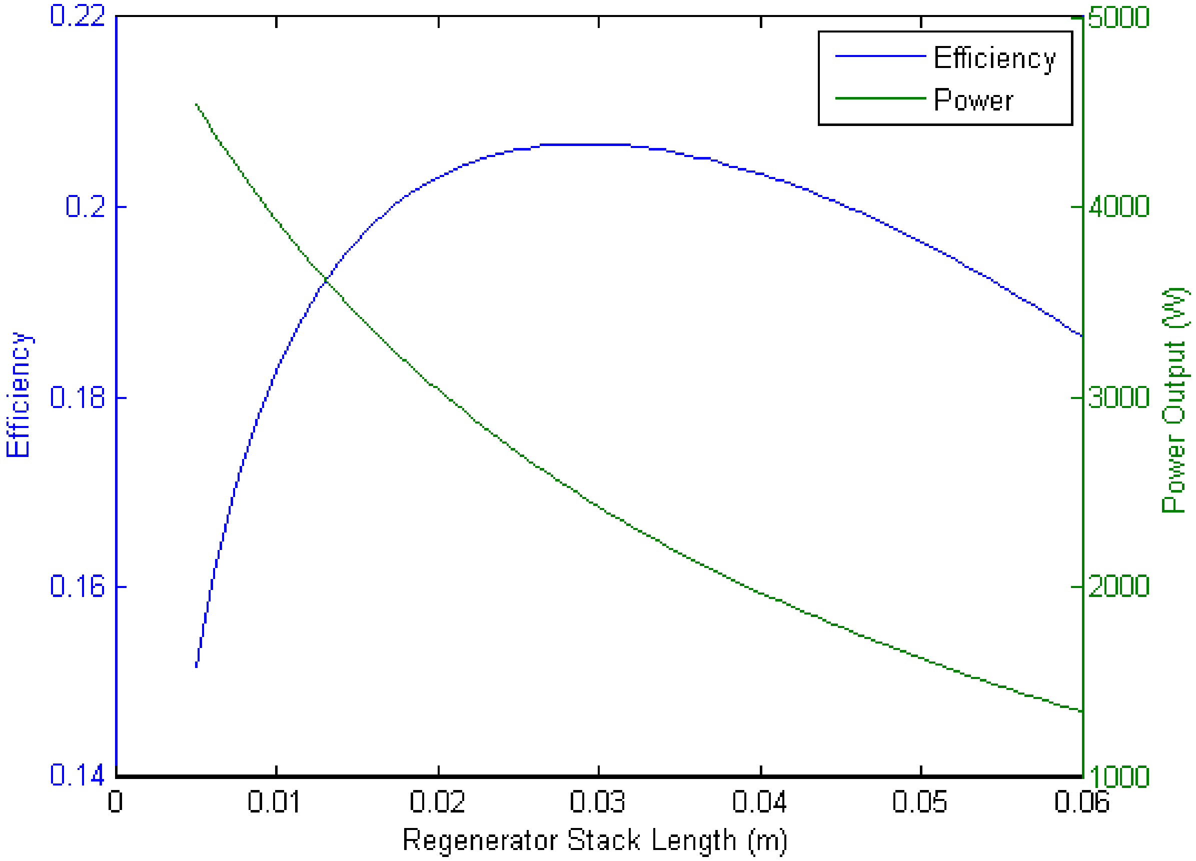

Figure 3.11: Optimization sweep over regenerator stack length.

Working Fluid

The working fluid of the Stirling engine is an important design choice, since it interacts with every component of the engine and is responsible for heat transfer throughout three heat exchangers (including the regenerator). The properties for an ideal choice for working fluid would include low heat capacity, which provides greater temperature swing for a given quantity of heat absorbed and improves regenerator effectiveness, but lowers heat transfer at the heat exchanger; high thermal conductivity, which improves heat transfer at the heat exchanger and regenerator; and low viscosity, which reduces frictional drag throughout the engine. The ideal candidate for a working fluid based on material properties alone is hydrogen gas. However, hydrogen carries practical problems. First, it is flammable, adding a significant safety concern to an otherwise benign technology. Second, the small molecule size of hydrogen makes it hard to contain, requiring high-quality hermetic seals to prevent leakage, and hydrogen also causes embrittlement of steel.

Helium is more typically used, as it is inert and has nearly the same properties as hydrogen. Helium is also prone to leakage, but not to nearly the same degree as hydrogen. However, helium is relatively expensive, and would have to offer significant performance advantages to merit its use over ordinary gases such as air and nitrogen. The full simulation and optimization procedure was performed to compare the expected performance between these gases and ordinary compressed air or nitrogen. Comparisons of the most significantly changed parameters and results are shown in Table 3.7. Different piston strokes and regenerator stack length are the most important design changes for use with these alternate gases. Note that hydrogen also allows operation at a lower pressurization for the same power level. Graphs of the stroke sweep step of optimization for these two designs are shown in Figure 3.12.

The final design settled on a working fluid of compressed nitrogen. Primarily chosen for its low cost and simplicity, compressed nitrogen is cheap, easy to contain, and can be easily repleneshed if leaks occur. The use of nitrogen does exhibit a performance penalty compared to alternative gases, but the difference is small enough that practical considerations of usage dominate. The realities of the intended applications are also important here; low cost and low maintenance are crucially important in power generation, especially in developing regions.

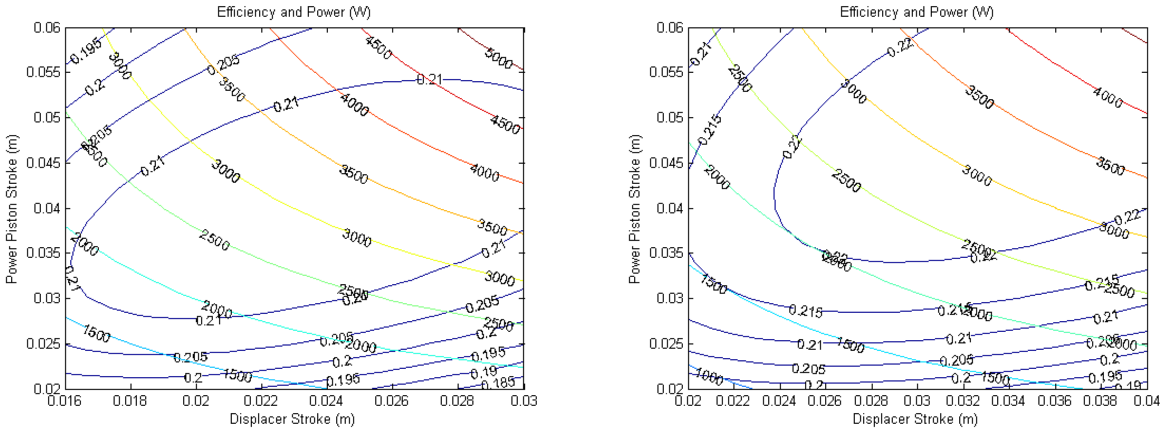

(a) Helium

(b) Hydrogen

Figure 3.12: Working Fluid Stroke Length Sweep

	Nitrogen	Helium	Hydrogen
Optimal Efficiency (2.5 kW)	20.7%	21.7%	22.2%
Displacer Stroke Length	1.4 cm	2.0 cm	2.8 cm
Power Piston Stroke Length	1.4 cm	3.8 cm	4.2 cm
Regenerator Stack Length	3.0 cm	3.6 cm	2.2 cm
Pressurization	30 bar	30 bar	15 bar

Table 3.7: Stirling engine losses

3.8 Drive Train

The drive train of the engine is the kinematic linkage between the power piston, displacer piston, and alternator. Two typical designs are used: a free-piston design or a crankshaft. Free piston designs have advantages in the ability to vary the swept volumes, fewer moving parts, and lower frictional losses. A crankshaft design has advantages in not requiring independent piston actuation, simpler controls, and utilization of parts which already have a ubiquitous supply chain. A crankshaft was chosen for this design for these reasons. The primary design implication for the engine cycle is that the swept volumes of the displacer and power pistons are fixed by the geometry of the crankshaft. The crankshaft diameter must be designed to accomodate the maximum forces developed by the power piston, as well as the forces needed to drive the displacer piston. Bearings must also be chosen to reduce losses, as these losses are directly subtracted from output work. A picture of the final built crankshaft is shown in Figure 3.13, and Figure 3.14 shows it assembled with the connecting rods and pistons. At each of the connections in the crankshaft, an off-the-shelf or custom bearing was used; these are listed in Table 3.8.

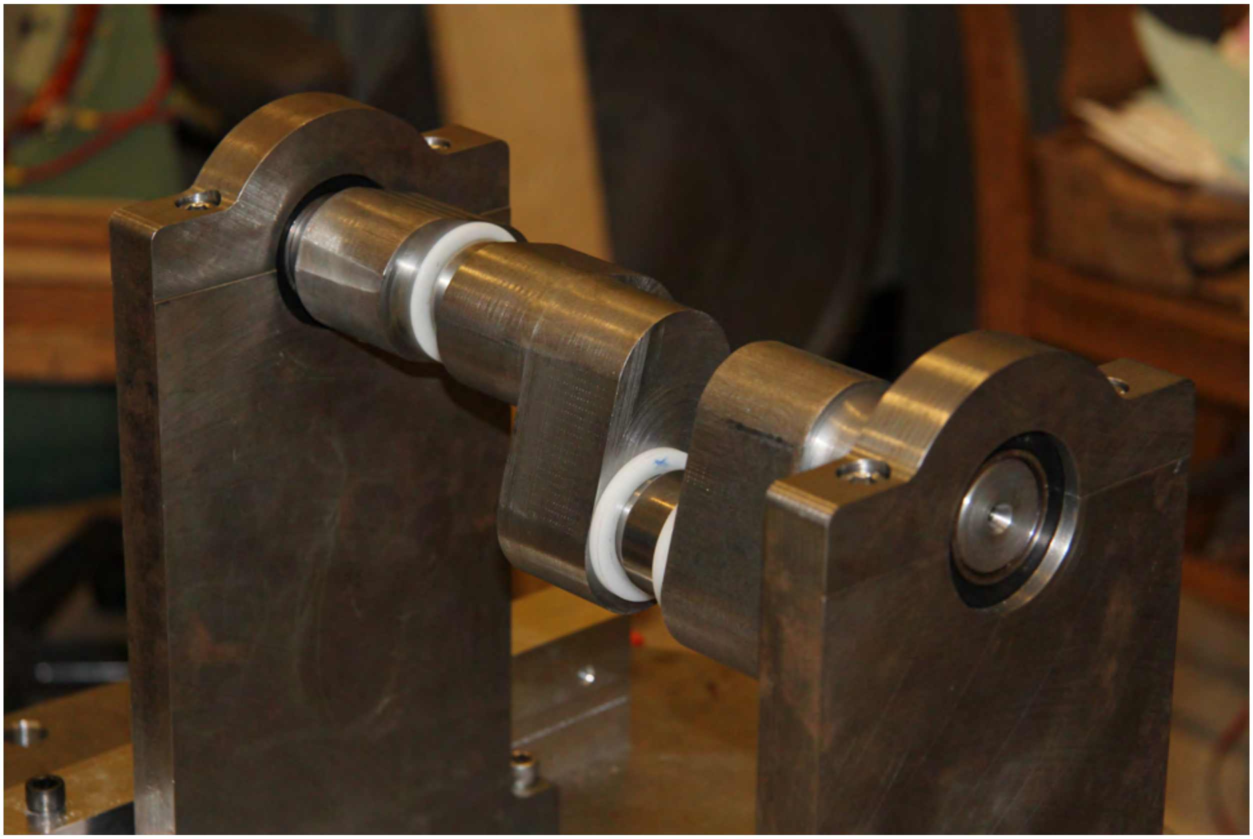

Figure 3.13: Crankshaft unconnected to pistons.

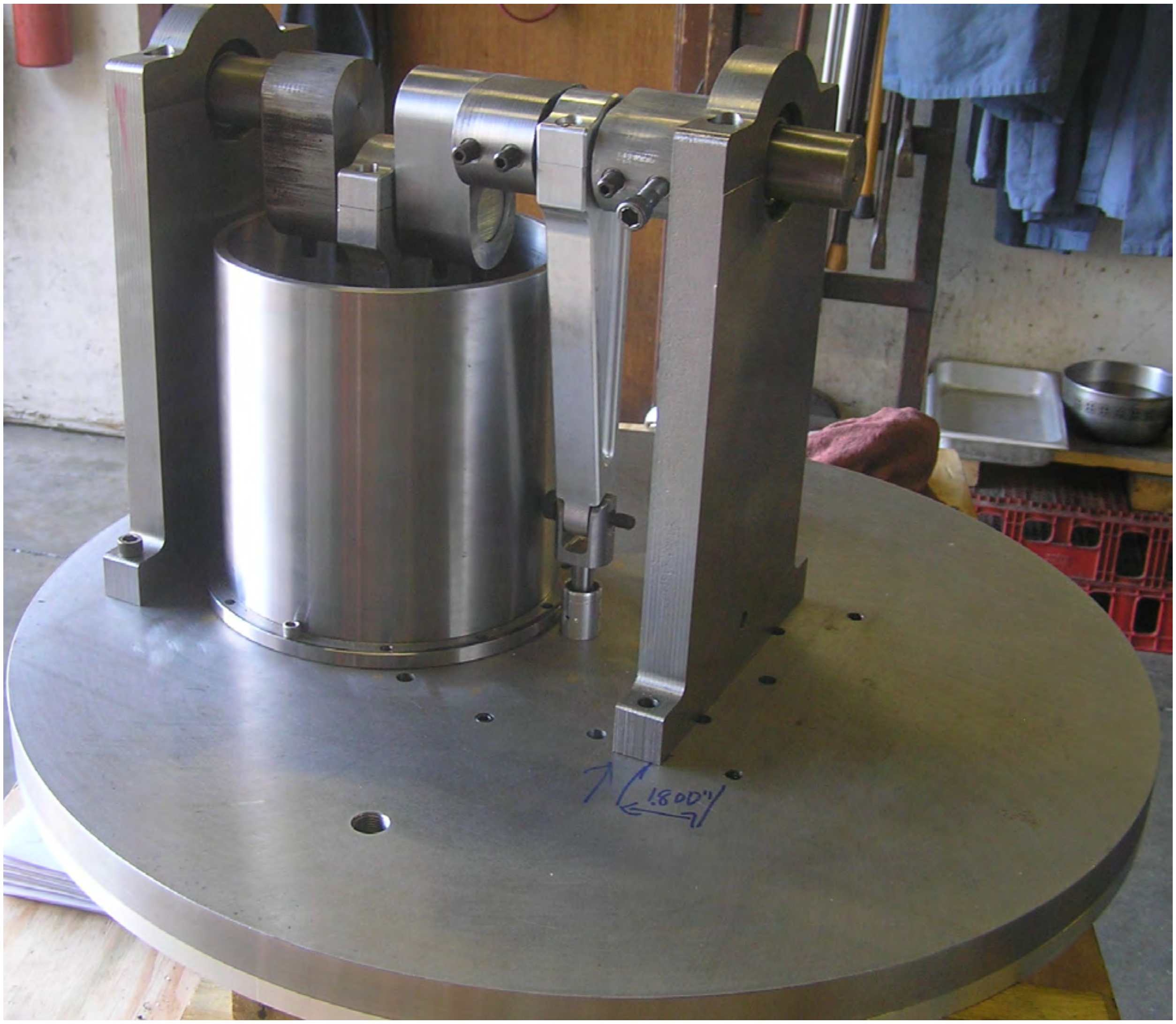

Figure 3.14: Crankshaft assembled with connecting rods to pistons.

The weak point of the crankshaft and drive train is the piston rod bearing for the displacer, which both serves as the bearing as well as enforces linear motion of the piston rod. During testing, this proved to be problematic, as the bearing failed repeatedly or developed angular play that led to the displacer contacting its cylinder. To mitigate this problem, a double-bearing housing was designed and fabricated, as shown in Figure 3.15.

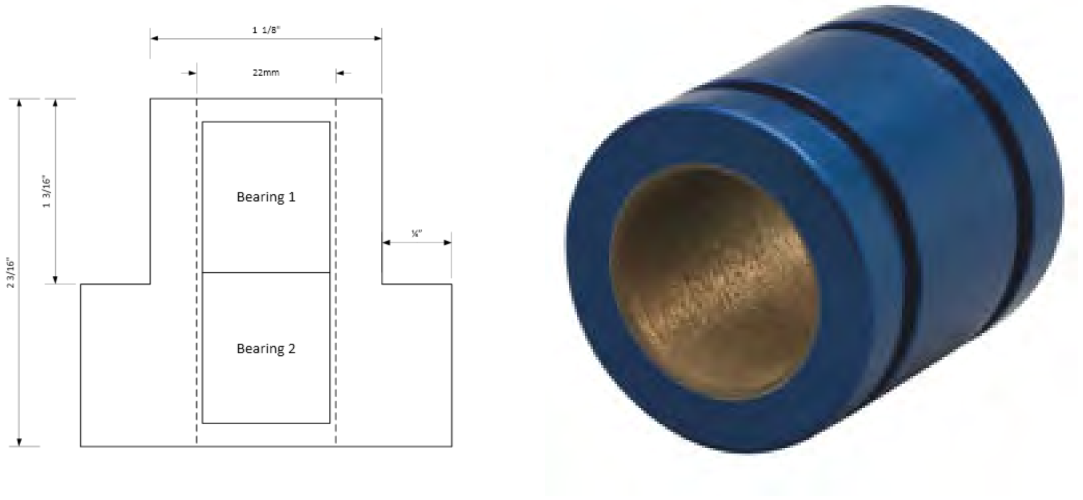

(a) Double-Bearing Housing (b) Linear Bearing

Figure 3.15: Bearing housing for the displacer linear bearing.

Purpose	Bearing Type	Bore	OD	Load Rating
Displacer rod	Linear Sliding bearing	12 mm	22 mm	3335 N
Displacer connecting rod	Needle bearing	35 mm	42 mm	18 700 N
Power piston crank-joint	Needle bearing	35 mm	42 mm	18 700 N
Power piston piston-joint	Needle bearing	15 mm	21 mm	7800 N
Crankshaft mounts	Deep groove bearing	35 mm	62 mm	17 000 N

Table 3.8: Bearing Components

Component	Total Force	Direction-Of-Motion	Orthogonal
Power Piston	708 N	684 N	184 N
Displacer Piston	251 N	250 N	17.7 N

Table 3.9: Peak Piston Forces

3.9 Losses and Inefficiencies

Losses and inefficiencies in the Stirling engine represent deviations from the ideal conception of heat engine operation using a Stirling cycle. These can range from friction from gas flow to thermal energy that is not fully captured by a heat exchanger. Each of these impacts the performance of the engine in different ways - not all losses have the same impact on efficiency.

An important classification of loss is distinguishing between enthalpy loss and work loss. The difference between these types of loss is whether the energy has been thermodynamically converted to work or not. Enthalpy losses, which are pre-conversion, are less adverse than work losses, which are post-conversion, because each watt of output work required multiple watts of input thermal energy due to the efficiency of the cycle. To properly account for this difference, enthalpy losses are multiplied by the conversion efficiency and added to work losses to determine the total engine loss.

A second nuance is that losses can contribute or detract from the work load of the heat exchangers. For example, heat flux directly from the hot side to the cold side imposes a burden on both hot and cold side heat exchangers, as that heat must be transferred into the engine at the hot side and transferred out of the engine at the cold side. Frictional loss manifests in the form of added heat, but where in the engine this heat is added changes the accounting for this loss. Frictional heat at the cold side degrades the temperature differential between hot and cold chambers and must be transferred out of the engine, but frictional heat at the hot side heat exchanger passes through the Stirling cycle again and can be partially recovered. The recoverable portion is again the conversion efficiency of the engine.

Taking into account these considerations when evaluating the losses in the engine, the next sections will cover the most important losses in the engine and how they are analyzed and accounted for.

Regenerator Ineffectiveness

The single largest source of loss in the Stirling engine is regenerator ineffectiveness. This is essentially uncaptured enthalpy that directly moves from the hot side to the cold side, without being conserved by the regenerator. In this design, the quantity of heat moving through the engine is about an order of magnitude greater than the heat flux through the heat exchangers, therefore any ineffectiveness in the regenerator is very impactful. The loss due to regenerator ineffectiveness is given by:

$$P_{ineff} = \dot{Q}_r(1 - \epsilon_r) \tag{3.21}$$

where Q_r is the heat flux through the regenerator, and ϵ_r is the effectiveness of the regenerator. According to the adiabatic model, the Q_r is roughly 3.97×10^2 kW. Even with an effectiveness of 99.8%, this equates to almost 800 W of enthalpy loss in this design.

Conduction Losses

Conduction losses are the next biggest component, and are an enthalpy loss. The most important conduction paths are through the displacer internal cylinder, through the displacer itself, and through the exterior engine wall. The displacer was designed to be hollow, with thinner walls and sufficient structural supports inside, in order to reduce the cross-sectional area for conduction. In this design, the exterior wall was designed to be a thin shell in

Conduction Path	Loss
Displacer Cylinder	233.4 W
Displacer OD Wall	118.5 W
Engine OD Wall	74.8 W

Table 3.10: Conduction path losses

order to mitigate this loss. Normally, the exterior wall must support the pressurization of the working fluid, but this design used secondary containment to maintain the elevated pressure. The equation for conductive loss is the basic formula for conduction through a solid body:

$$\Phi_q = \frac{\Delta T \sigma * A}{L} \tag{3.22}$$

Important conduction loss paths include the displacer cylinder, the displacer outer diameter wall, and the engine outer diameter wall. Conduction through the regenerator mesh is negligible, due to a high porosity and low conductivity of the regenerator material. The loss from these conduction paths is listed in Table 3.10.

Gas Flow Friction

The next biggest source of loss is gas flow frictional losses through the regenerator and heat exchanger mesh. These are work losses, since this energy must be supplied from the motion of the pistons to force the flow of gas. In this design, these components are comprised of tightly packed small-diameter fibers, and both experience oscillatory gas flow. A full analytical formulation of this type of loss would be highly complicated and require fluid dynamics modeling, but empirically-tested formulas exist in the literature and have been used for Stirling engines previously [20, 22]. The fluid flow friction through a fine mesh is given by the following set of equations:

$$f_{max} = \frac{C_{sf}}{Re_{max}} + C_{fd} \tag{3.23}$$

$$p_{max} = \rho f_{max} v_{max}^2 \frac{L_w}{2D_h} \tag{3.24}$$

$$P_{mesh} = \frac{A_o}{2} p_{max} v_{max} \tag{3.25}$$

where f_{max} is the friction factor; C_{sf} and C_{fd} are empirically determined constants, in this case $C_{sf} = 175$ and $C_{fd} = 1.6$; Re_{max} is the Reynolds number at maximum velocity, defined as $Re_{max} = \frac{D_h v_{max}}{\nu}$; p_{max} is the peak pressure drop associated with frictional drag; v_{max} is the maximum velocity; L_w is the length through the mesh; D_h is the hydraulic diameter of the mesh; P_{mesh} is the frictional power loss in the mesh; and A_o is the open area of the mesh facing the direction of flow. These equations can be applied to both the regenerator mesh and copper mesh. As can be seen from these relations, flow frictional loss scales quadratically with fluid velocity, inversely quadratically with hydraulic diameter, and, perhaps surprisingly, does not scale at first order with pressure.

Compression Loss

Another critical enthalpy loss is the gas spring compression loss, also known as gas hysteresis loss. This is caused by adiabatic heating of the working fluid during the compression portion of the Stirling cycle, raising the temperature of the fluid. This leads to additional thermal transfer loss to the environment, removing enthalpy from the fluid. This lost enthalpy must be restored by the heat exchangers to maintain the enthalpy level of the working fluid. On the expansion stroke, the fluid cools adiabatically beyond ideal isothermal behavior, requiring additional input energy to maintain temperature. This loss can be understood as a result of an expansion and compression process that is substantially faster than the rate of heat transfer of the heat exchangers. This is also the primary loss mechanism in a gas spring under sinusoidal motion. The equation for this loss is:

$$W_{comp} = \sqrt{\left(\frac{1}{32}\omega\gamma^3(\gamma-1)T_w p_{mean} k\right)}\,\left(\frac{V_m}{V_o}\right)^2 A_w \tag{3.26}$$

where ω is the cycle frequency, γ is the heat capacity ratio $\frac{c_p}{c_v}$, T_w is the temperature at the wall, p_{mean} is the mean chamber pressure, V_m and V_o are the swept and unswept volumes, respectively, and A_w is the wetted area of the chamber. Compression loss scales quadratically with the volume variation $\frac{V_m}{V_o}$, and can quickly grow if piston swept volumes are designed too high.

Channel Loss

The working gas must be forced through channels in the heat exchanger and incurs frictional loss from this motion. This forcing is provided by the pistons, and therefore is a work loss, but contributes unevenly to the overall engine loss depending on which heat exchanger is in question. Hot side friction can still be partially recovered, but cold side friction is entirely detrimental. This loss is determined from empirical formula for the friction factor along with standard gas loss equations:

$$f_{channel} = (0.79\log(Re) - 1.64)^{-2}; \tag{3.27}$$

$$p_{channel} = \rho f_{channel} v_{max}^2 \frac{L}{2D_h} \tag{3.28}$$

$$P_{channel} = p_{channel}\dot{V} \tag{3.29}$$

where L is the length of the channel, D_h is the hydraulic diameter of the channel, $\dot{V}$ is the volumetric flow rate through the channel. This loss roughly scales with the velocity squared, so keeping flow velocities low is the best method of lowering the loss. The external heat transfer fluid flows through similar channels on the external side of the heat exchanger and also obeys this set of equations.

Clearance Losses

Clearance losses refer to the losses that are caused by the clearance between a piston and its cylinder, allowing a portion of gas to convect from one side of the piston to the other. This creates loss due to two mechanisms: first, if a temperature differential exists between the two chambers, then this gas flow is an enthalpy loss from one chamber to the other. Second, if there is a pressure drop across the piston, then this flow incurs flow loss. The clearance gap around both the displacer and power piston both exhibit this loss, but each due to a different one of the mechanisms. The gap around the displacer is a direct path for mixing between the hot and cold chambers, which results in lost enthalpy that was provided by the hot-side heat exchanger and rejected by the cold-side heat exchanger without contributing to work. This clearance is not exposed to a significant pressure differential, however, and therefore does not exhibit the flow loss component. The power piston clearance does not expose a significant temperature differential, and therefore does not incur that component. Instead, it exhibits the flow loss component due to leakage of the developed pressure waveform to the ambient environment. The displacer loss is the larger of the two clearance losses, in part due to the larger gap around the displacer. The model for clearance loss is derived from [28]. First, the mass transfer is given by:

$$\dot{m} = \pi D \frac{p_1 + p_2}{4RT_g} .* (vg - g^3 \frac{p_1 - p_2}{6\mu L}) \tag{3.30}$$

where $\dot{m}$ is the mass flow rate through the gap, D is the diameter at the gap, p_1 and p_2 are the pressures on either side of the gap, R is the ideal gas constant, T_g is the average temperature in the gap, v is the velocity of the piston, g is the gap, μ is the dynamic viscosity, and L is the length of the gap. The equation for mass transfer incorporates two terms: the first term, vg, represents shear due to the motion of the piston; the second term represents flow due to a pressure differential from one side of the gap to the other. From the calculated mass transfer, the enthalpic and pressure drop losses are given by:

$$P_{PVloss} = \frac{1}{t_2 - t_1} \int_{t_1}^{t_2} \Delta p \frac{\dot{m}}{\rho} dt \tag{3.31}$$

$$\dot{H} = \frac{c_p \Delta T}{t_2 - t_1} \int_{t_1}^{t_2} \dot{m} dt \tag{3.32}$$

where P_{PVloss} is the loss from pressure drop, $\dot{H}$ is the loss from enthalpy transfer, t_1 and t_2 are the start and end times of a complete period, Δp is the pressure drop across the clearance, ρ is the density of the gas, c_p is the constant pressure heat capacity of the gas, and ΔT is the temperature drop through the gap. These equations give the two forms of loss: Equation 3.31 gives the pV loss due to pressure leakage, which applies to the power piston; Equation 3.32 gives the enthalpy loss due to sensible heat flow through the gap.

Summary of Losses

These losses are compiled in Table 3.11. These numbers are for the example design as fabricated and tested. The calculations of each of these losses were folded into the design choices and optimization described previously and informed the resultant design chosen. A full diagram of the losses and power flows from input to output streams is given in Figure 3.18. As shown in this figure, the accounting procedure for the losses differ slightly for enthalpy versus work losses, and for hot side versus the cold side losses.

To summarize: direct thermal losses from the hot-side heat exchanger to the cold-side heat exchanger, such as regenerator inefficiency or conduction loss, are not as detrimental as losses that must be subtracted from work output because they represent unconverted energy and are therefore discounted by the conversion efficiency. Work losses are those losses that are subtracted from the developed output work, such as the energy required to overcome flow friction. The localized heating from these losses has different effects depending on the proximate chamber. Frictional heating at the cold side must be rejected to the ambient environment, but frictional heating at the hot side adds to the enthalpy in that chamber, and therefore is recycled back into the Stirling cycle. Flow friction through the regenerator is divided between the hot and cold chambers in accounting to represent the fact that this component straddles the hot and cold chambers. Each loss component is listed in its undiscounted value; the last line discounts and sums each loss accordingly, so is therefore stated in values comparable to output pV work.

Loss Mechanism	Enthalpy Loss	Mechanical Loss
Regenerator Ineffectiveness	794 W	
Regenerator Flow Friction		135 W
Heat Exchanger Flow Friction (Hot Side)		11.5 W
Heat Exchanger Flow Friction (Cold Side)		12.5 W
External Fluid Flow Friction (Hot Side)		13.7 W
External Fluid Flow Friction (Cold Side)		18.1 W
Hot Side Channel Flow Friction		74.2 W
Cold Side Channel Flow Friction		97.7 W
Compression Loss		62.9 W
Displacer Clearance Loss	201 W	
Power Piston Clearance Loss		21.5 W
Conduction Loss	426.7 W	
Total Enthalpy Loss	1421.7 W	
Discounted Enthalpy Loss	284.34 W	
Total Mechanical Hot Side Loss		198.7 W
Discounted Mechanical Hot Side Loss		156.0 W
Total Mechanical Cold Side Loss		249.1 W
Total Effective Output Loss		732 W

Table 3.11: Accounting of losses in Stirling engine design. Enthalpy losses are differentiated from mechanical losses and are discounted by the conversion efficiency, η. Mechanical losses are separated into cold side and hot side losses, with hot side losses partially converted through the cycle process and discounted by $(1-\eta)$. The total effective loss is the summation of these terms.

Design Scaling

Given the example design described herein for a specific power output, an important discussion is the scaling of the design to different power outputs. Such scaling can be accomplished by changing a number of different design parameters, but each change will affect performance and incur losses in different ways. These scaling options will be discussed along with their first-order effects on performance.

Increasing the cycle frequency and the working fluid pressure are both canonical ways to increase Stirling engine power output. However, they affect performance in different ways and there are important implications for the choice of scaling for each. To first order, both increase power output linearly, as is seen in the well-known Beale number, which is defined as:

$$B_n = \frac{W_o}{PVf} \tag{3.33}$$

where W_o is the power output, P is the working fluid pressure, V is the swept volume, and f is the cycle frequency. The PVf product contains the three primary scaling factors for a given temperature input, and so the Beale number is a measure of performance of the engine. While this number is useful as an approximate comparison of engines, it is not as useful for the purposes of optimizing a design precisely because of its approximate nature.

Scaling up either pressure or frequency to increase the power output of an engine has different effects on actual performance. Scaling up frequency increases the mean gas flow velocity; this tends to increase flow frictional losses, since these losses scale as the velocity cubed. Scaling up pressure does not increase most losses to the same degree as frequency; indeed, frictional losses through mesh structures are surprisingly independent of pressure. However, higher pressure imposes more stringent requirements for the structural design of the engine. The displacer and engine walls must be properly sized to contain the pressure, which requires thicker walls and therefore causes more conduction loss and also increases the cost of components. Therefore, while scaling up engine pressure is locally a better choice than frequency, the costs and constraints on scaling up pressure tend to be nonlinear and can quickly increase based on thresholds. In general, the optimal design first scales pressure up within the limit of practical pressure containment requirements. Frequency can then be scaled to achieve the desired power rating.

Scaling up swept volume is best understood as a combination of scaling up engine size and piston stroke length. Keeping the engine size constant, scaling up power piston swept volume increases the fraction of PV potential extracted each cycle, and is somewhat analogous to increasing the compression ratio of a Brayton cycle. In addition, the swept volume is only useful when compared with the total volume of the working fluid, which includes dead volume, or volume that is not swept by the piston. It is the ratio of swept volume to total volume that determines the power extraction each cycle. However, increasing this compression fraction increases the compression loss quadratically, which increases faster than the linear growth in power extraction. Therefore, the compression fraction should be optimized rather than simply increased to its practical limit.

If the compression fraction is kept constant, but instead the overall size of the engine is increased, then this nominally increases power output linearly. However, this is only true as a local first-order approximation. Many key components in a Stirling engine do not scale well by simply increasing the size of the engine. Heat exchangers are fundamentally operative over a surface area, and surface area scales quadratically with length scale, while volumes scale cubically. Therefore, a naive scaling of lengths will degrade heat exchanger performance in relation to power output. In the case of the design discussed herein, the heat exchangers are planar and could be scaled in the plane to keep a constant ratio of heat exchanger surface area to working fluid volume, or the orthogonal length can be reduced to increase the ratio of heat exchanger surface area to working fluid volume. This is how heat exchanger performance is improved to address stringent requirement at low temperature differentials. However, this approach is also fundamentally limited by flow throughout the heat exchangers. As the planar design is widened, the working fluid must travel farther from the central displacer to the heat exchanger extremities. This increases flow frictional losses, increases dead volume (which reduces compression fraction), and leads to thermal anisotropy throughout the heat exchanger surface - i.e. a uniform temperature is no longer maintained throughout the heat exchanger structure, which negatively impacts heat transfer. These issues quickly outpace the additional benefit gained; therefore, this type of scaling is also limited. Ultimately, there is a fundamental limit to Stirling engine scaling by size, regardless of geometry.

3.10 Pressurization

Engine pressurization is a significant design challenge for Stirling engines. Pressurization typically presents two problems: containment and thermal loss. Containment requires designing the external wall of the engine to be sufficiently strong to contain the pressurization with a safety factor, and designing the bearings and other openings to both withstand the pressure differential and prevent leakage. Strong structural components typically require higher thicknesses, which increase conduction loss from the hot side to the cold side.

In this design, the engine is enclosed in a pressure vessel as a secondary containment structure. This allows the engine wall to be drastically thinner, as it only has to contain the variable pressure in the working fluid due to the Stirling cycle, which roughly equals 3 bar. The average pressurization of 30 bar is instead handled by the secondary containment structure, which can be designed without exacerbating conduction losses. This likewise also eliminates sealing challenges with bearings, since the pressure differential is reduced to a minimal amount. The engine wall was designed as a split thin 1/16th Inch steel shell, with a clamping mechanism at the split. Conduction losses for this component are greatly reduced at this thickness. The engine wall can be seen in Figure 3.16, which also shows the rest of the engine assembled. The wall clamps around the perimeter of the engine, with a rubber gasket at the top and bottom interfaces to aid in sealing.

The drawback of this approach is the additional cost of the secondary containment struc-

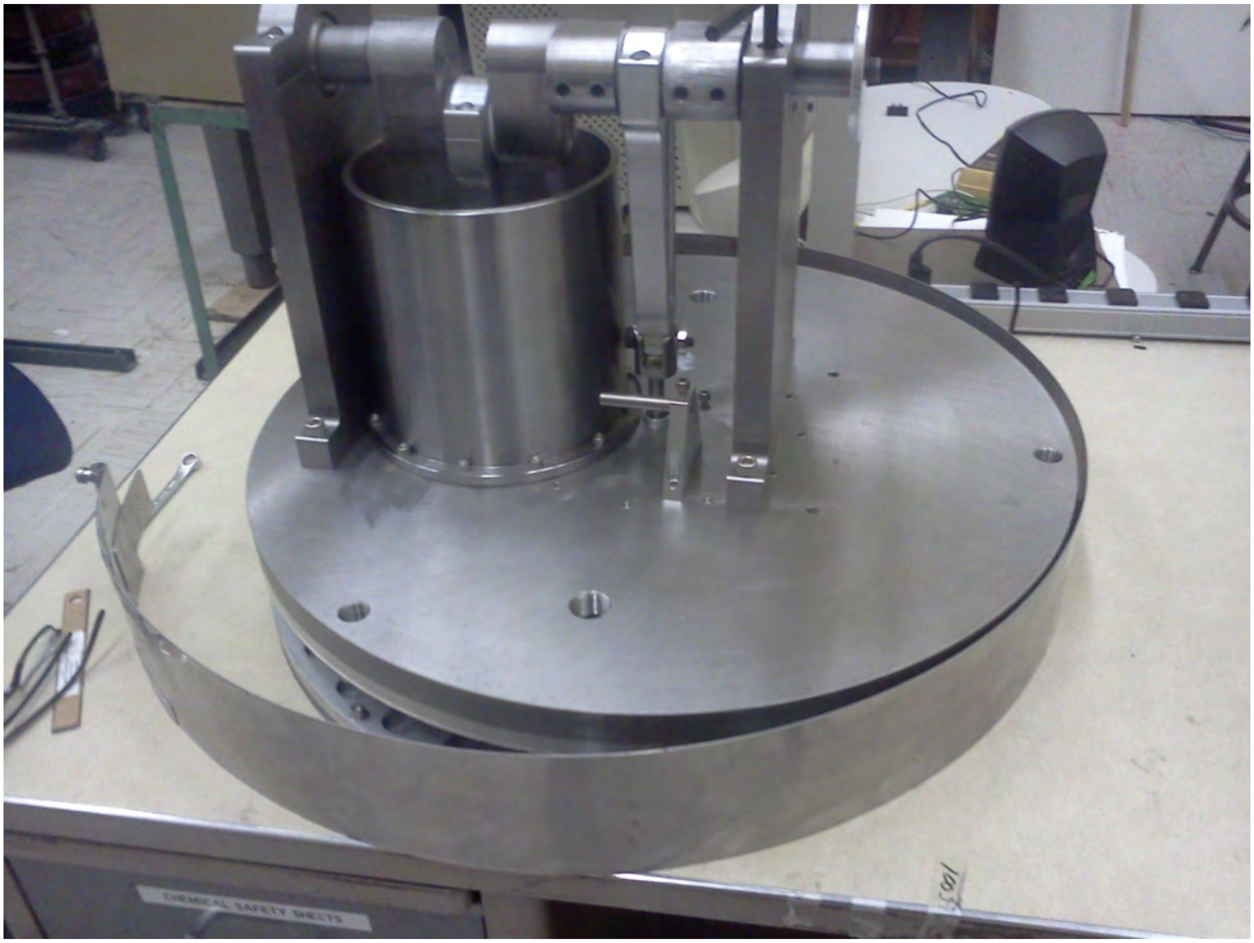

Figure 3.16: The engine core assembled with the outer wall.

ture. The containment structure for this design was greatly oversized, both for additional safety as well as to accomodate necessary research instrumentation and flexibility that would not be necessary in a commercial design. The use of the secondary containment structure, instead of an integrated single-containment design, aided in the experimental process by eliminating the need for sealing on instruments inside the engine, instead moving wire seals to the secondary containment vessel, where greater space and flexibility were available. The vessel was also designed with a removable bottom hemisphere that housed the engine to aid in repeated removal from the vessel. The top portion was firmly bolted down and structurally supported the entire apparatus. A drawing of the pressure vessel and a picture of the fabricated vessel are shown in Figure 3.17.

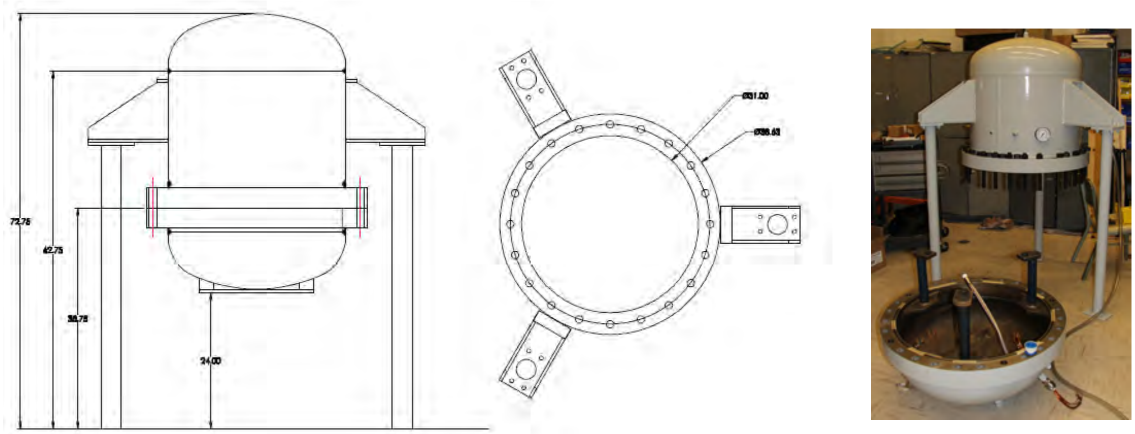

(a) Drawing

(b) Picture

Figure 3.17: Drawing and picture of the fabricated pressure vessel.

3.11 Prototype Design

Throughout this chapter, the constellation of heat fluxes and losses have been discussed individually. These are compiled into an energy flow diagram for clarity, shown in Figure 3.18. This diagram shows the flows of energy throughout the Stirling engine, from thermal energy as an input to pV work output and rejected thermal energy output. Losses are shown as flows that are subtracted from power quantities to best represent their physical path and effect. Colors are only illustrative of temperature, and should not be taken quantitatively.

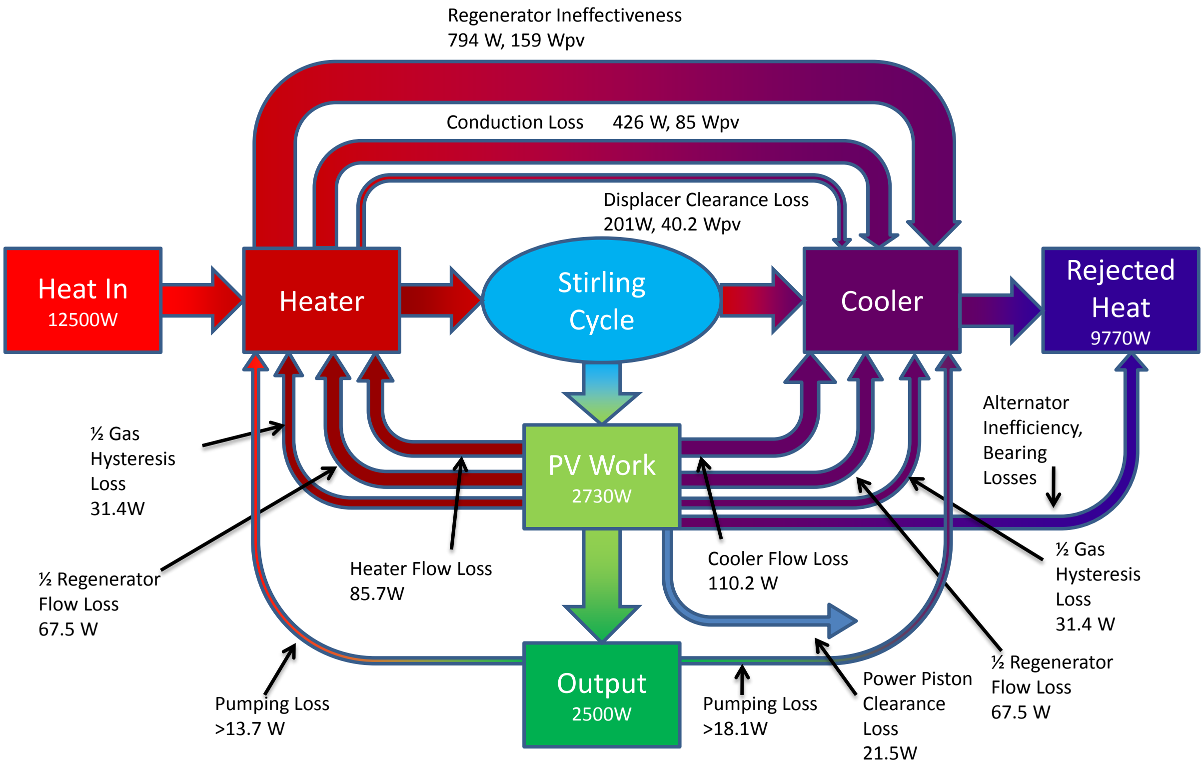

Figure 3.18: Energy flow diagram showing the path of energy from input to output and work, including loss paths.

Important engine design parameters for the 2.5 kW engine are listed in Table 3.12. Photographs of the assembled engine are shown in Figure 3.19.

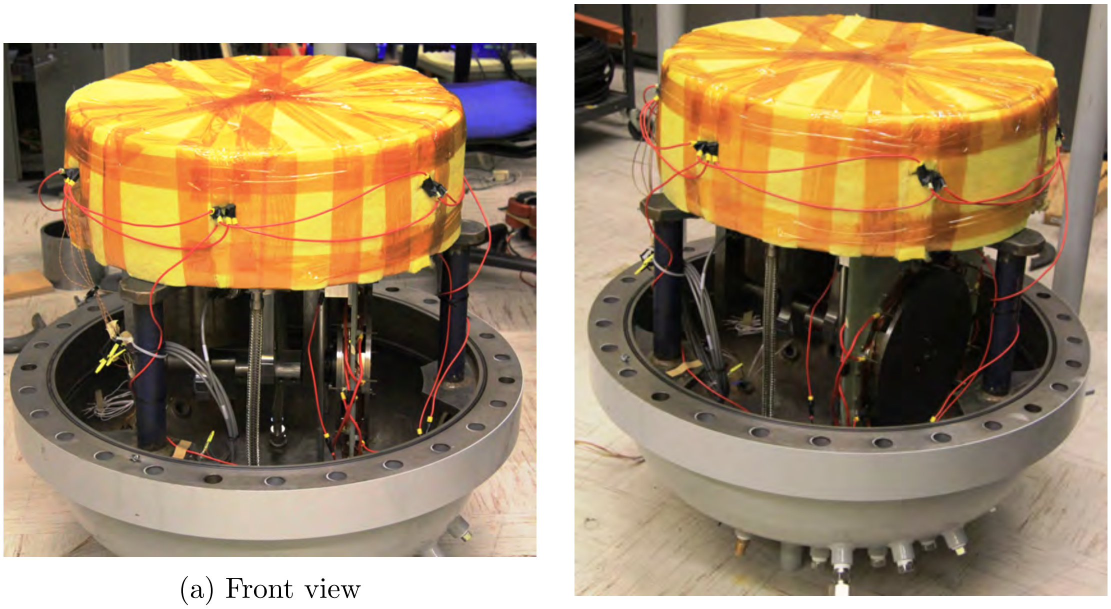

(a) Front view

(b) Oblique view

Figure 3.19: Photographs of assembled engine with front and oblique view.

Rated Work Output	2.5 kW
Conversion Efficiency	20%
Fraction of Carnot Efficiency	60%
Hot-Side Temperature	180 °C
Cold-Side Temperature	30 °C
Pressurization	30 bar
Cycle Frequency	20 Hz

Table 3.12: Temperature drops

Chapter 4

Electrical Conversion and Motor Control

4.1 Alternator Design

Conversion from mechanical power developed by the Stirling Cycle into electrical power requires an alternator. In this engine, an integrated custom alternator was designed in order to fit within the geometric constraints of the pressure vessel, achieve high torque at low speed in order to start the engine, and to achieve low losses. The alternator design used in this prototype is a permanent magnet, coreless 8-pole machine. The coreless permanent magnet design allows high torque at low speed and eliminates core losses. The choice of 8 poles allows a symmetric winding arrangement that minimizes end turns and wasted gap space.

The available space in the pressure vessel forces a thin low-profile design for the alternator. This, along with the simplicity of design, makes the axial flux machine configuration compelling. The magnets selected were N42 grade NdFeB, with a residual flux density B_r of $1.32\,\mathrm{T}$ and a gap flux density of about $0.66\,\mathrm{T}$. A picture of the magnet rotor is shown in Figure 4.1.

The windings were constructed from Litz magnet wire and arrayed on two separate halves, then assembled together. The end turns from each half were arrayed out of the plane, to allow wires on both halves to fully occupy the gap space. The winding assembly is shown in Figure 4.2. This design used litz magnet wire with 81 strands of 33 gauge wire per bundle. The winding packing factor, defined as the fraction of copper to total cross-sectional area at the inner radius of the winding region, is approximately 0.26. The total series resistance of each phase is $0.24\,\Omega$.

The full rotor and stator assembly is shown in Figure 4.3. The two rotor discs are assembled around the winding assembly through a coupler shaft in the center hole.

The design of the windings first used an FEM simulation of the magnetic components to generate flux data over the gap space. Since the stator components are non-magnetic, the magnetic fields were stationary relative to the reference frame of the rotor. The flux

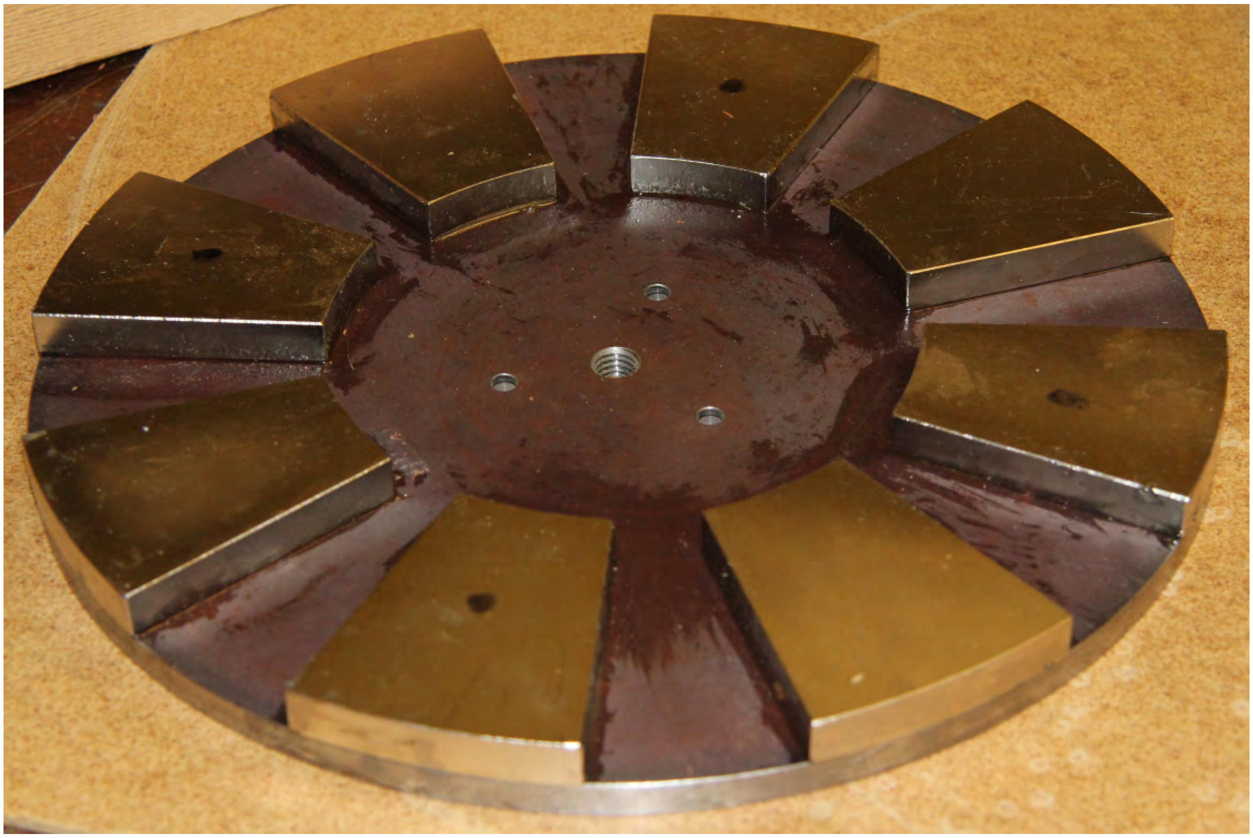

Figure 4.1: One disc of the magnet rotor. The full rotor is assembled with two facing discs.

data was then used in a Matlab simulation to calculate the EMF on various arrangements of windings. The magnet winding configurations were optimized in this way to maximize the effectiveness of the alternator, represented by the $\frac{V^2}{R}$ metric, there V is the voltage induced and R is the resistance of the windings. The V in this metric must be chosen appropriately for the application. For most applications, choosing V as the amplitude of the fundamental voltage component is appropriate, as the fundamental is the frequency component that is effectively harnessed. If higher order harmonics can be effectively harnessed as well, such as if the application is a simple resistive heater, then a more inclusive V can be used in the metric.

Geometry Optimization

The axial flux machine presents some unique design considerations compared to traditional radial flux machines. One important difference is that the magnetic flux over the magnet region does not contribute equally to the EMF, with flux at the outer radius being more effective due to the higher velocity. An important design choice is the radial depth of the magnet space - i.e. given an outer radius for the magnets, what inner radius maximizes

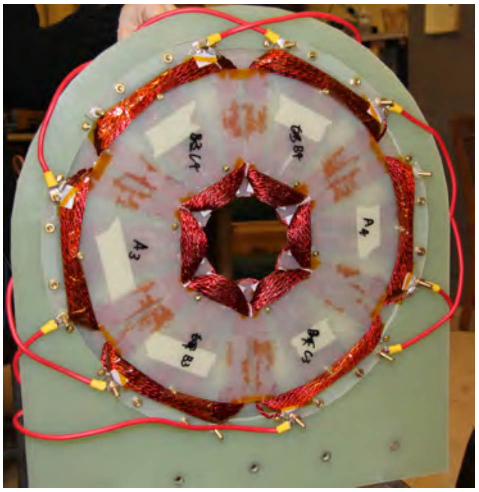

Figure 4.2: The assembled winding structure. The two winding halves were assembled facing each other on the support structure.

performance? Given some assumptions about the shape and structure of components, an optimal aspect ratio can be determined.

This analysis can be generalized regardless of radial scale. Thus the magnet aspect ratio factor, k_d, is defined as the ratio between the inner radius of the magnets and the outer radius, $\frac{r_i}{r_o}$. The magnets are assumed to be sectors of an annulus with the given outer and inner radii, placed at the corresponding location on the rotor disk. Additionally, m is defined as the number of phases, p as the number of poles, s as the number of slots per phase (two slots per coil), and N as the number of turns in a slot. The winding structure is mechanically slotless, but the analysis refers to slots as wire bundles analogously with slotted designs. To evaluate the performance of the machine, $\frac{V^2}{R}$ is used as the metric of performance, where V is the fundamental frequency component of voltage and R is the winding resistance. Both of these quantities need to be analytically calculated to optimize the design.

Only the axial component of the B-field is relevant to the windings, with torque-producing sections arrayed in the radial direction. The following discussion refers only to this component of the B-field. Furthermore, the sinusoidal fundamental component of the magnetic field is what contributes to the fundamental component of the back EMF, therefore the B-field over the magnet region can be approximated as varying sinusoidally in the azimuthal direction for this analysis. In other words, the B-field can be expressed as:

$$B(\theta) = B_{\text{peak}} cos(p\theta) \tag{4.1}$$

The RMS value of the B-field rather than the peak is used for direct calculation of the RMS EMF. Additionally, the B-field differs over the span of each slot, and the EMF is calculated from integration over the slot, which derates the effective RMS value by an integration factor. Therefore the B-field can be expressed as an effective B value for the

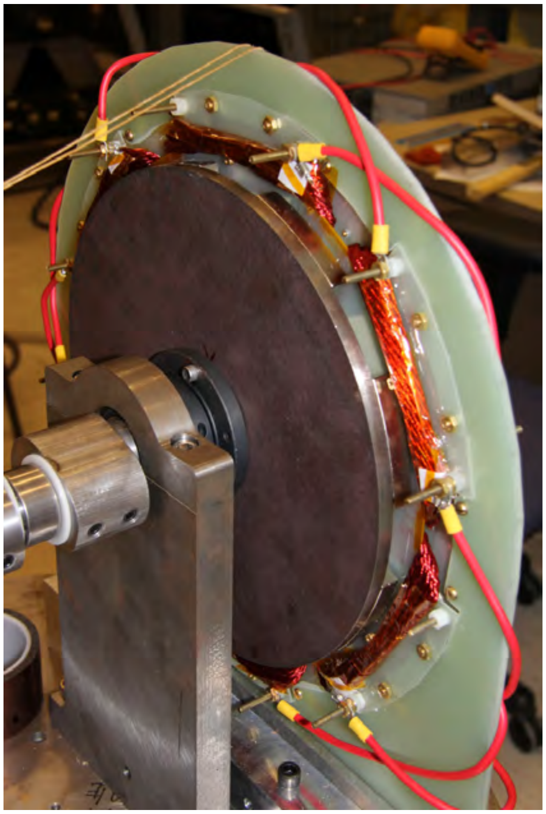

Figure 4.3: The full rotor and stator assembled on the engine crankshaft.

purposes of this analysis, given by:

$$B_{\text{eff}} = \frac{B_{\text{peak}}}{\sqrt{2}} \frac{m}{\pi} \int_{-\frac{pi}{2m}}^{\frac{pi}{2m}} cos(\theta)\, \mathrm{d}\theta = B_{\text{peak}} \frac{2m}{\pi\sqrt{2}} sin\left(\frac{\pi}{2m}\right) \tag{4.2}$$

where B_{eff} is the effective B-field used for calculation of the RMS back EMF, B_{peak} is the peak B-field, and m is the number of phases. For the N42 magnets selected, this evaluates to a B_{eff} value of $0.456T$. Using the field data obtained by a magnetic FEA in Comsol, an integration of the windings and over the motion of the rotor yields the effective flux linkage per turn over the slot as a function of position in Figure 4.4a. A harmonic decomposition, shown in Figure 4.4b, indicates that the flux density field is relatively free of higher harmonics. The B-field is also assumed to be approximately constant over the radial span from r_i to r_o; according to FEA results, the actual variation with radius is under 3% in this region.

From this model of the B-field, the back-emf over a slot is given by:

$$V_{\text{slot,eff}} = \frac{1}{2} B_{\text{eff}} N r_o^2 (1 - k_d^2)\omega \tag{4.3}$$

where N is the number of turns in the slot, r_o is the outer radius of the active region of the winding (equivalent to the outer diameter of the magnets), k_d is the aspect ratio factor $\frac{r_i}{r_o}$,

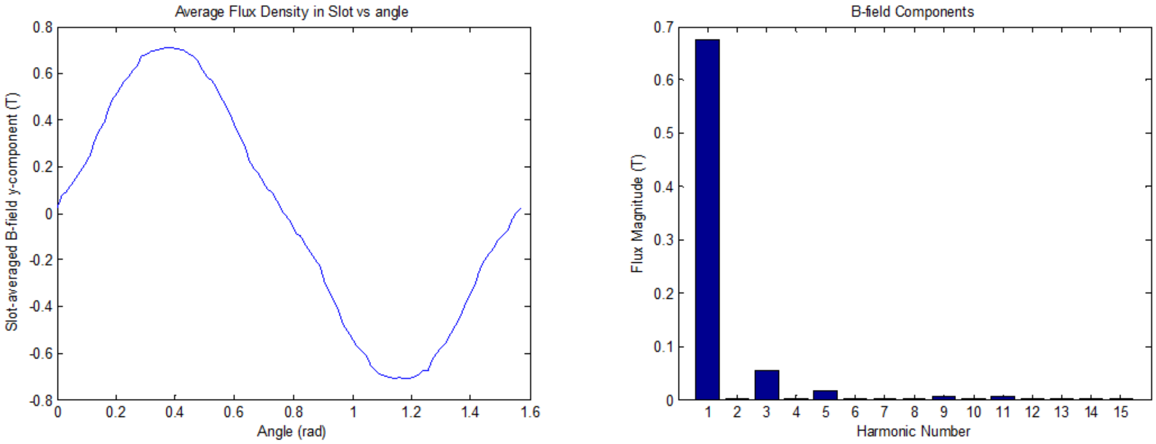

(a) (b)

Figure 4.4: (a) Effective flux density versus rotor angle from simulation and FEA. (b) Fourier decomposition of (a) expressed as multiples of the fundamental frequency.

and ω is the angular velocity of the motor. From this, the phase back-emf voltage can be calculated by:

$$V = \frac{s}{2} B_{\text{eff}} N r_o^2 (1 - k_d^2) \omega \tag{4.4}$$

To calculate the winding resistance, first note that each slot is arrayed radially but is limited by the slot space available at the inner radius. The length and cross-sectional area of each turn of conductor in a slot are given by:

$$L = (r_o - r_i) k_{we} \tag{4.5}$$

$$A = \frac{2\pi r_i}{smN} d k_w \tag{4.6}$$

where d is the thickness of the slot in the axial direction, k_{we} is an end-turn factor that includes the length of inactive wire length, and k_w is a winding packing factor that represents the fraction of total available cross-sectional area covered by conductor. In the fabrication of this winding, k_w was approximately 0.26.

The resistance per turn in terms of the length and and cross-sectional area is then given by:

$$R_{turn} = \frac{L\rho}{A} \tag{4.7}$$

Each winding phase consists of s windings of N turns each, therefore the total phase resistance is given by:

$$R_{phase} = \frac{sNL\rho}{A} \tag{4.8}$$

The end turns are arrayed azimuthally at both the inner and outer radius, therefore the additional end-turn factor k_{we} is given by:

$$k_{we} = \frac{(1-k_d) + \frac{4\pi}{sm}(1+k_d)}{1-k_d} = 1 + \frac{4\pi}{sm}\frac{(1+k_d)}{(1-k_d)} \tag{4.9}$$

Plugging this equation and the equations for length and cross-sectional area into the phase resistance equation, and making the substitution $k_d = \frac{r_i}{r_o}$, the expanded equation for phase resistance is given by:

$$R_{phase} = \frac{s^2 m N^2 \rho}{2\pi d k_w}\left(\frac{1-k_d}{k_d}\right)\left(1 + \frac{4\pi}{sm}\frac{(1+k_d)}{(1-k_d)}\right) \tag{4.10}$$

From this and the EMF per phase, the $\frac{V^2}{R}$ metric is given by:

$$\begin{aligned}
\frac{V^2}{R} &= \frac{\frac{s^2}{4}B_{\text{eff}}^2 N^2 r_o^4 (1-k_d^2)^2 \omega^2}{\frac{s^2 m N^2 \rho}{2\pi d k_w}\left(\frac{1-k_d}{k_d}\right)\left(1 + \frac{\pi}{sm}\frac{(1+k_d)}{(1-k_d)}\right)} && (4.11)\\
&= \frac{\pi B_{\text{eff}}^2 N^2 r_o^4 \omega^2 d k_w}{2m\rho}\frac{(1-k_d^2)^2}{\left(\frac{1-k_d}{k_d}\right)\left(1 + \frac{\pi}{sm}\frac{(1+k_d)}{(1-k_d)}\right)} && (4.12)\\
&= \frac{\pi B_{\text{eff}}^2 N^2 r_o^4 \omega^2 d k_w}{2m\rho} k_a r && (4.13)
\end{aligned}$$

where $k_a r$ is defined as the aspect ratio factor $k_a r = \frac{(1-k_d^2)^2}{\left(\frac{1-k_d}{k_d}\right)\left(1+\frac{\pi}{sm}\frac{(1+k_d)}{(1-k_d)}\right)}$. $k_a r$ is independent of most machine parameters, such as the B-field, motor speed (ω), overall radius (r_o), and slot thickness (d); the only dependent parameters are the slots per phase, s and the number of phases, m. Therefore, maximizing $k_a r$ offers general insight into the optimal geometry of the machine.

For the axial flux machine designed for this Stirling engine, there are three phases and eight poles, therefore $s = 8$ and $m = 3$. Given these parameters, the aspect ratio factor $k_a r$ is maximized at $k_d = 0.51$ - in other words, when the inner radius of the magnet and winding space is half of the outer radius. The value of this aspect ratio factor over the range of aspect ratios is shown in Figure 4.5, showing the maximal value of $k_a r$ can be seen to occur at $k_d = 0.51$. If the minimization of magnet volume is desired, then an additional magnet volume factor can be included, which further drives $k_a r$ higher to approximately 0.67, as shown in Figure 4.6. These conclusions agree with similar analysis in [19].

Alternator Losses

There are three main sources of loss in this alternator design: resistive winding losses, eddy current losses, and windage frictional losses. The resistive winding losses are simply given

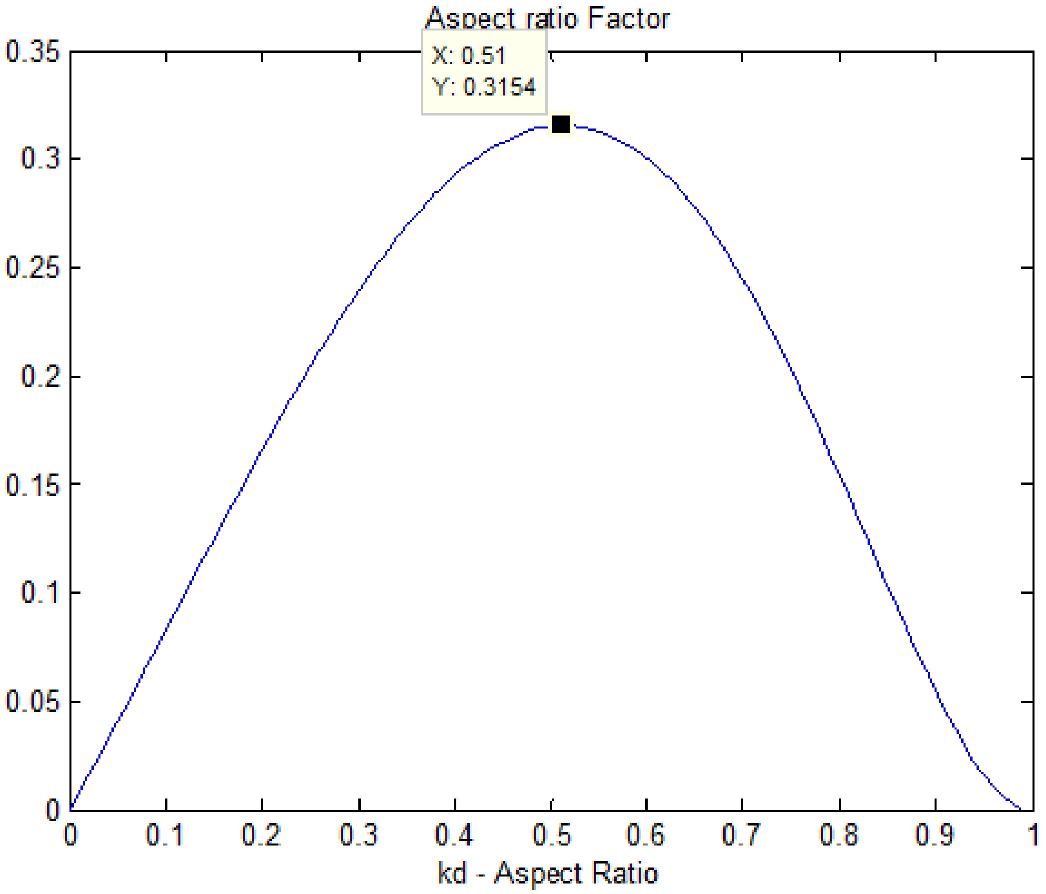

Figure 4.5: The value of $k_a r$ over varying aspect ratios reaches a maximum at approximately $k_d = 0.51$.

by:

$$P_\Omega = \frac{1}{2} I^2 R_w \tag{4.14}$$

where I is the current in the windings and R_w is the resistance of the windings. This is calculated for each phase and summed together. The design and optimization around the V^2/R metric already serves to minimize the quantity of these losses. A first-order estimate of the resistance of the windings was $112\,\mathrm{m}\Omega$. This, however, only accounts for the core resistance component of the windings; it did not account for contact resistances and additional wire length for interconnecting windings and

Eddy current losses occur due to small circulating currents in conductors caused by changing magnetic fields. Since there is no stator back-iron, the only conductor that contributes eddy losses are the copper wires. The wires were chosen as fine-strand litz wire bundles, with individual strands of 30 gauge wire, in order to manage eddy current losses. The equation

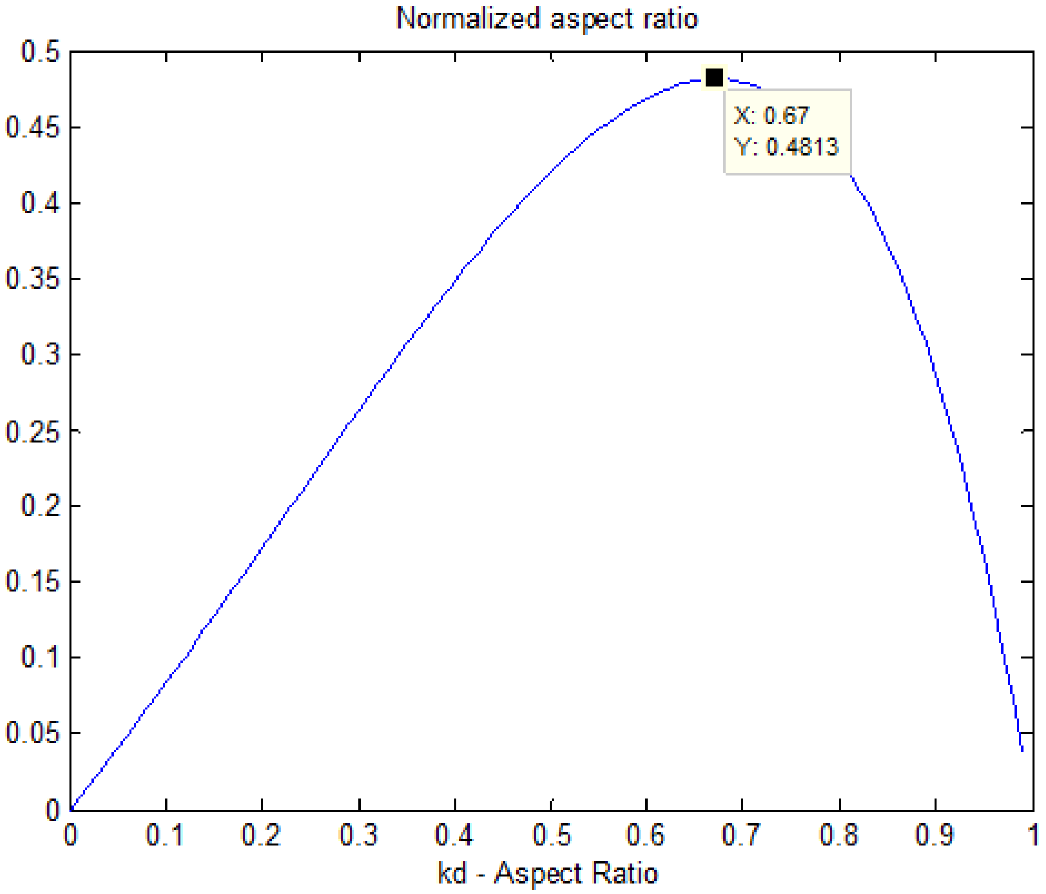

Figure 4.6: The aspect ratio factor normalized by magnet volume.

for eddy current loss is given by [28]:

$$P_{eddy} = \frac{1}{16}\sigma\omega^2 d^2 V_{cond} \sum_{n=1}^{\infty} n^2 \left(B_{myn}^2 + B_{mzn}^2\right) \tag{4.15}$$

where σ is the conductivity of the material, ω is the angular frequency of alternating magnetic fields (which is not the same as the engine cycle frequency), d is the diameter of the conductors in the gap, V_{cond} is the volume of conductors, n is the harmonic order number, and B_{myn} and B_{mzn} are the harmonic components of the magnetic flux density that are transverse to the conductor. The flux density component that is parallel to the conductor is negligible due to the small cross-section of the wire. With a good magnetic design in which flux at the windings is almost entirely oriented in the axial direction, as is the case with this machine, the B_{mzn} component is also negligible and can be ignored. The summation in the equation is over the harmonic orders of the flux density, with higher order harmonics scaling up quadratically with the order. The eddy current losses for this machine are calculated to be below 2 W.

Windage losses are frictional losses from moving air, caused by the relative motion of the rotor.

$$P_{windage} = \frac{\pi\omega^2\mu(r_o^4 - r_i^4)}{2g} \tag{4.16}$$

where ω is the mechanical angular frequency of the rotor, μ is the dynamic viscosity of the air between the rotor and stator, and g is the air gap between the rotor and stator. For the electric machine at hand, the windage losses were conservatively estimated to be less than 0.08 W, and therefore negligible. Magnetic core losses are also a signficiant component of loss in typically motor-alternators, but since the stator is coreless in this design, this source of loss is negligible.

4.2 Drive Controls

The Stirling engine required the development of custom motor drive controls to overcome the challenges associated with startup. A commercially-available motor drive was initially used, but was unable to start up the Stirling engine due to a high torque requirement at low speed. This is due to the significant force required to initially compress the gas volume of the engine in order to complete the first half-cycle of the engine. This compression requires a large activation energy to be overcome at startup. The controls developed to overcome this challenge and to run the Stirling engine during normal operation are described in this section.

While this compression energy is a significant challenge for startup, it is mitigated during operation by the design of the power piston as a resonant system. The gas volumes and power piston mass were specifically chosen to form a resonant mass-spring system at the nominal operating frequency, therefore minimal drive is required to sustain motion. In addition, when a temperature differential is present and the displacer is activated, the Stirling cycle provides a thermodynamic driving force that biases the engine toward the forward (generation) direction. This effect also serves to reduce drive requirements during nominal operation, but not during startup. Therefore, the most challenging part of the motor drive is startup. To address the challenge of startup, a custom mechanically-resonant PWM drive was developed to overcome this initial barrier.

It should be noted that the engine at rest had the power piston in the fully expanded state. This added to the startup challenges by requiring even greater initial compression to begin engine motion. An alternate configuration could have allowed the power piston to begin in a neutral compression position when at-rest, and would have eased the startup compression required. Nonetheless, the development of the custom resonant startup drive is relevant even in that case, as the compression forces required are still high.

The motor controls were implemented on a National Instruments sbRIO-9632, a board that combines an FPGA with a real-time operating system on a microcontroller. The control algorithms were developed and programmed through LabView. The core of the control code ran on the FPGA, while the real-time OS was used for management, configuration, HMI, and data logging. The control algorithm used measurements of three-phase voltages and currents at the motor terminals in a sensorless scheme and generated PWM signals to run a custom lab inverter. An observer was used to estimate the phase angle of the motor based on three-phase voltage measurements.

The controls had three stages of operation. The initial stage was simply an open-loop impulse to generate enough motion for the observer to lock on. The second stage is a resonant startup mode designed to overcome the compression work required to begin spinning. Rather than attempting to produce high torque at low speed to overcome compression forces, the drive added energy at the resonance of the piston motion. This leveraged the behavior of the piston and gas spring as a mass-spring system to gradually impart energy into the system over the course of multiple cycles. By adding energy at the resonance of the system, the total activation energy required to begin normal operation could be added incrementally at lower torque over a longer period of time. The energy of the system is increased over the course of multiple cycles, gradually increasing the swing amplitude, until there is sufficient energy to overcome the compression barrier. The final stage of operation is normal engine operation, and takes place after the piston has built up enough momentum for sustained rotation. These controls will be discussed in the following subsections.

System Equations

First, the Stirling engine, motor/alternator, and electrical interface will be described by a set of state equations in a dynamical state-space system model. These three subsystems are each described by differential equations, which when combined characterize the behavior of the overall system. The state variables in these system equations are the angular position of the engine, θ, the angular velocity of the engine, ω, and the three-phase current in the electrical circuit, i.

The Stirling engine mechanical system is modeled as a rotating mass with rotational inertia and frictional damping, along with PV forces from the Stirling cycle and gas spring. The motor contributes torque to the system, leading to the following engine equation:

$$J\frac{d}{dt}\omega + b\omega + k_c \sin\theta = \tau_m + \tau_S(\theta) \tag{4.17}$$

where J is the rotational inertia of the engine, θ is the engine angular position, with angle 0 designated as the central position of the power piston, b represents frictional damping forces, k_c is the effective gas spring constant, τ_m is the applied motor torque, and $\tau_S(theta)$ is drive from the Stirling cycle conversion between thermal and mechanical energy, and is negative for the engine operating in motor mode and positive for generation mode.

The gas spring and Stirling drive terms, $k_c \sin\theta$ and $\tau_S(\theta)$, comprise the combined PV forces of the working fluid in the Stirling engine. The PV forcing of the Stirling cycle is disaggregated in this manner to represent real and reactive components of the cycle, in much the same way that AC power can be real and reactive. The gas spring term contributes forces throughout the cycle, but imparts zero net energy over a cycle, aside from losses, and is therefore analogous to reactive AC power. This term represents the component of gas forces that would still be present even in the absence of a temperature differential, and therefore without any thermal energy conversion. The Stirling cycle conversion drive term is the core energy conversion process of the Stirling engine, and is manifested as additional PV forces (on top of gas spring forces) from thermal energy transfer into or out of the working fluid. This is analogous to real power in an AC system, since it represents the power that is converted and delivered during the net Stirling cycle.

The electrical circuit includes the three-phase inverter and the motor/alternator, which is represented by a back-emf and a series resistance and inductance. The equation for the electrical circuit is:

$$L\frac{d}{dt}i + Ri = V_i - V_e \tag{4.18}$$

where L is the per-phase inductance between the motor and inverter, R is the per-phase resistance, V_i is the inverter voltage, i is the current, and V_e is the back-emf. Since the motor/alternator is a three-phase machine, the voltages and currents in this equation are three phase vectors, representing three circuits, but written here as one for simplicity.

The mechanical and electrical state equations are coupled together through the equations for the motor/alternator, which is represented by a motor back-emf and torque with the following equations:

$$\tau_m = k_t i \tag{4.19}$$

$$V_e = k_e \omega \tag{4.20}$$

$$\tag{4.21}$$

where k_e is the back-emf constant, and k_t is the torque constant. Note that the back-emf and torque constants are numerically equal when expressed in SI units.

Combining these equations into a state space model gives the following:

$$\frac{d}{dt}\theta = \quad \omega \tag{4.22}$$

$$\frac{d}{dt}\omega = \frac{-b}{J}\omega + \frac{k_c \sin\theta}{J} - \frac{k_t}{J}i + \frac{\tau_S(\theta)}{J} \tag{4.23}$$

$$\frac{d}{dt}i = \frac{-k_e}{L}\omega + \frac{-R}{L}i + \frac{1}{L}V_i \tag{4.24}$$

$$\frac{d}{dt}\theta = \quad \omega \tag{4.25}$$

$$\tag{4.26}$$

Or expressed in matrix notation:

$$\frac{d}{dt}\begin{bmatrix}\theta\\ \omega\\ i\end{bmatrix}=\begin{bmatrix}0 & 1 & 0\\ 0 & \frac{-b}{J} & \frac{k_t}{J}\\ 0 & \frac{-k_e}{L} & \frac{-R}{L}\end{bmatrix}\begin{bmatrix}\theta\\ \omega\\ i\end{bmatrix}+\begin{bmatrix}0\\ 0\\ \frac{1}{L}\end{bmatrix} \tag{4.27}$$

In this model, the motor is modeled as a combination of a back-emf component, a resistive component, and an inductive component. The back-emf component represents the electromotive force of the motor/alternator and increases proportinally with engine frequency, multiplied by the number of pole pairs in the motor/alternator. The winding inductance was measured to be (171 µH) and the winding resistance was measured to be 240 mΩ. Within the operating range of the Stirling engine, from low frequency startup to a peak electrical frequency of 80 Hz, the impedance of the motor windings is predominantly resistive. This differs from typical motors, which tend to be dominated by winding inductance, and is a result of the coreless design of the motor windings. These measured impedances were modeled in the control loop parametrically, and used to calculate a winding voltage drop that is then subtracted to estimate the back-emf rotor voltage V_r. This rotor voltage was used in the calculation of control signals.

Two-Phase Representation

In a three-phase system, there are two degrees of freedom for AC voltages and currents around a DC common mode, and therefore three-phase information can be fully represented by two AC values and an offset. These are obtained by a transformation from three-phase space to a two-phase vector, called the Clarke Transformation. This helps simplify control algorithms, and is commonly used in motor control algorithms. The two-phase coordinate system generated by the Clarke Transformation is by convention labeled $\alpha\beta\gamma$ coordinates [6]. The $\alpha\beta\gamma$ representation combines a two-dimensional vector represented by α and β components and an common-mode offset represented by γ. The γ component is nominally zero in a balanced three-phase system. As long as voltages are referenced to the three-phase neutral, and there are no alternate paths for currents to flow, then three-phase voltages and currents sum to zero and the γ component is not needed for controls. The Clarke transformation is given by the following equation:

$$\begin{bmatrix}X_\alpha\\ X_\beta\\ X_\gamma\end{bmatrix}=\frac{2}{3}\begin{bmatrix}1 & -\frac{1}{2} & -\frac{1}{2}\\ 0 & \frac{\sqrt{3}}{2} & -\frac{\sqrt{3}}{2}\\ \frac{1}{2} & \frac{1}{2} & \frac{1}{2}\end{bmatrix}\begin{bmatrix}X_a\\ X_b\\ X_c\end{bmatrix} \tag{4.28}$$

where X is the type of quantity being transformed, namely voltage V or current I, and the a,b,c subscripts refer to three-phase quantities and α,β,γ subscripts refer to transformed quantities. As mentioned above, for balanced three phase systems, the γ component is zero and the transformed coordinates are effectively two-dimensional. The equation can be rewritten in terms of line-to-line quantities, since the measured voltages were line-to-line. Therefore, the transformation equations for voltage and current are:

$$\begin{bmatrix} V_\alpha \\ V_\beta \end{bmatrix} = \begin{bmatrix} \frac{2}{3} & -\frac{1}{3} \\ 0 & \frac{1}{\sqrt{3}} \end{bmatrix} \begin{bmatrix} V_{ac} \\ V_{bc} \end{bmatrix} \tag{4.29}$$

$$\begin{bmatrix} I_\alpha \\ I_\beta \end{bmatrix} = \begin{bmatrix} 1 & 0 \\ \frac{1}{\sqrt{3}} & \frac{2}{\sqrt{3}} \end{bmatrix} \begin{bmatrix} I_a \\ I_b \end{bmatrix} \tag{4.30}$$

The inverse transformation is given by:

$$\begin{bmatrix} X_a \\ X_b \\ X_c \end{bmatrix} = \begin{bmatrix} 1 & 0 \\ -\frac{1}{2} & \frac{\sqrt{3}}{2} \\ \frac{1}{2} & -\frac{\sqrt{3}}{2} \end{bmatrix} \begin{bmatrix} X_\alpha \\ X_\beta \end{bmatrix} \tag{4.31}$$

The $\alpha\beta\gamma$ space and the Clark Transformation are conceptually similar to a Direct-Quadrature (DQ) coordinate system, with the $\alpha\beta\gamma$ transformation differing only in that the reference frame does not rotate along with the rotor angle. This was chosen over the DQ transformation because it reduces the complexity of calculatons required on the FPGA. Following discussions of currents and voltages will use the $\alpha\beta$ vector space representation for the purposes of the control loop.

Sensing and Observer

As shown above, three phase voltages and currents can each be determined with two measurements given a balanced three-phase system. During experiments, differential voltage sensors were used to measure the line-to-line voltages $V_a - V_c$ and $V_b - V_c$, and clamp-on current sensors were used to measure I_a and I_b. These sensors were connected to Analog-to-Digital converters on the National Instruments control board, and in software were converted into $\alpha\beta$ quantities.

The $\alpha\beta$ voltage measurements are used to estimate the angular position and speed of the engine, in lieu of Hall sensors or motor shaft encoders to directly measure motor position. This scheme is called Sensorless Motor Control, eponymously referring to the lack of direct sensors of motor position. Instead, an observer is implemented in software to estimate the motor position using measurements of voltage. The observer represents the electrical angle of the motor in cartesian coordinates, as a vector on the unit circle, and updates its position based on new measurements of the voltage. Control commands are derived from the observer in order to generate voltages related to the physical state of the motor, within a reasonable error margin.

The observer can be described as a set of states and update equations. The states are the cartesian coordinates and the angular velocity. The update equations are described by the following equations. First, the voltage measurement is used to generate an error in the measured angle from the observer angle at each timestep, which is calculated by the following equation:

$$\delta\theta = \frac{\vec{V_r}}{\|V_r\|} \cdot \vec{\theta_t} \tag{4.32}$$

where θ_t is the unit tangent vector at the observer position. $\delta\theta$ is the component of the new voltage position in the direction tangent to the observer position, which is a good approximation for the change in angle for small deviations. This is a computationally expensive calculation, primarily due to the division by the magnitude of the measured voltage. An approximation to the magnitude was made using:

$$\|V\| \approx max(|V_x|, |V_y|) + \frac{1}{4}min(|V_x|, |V_y|) \tag{4.33}$$

This drastically reduces the norm calculation overhead, while only incurring a 5% RMS error over the angular domain $[0, 2\pi)$. This is also equivalent to $\frac{3}{4}\|V\|_\infty + \frac{1}{4}\|V\|_1$. The level-set of this norm is shown in Figure 4.7

The observer then updates its internal state based on this angle error. A rotation update is calculated based on both a predictive component incorporating the angular velocity and the angle error, and the angular velocity is updated based on the angle error. Both updates are modulated by scalar gain constants α_1, α_2, chosen empirically to give a sufficienctly fast response.

$$\Delta\theta = \omega_k + \alpha_1 \delta\theta \tag{4.34}$$

$$\omega_{k+1} = \omega_k + \alpha_2 \delta\theta \tag{4.35}$$

where $\Delta\theta$ is the rotation update to be used in the next equation, ω_k is the prior angular velocity, ω_{k+1} is the next angular velocity, $\delta\theta$ is the angle error calculated previously in Equation 4.32, and α_1 and α_2 are the observer gains.

The rotation update from Equation 4.34 is used to update the observer vector via forward integration. A basic method is to use simple Euler integration, as shown in Equation 4.36.

$$\begin{aligned} x_{k+1} &= x_k + \Delta\theta y_k \\ y_{k+1} &= y_k - \Delta\theta x_k \end{aligned} \tag{4.36}$$

However, Euler integration leads to accumulating unbounded error. The Euler method is a poor choice for forward integration in all but the simplest cases, requiring very small step sizes to reduce error. More complicated algorithms are typically used that bound and reduce the integration error drastically, such as Runge-Kutta integration, but at the cost of more calculation overhead. However, since the angular position observer is constrained to a

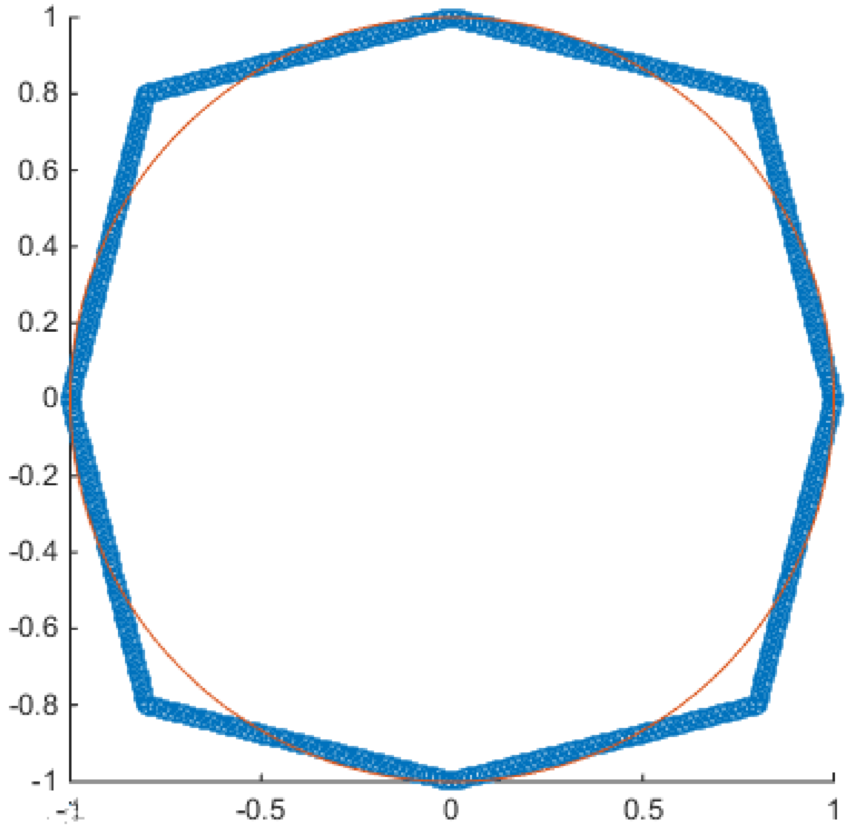

Figure 4.7: The level-set of the custom norm (in blue) compared to a Euclidean $L2$ norm (in red).

circle, a simpler method can be used with almost no impact on computational overhead. The Gauss-Seidel method of integration (also know as Euler-Cromer), shown in Equation 4.37, eliminates the growth of integration error [10]. This is the method that is used to update the observer angular position.

$$\begin{aligned} x_{k+1} &= x_k + \Delta\theta y_k \\ y_{k+1} &= y_k - \Delta\theta x_{k+1} \end{aligned} \tag{4.37}$$

With the observer providing an estimate of the motor/alternator position, the control loop can generate a command that drives the engine as desired.

Controller

The controller is responsible for generating a PWM command to the inverter in order to produce the desired behavior of the engine. It uses the speed estimate from the observer, compared with the desired speed setpoint, to generate a current magnitude command, which is used to generate a voltage command to the inverter. Details of the control algorithm are explained next.

First, the speed control block, shown in Figure 4.8, calculates the error in speed between the observer estimate and the speed setpoint. This error is actually calculated from the difference between the squares of the angular velocities, rather than simple linear subtraction. This was chosen for two reasons: first, it simplifies the controls to be independent of the signs of the observer speed estimate and speed setpoint; second, it matches the physics dimensionally, where rotational energy is proportional to ω^2. It is desirable to control a quantity that is analogous to energy as the resonant control scheme is intended as a control on the energy of the system. The current reference is generated from the speed error by multiplying by a feedback gain, and then scaled from the motor voltage vector in order to command a current in phase with the motor voltage to command unity power factor. The equation for the control is then given by:

$$I_{ref} = \alpha_{speed}(\omega_{set}^2 - \omega_{obs}^2)V_r \tag{4.38}$$

where I_{ref} is the reference current command calculated from this block, α_{speed} is the feedback gain, ω_{set} is the speed setpoint, ω_{obs} is the observer speed estimate, and V_r is the motor voltage. In order to finish the resonant startup mode rotating in the same direction deterministically, the reference current was modulated assymetrically to drive harder in one direction than the other during the startup portion of the control. This ensures that the engine always rotates in the desired direction. This is important, as the direction of rotation dictates the direction of the thermodynamic cycle; i.e. whether the engine operates in generation mode or heat pump mode. The output of this block is the current reference used in the next step.

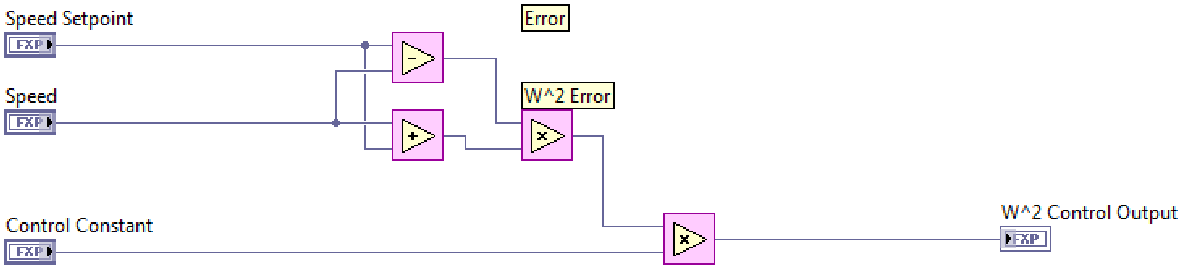

Figure 4.8: Schematic for generating a reference scaling factor based on observer velocity and setpoint.

The reference current I_{ref} is compared to the measured current I and fed into an integrator to obtain the voltage control signal to drive the inverter gates with PWM. This can be expressed as:

$$V_{control} = \alpha_{int} \int (I_{ref} - I_{meas}) \tag{4.39}$$

where $V_{control}$ is the voltage command output, α_{int} is the integrator gain, I_{ref} is the reference current generated in the previous step, and I_{meas} is the measured current. The voltage command is transformed using the inverse $\alpha\beta$ transformation to three-phase voltages and then converted to PWM gate signals to drive the inverter.

A block diagram of the overall control scheme is shown in Figure 4.9, and a full schematic of the control algorithm is shown in Figure 4.10. The control algorithm updated at a frequency of 15 kHz, the same frequency as the PWM algorithm, and synchronized to update on the FPGA at the peak values of the PWM triangle modulator waveform, thereby minimizing the possibility of glitches or additional switching in the middle of a PWM period. The value of the important control constants were first chosen to provide sufficient bandwidth without creating instability, then refined empirically to optimize behavior based on observer fidelity, low current startup, and well-behaved control while running.

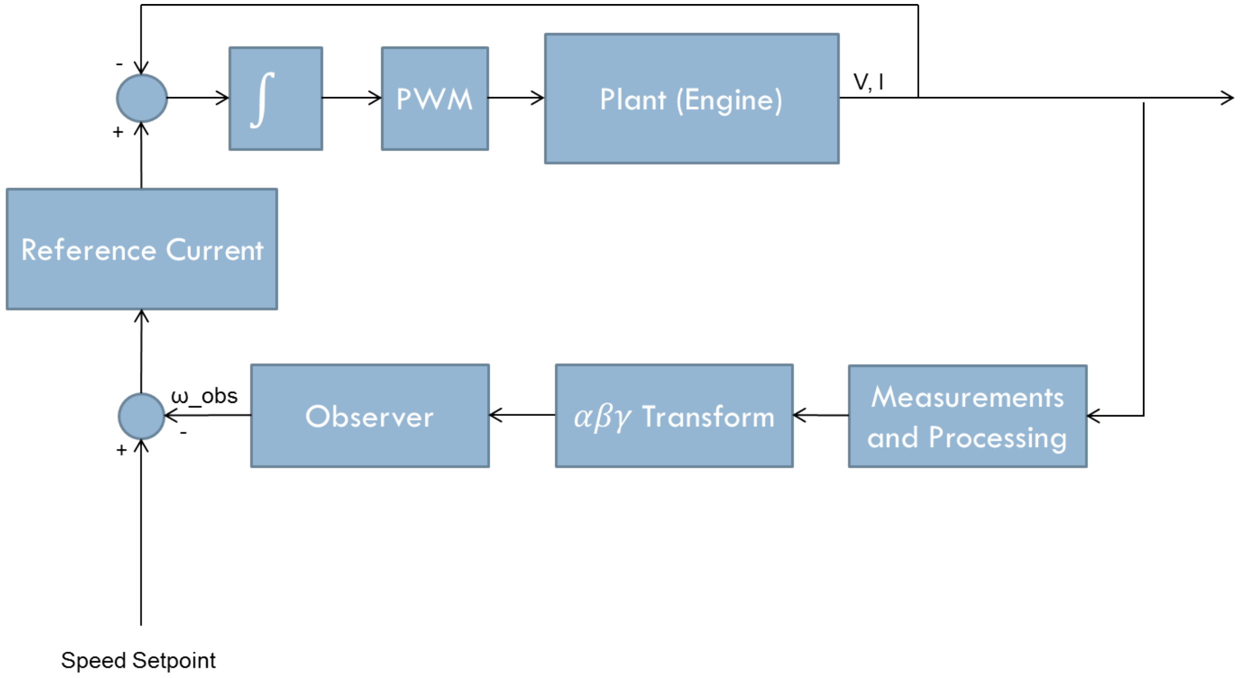

Figure 4.9: Block diagram of the overall control scheme.

This control scheme successfully allowed for a softer resonant startup by injecting energy in phase with the natural resonant motion of the engine during startup. The piston would undergo startup by swinging in one direction, then the other, with the controller injecting energy throughout the process. Once enough kinetic energy was imparted to overcome the compression activation energy, the engine successfully rotated and engaged in normal operation. This same control scheme also worked during normal operation, with the change that the drive command was no longer assymmetrically modulated as was necessary during startup to ensure rotation in the desired direction. The implementation of the this resonant control scheme significantly reduced the startup currents. While previous algorithms commanded upwards of 80 A, resonant startup using this control scheme reduced mean currents to under 10 A, with brief peaks at 20 A.

The software layer above the control algorithm consisted of reading measured and generated data through the FPGA FIFO, displaying and graphing the control front panel interface, and relaying user setpoints and configurations down to the FPGA. This ran on the real-time OS portion of the board in order to save FPGA space, and ran at a signficantly slower speed, at about 10 Hz. An additional service ran on the host computer, which simply logged data continuously to the disk.

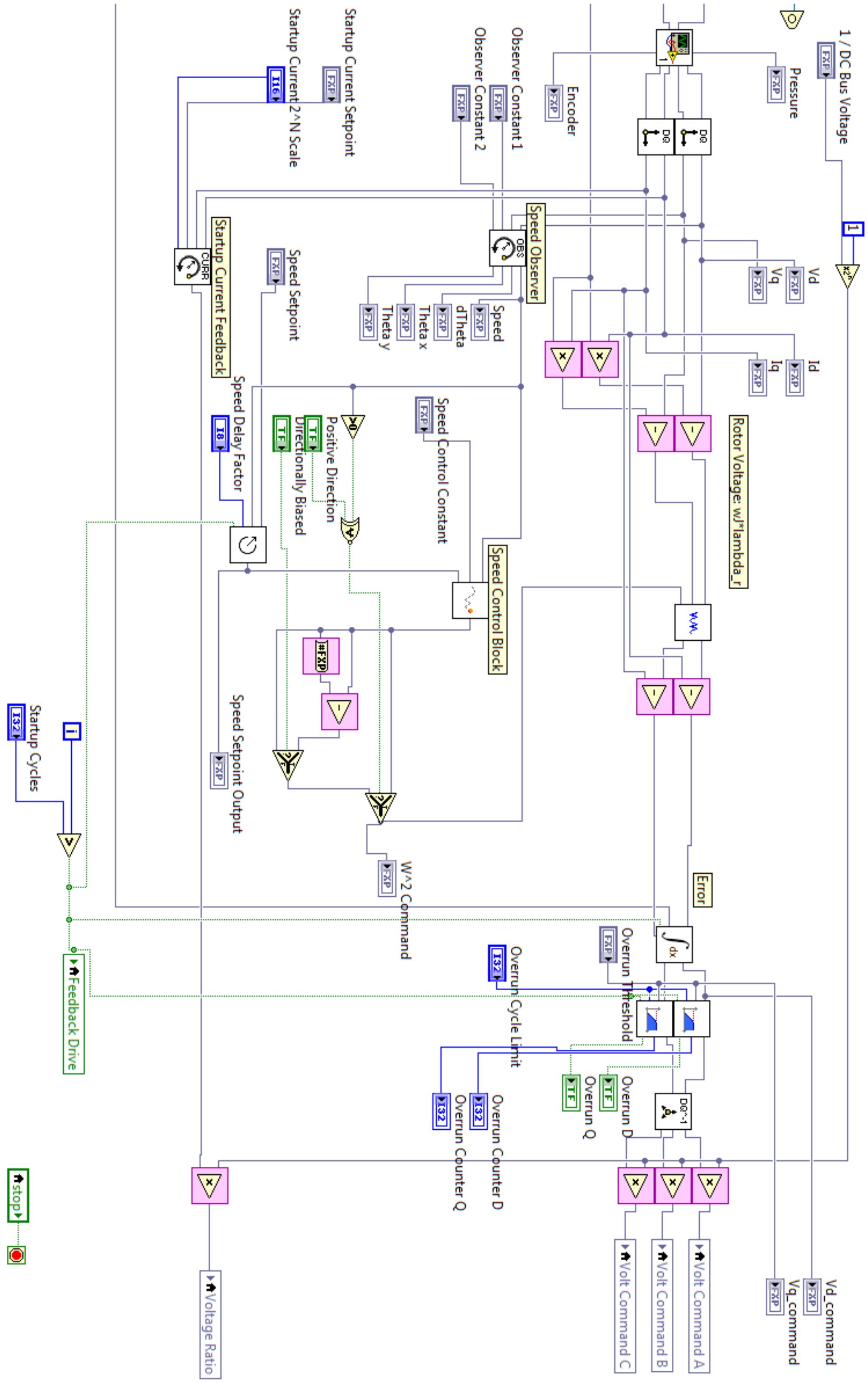

Figure 4.10: Schematic of the overall control scheme.

Chapter 5

Experimental Results

This chapter will discuss the results of various experiments, how the data compares to predictions, and the implications for the Stirling engine system as designed. The experimental stage focused on assessing the performance of heat exchangers and thermal transfer, on quantifying losses in the system, and on quantifying the Stirling cycle behavior of the engine.

Even though this engine was designed with a specific application in mind, the primary purpose of experimentation was to confirm that the design process was accurate and robust, rather than demonstrating a commercially ready engine. A commercially ready prototype has different requirements from a research prototype and would likely require significant changes or additions, in particular to the pressure containment structure, to the fabrication and assembly process of components, and the integration of a solar-heated fluid loop. The same design procedure would be fully appropriate for such a prototype, however, and remains the most important contribution.

The process of testing and experimentation happened over several stages, which will be described in the followings sections. The first stage was assembly and testing of components of the engine to verify correct high-level operation. This required the refinement of several components in order to produce the desired behavior. The next stage was to conduct isolated tests on particular components to confirm particular design predictions. Finally, experiments were conducted with the fully assembled engine of thermal behavior, Stirling cycle heat pump operation, and engine operation.

5.1 Assembly and Verification

After the core engine components were fabricated, assembly and verification were performed to confirm proper operation at a high level. As part of this stage, the assembly procedure for the engine was tested and refined. The assembly procedure was greatly simplified with slight modification or a few components. In brief, the crankshaft and piston components are first assembled together around the cold-side steel plate, which serves as the structural foundation for the rest of the engine. Then heat exchanger and regenerator components are assembled, and the engine is then enclosed by its containment shell and insulated externally. The alternator is then assembled; first the rotor magnet discs are mated together on either-side of the stator, then the rotor is attached to the crankshaft and the stator attached to the cold-side steel plate. Finally, the engine is lifted into the pressure vessel. A series of pictures showing stages of the engine assembly process is given in Figure 5.1.

During this stage, two significant problems were identified. One was intermittent scraping of the displacer piston against its cylinder. This was caused by a combination of higher than specified angular play in the linear sliding bearing of the displacer piston rod, and out-of-spec circularity and flatness in the displacer ring and plates. The latter issue required additional machining to bring the parts into spec. However, the former issue required rethinking of the bearing mechanism for the displacer rod. As mentioned in Chapter 3, a double-bearing housing, incorporating two of the linear sliding bearings along the same axis, was designed to structurally reduce angular play in the displacer piston rod and enforce linear motion. A schematic of the double-bearing housing was shown in Figure 3.15a. The second significant problem was runout in the crankshaft end. This caused large out-of-plane deviation in the spinning magnet disc, causing interference with the stator. This was fixed with a combination of re-machining and by mounting the stator to adjustment bolts to tune its position.

There is a notable difference between the prototype as assembled and a hypothetical commercial system. Due to the constraints of lab experimentation, the hot side external fluid loop could not be implemented to provide the full quantity of heat, which would have required a significant boiler. Instead, electric heating was installed on the hot side as a proxy for whatever heat source would be present in an actual application, as shown in Figure 5.2. This greatly simplified the construction of the experimental apparatus, as well as allowed for much more accurate measurements of input thermal power. The characterization of the engine thermal performance is still complete, except for the hot-side external fluid-to-metal component. However, this component of hardware is identical to the cold-side, whose characterization serves as a reasonable proxy. Identical equations are used in the design of both cold-side and hot-side versions, so verication on the cold-side serves to validate the model nonetheless.

5.2 Heat Exchanger Test

The heat exchangers represent one of the most important components in the engine. As such, a number of tests were conducted to verify their performance. The important properties to test were the external fluid to body heat transfer, heat transfer through the body, and body to working fluid heat transfer.

The first type of experiment tested the heat transfer through the body and through the mesh. Heating elements were applied to the external face of the heat exchanger, with an applied heating power of 500 W, and thermocouples were placed throughout the heat exchanger structure. Temperature drops were measured throughout the heating transient. This test was repeated twice. The results of the test are compiled in Table 5.1. This table

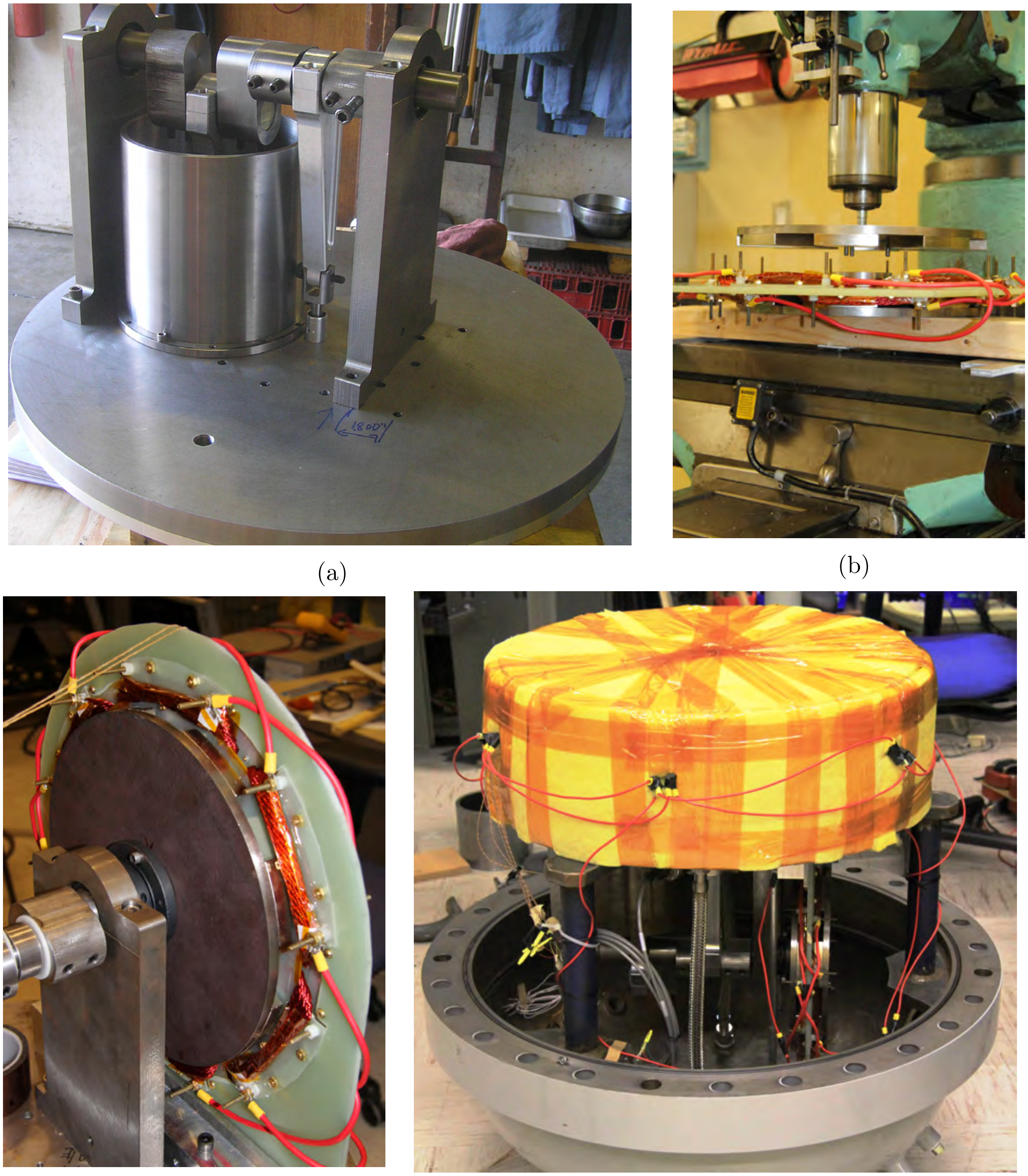

(a) (b)

(c) (d)

Figure 5.1: Pictures of the engine assembly procedure in several stages. (a) shows the engine assembled with crankshaft and pistons. (b) shows the assembly of the magnet rotor discs around the stator using a drill press. (c) shows the alternator assembled on the end of the crankshaft. (d) shows the engine fully assembled.

Figure 5.2: The electric heater assembly is shown here, bolted against the external side of the hot-side heat exchanger.

Component	Average Temperature Drop
External face to internal channel ridge	0.12 K
Mesh contact ridge to mesh interior	0.10 K

Table 5.1: Heat exchanger body and mesh conduction temperature drops.

shows two temperature drops: first, the temperature drops from the surface in contact with the external fluid to the ridge on the internal side of the heat exchanger that contacts the mesh; second, the temperature drop from where the mesh contacts the heat exchanger body to the center of working fluid flux region. This test confirmed that these temperature drops, which were predicted to be small but difficult to precisely calculate due to the high variance based on empirical conditions, were in fact appropriately small.

A second thermal experiment tested the full path of heat flux with the engine entirely assembled. During this test, electric heating was applied at the hot-side external face, while the cooling fluid loop was running at the cold-side. The engine was not in motion during this test. The thermal heating transient was recorded, along with the equilibrium stabiliation temperature profile through the engine, and the cooldown transient was also recorded. This allows characterization of thermal properties in the context of the assembled engine. In particular, this test quantifies static leakage heat fluxes in the engine, including heat conduction losses, heat transfer to the external fluid, and losses to the pressure vessel

Component	Heat Flux	Temperature Drop
Total Input Power	2183 W	
Cold-Side External Fluid	1873 W	0.30 °C
Losses to Vessel Ambient	310 W	144 °C
Engine Internal Cylinder	223 W	143.1 °C

Table 5.2: Heat exchanger temperature drops.

environment. Results from this experiment at thermal equilibrium are compiled in Table 5.2.

The total input power was measured by calculating the electrical input power to the heaters. The heat flux into the cold-side external fluid was obtained by measuring the temperature drop between the inlet and outlet, and multiplying by the heat capacity flow rate of the fluid. The losses to ambient were calculated as the difference between these two heat fluxes. The engine internal cylinder temperature drop was calculated as the difference in measured temperature between thermocouples contacting the internal cylinder at the hot side and cold side, and the heat flux was calculated from the temperature drop by modeling the internal cylinder as a thermal resistance due to conduction. This heat flux is included in the heat flux to the cold-side external fluid, as the heat loss is still delivered to the cold-side fluid. This test confirms that the engine behaves as designed with respect to static heat fluxes, most importantly in two ways. First, that the cold-side fluid heat exchanger properly cools the engine, as evidenced by a 2.3 °C temperature drop from the heat exchanger metal to the fluid, compared to a predicted 2.6 °C temperature drop. Second, that conduction losses through the engine are isolated to the predicted paths such as the internal cylinder, and that there are no other unexpected non-negligible thermal leakage paths. This is evidenced by the internal cylinder maintaining nearly the full temperature differential (174.7 °C to 32.3 °C) under equilibrium.

A third thermal experiment was performed in conjunction with the heat pump and generation tests, to be fully described later. This test differs from the prior tests primarily in that it is testing for oscillatory thermal behavior rather than static thermal behavior. This allows verification of the mesh-to-air heat transfer characteristic, which is the most significant component of the heat exchanger's overall performance. This test incorporated a heating transient, equilibrium measurements, and a cooldown transient. The most direct measurement of the mesh-to-air heat transfer performance is the equilibrium measurement. In this measurement, the temperature drop from the mesh to air was measured to be 1.5 °C, while the design value under these operating conditions was 3.1 °C. The improvement of the measured value over the design value is most likely simply due to the fact that the most conservative empirical model of mesh-to-air heat transfer was chosen as the basis for design. The experimentally measured values and design values are listed in Table 5.3.

By combining the results of these three tests, an overall characterization of the heat

Mesh-to-Air Property	Measurement	Design
Hot-side Temperature Drop	1.7 °C	3.1 °C
Cold-side Temperature Drop	1.5 °C	2.7 °C

Table 5.3: Heat exchanger temperature drops after reaching equilibrium during heat pump test.

Heat Exchanger Property	Measurement	Design
External fluid to body resistance	1.66×10^{-4} °C/W	1.75×10^{-4} °C/W
Body path	6.1×10^{-5}	5.51×10^{-5} °C/W
Body to mesh (longest path)	4.2×10^{-5} °C/W	3.97×10^{-5} °C/W
Mesh to working fluid (Hot side)	2.70×10^{-4} °C/W	2.70×10^{-4} °C/W
Mesh to working fluid (Cold side)	1.5×10^{-4} °C/W	2.33×10^{-4} °C/W

Table 5.4: Heat exchanger temperature drops after reaching equilibrium during heat pump test.

transfer properties of the heat exchangers can be made. A table listing the measured values versus the design values is given in Table 5.4.

5.3 Alternator Performance

The alternator was also tested and compared to predictions from the design process. The most important performance characteristics to be determined are the efficiency of the alternator, and the harmonic content of its associated waveform. The efficiency of the alternator is affected primarily by the electrical resistance of the windings. As previously discussed in Chapter 4, back-iron losses are neglibile, and eddy losses and windage are orders of magnitude less than resistive loss and accordingly difficult to measure. The design resistance of the windings was 249 mΩ per phase, while the measured resistance was 240 mΩ per phase.

The EMF waveform of the alternator was predicted in the design phase with flux data from FEA combined with a winding model and simulation. This waveform can be compared to the actual measured waveform in the time domain and frequency domain.

5.4 Loss Experiments

Measuring the losses or deviations from ideality in the engine is a highly important part of engine characterization. There are a variety of different loss mechanism, detailed in

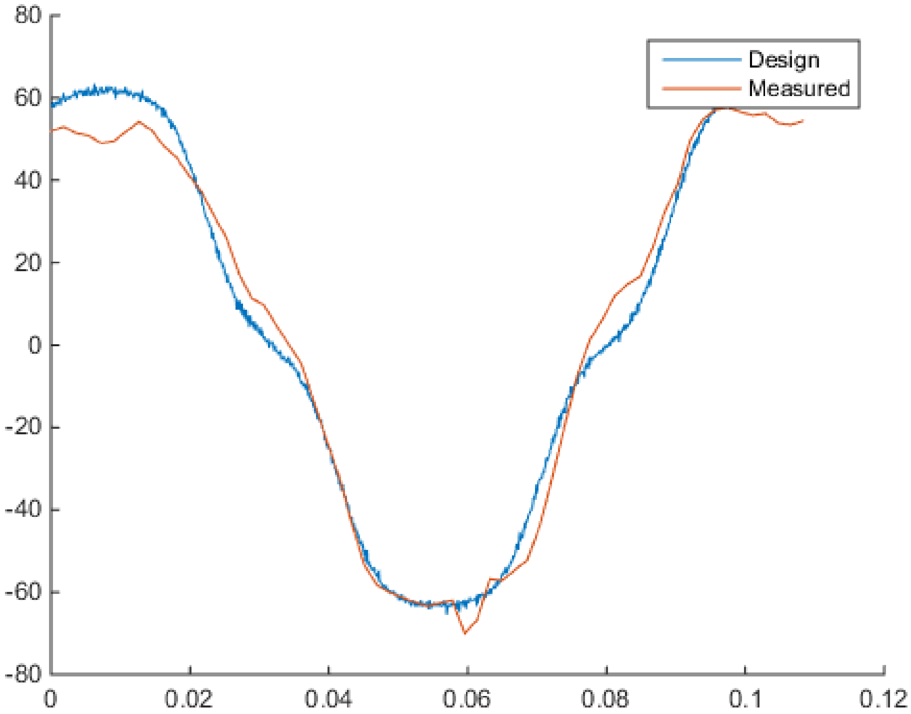

Figure 5.3: Plots of the motor back EMF as predicted during the design phase versus measured during tests.

Chapter 3, each of which require different experiments or methods of discernment. Since many of these losses are small, measurement in these cases can only accurately verify that they fall within the bounds of expectation, which is in itself a valuable exercise for the purposes of evaluating the Stirling engine design process.

A number of the losses only occur in the engine when it is actually operating. These include flow frictional losses in the mesh, air-channel frictional losses, displacer and power piston running losses. To separate and independently characterize these operating losses, a series of experiments was performed with the engine driven by the alternator, with components installed or removed in successive tests in order to isolate their effects. The change in power required to drive the engine therefore indicates the loss value of the change in installed componentry. The baseline was established by measuring driving power with only the alternator and crankshaft, without any additional components. This allows measurement of a baseline level of operating losses in the engine - that of the crankshaft bearings and motion. Subsequent tests measured various combination of installed components, which are detailed in Figure 5.4.

These tests were all performed at full pressurization at 30 bar and full frequency at 20 Hz, the only exception was the Compression Test which was performed at 16.2 bar and full

Baseline Test - Crankshaft only - Measures bearing losses and crankshaft drag loss

Displacer Test - Crankshaft and displacer piston - Measures displacer flow friction loss compared to baseline

Heat Exchanger Test - Crankshaft, displacer, and 1x heat exchanger - Measures single heat exchanger flow friction loss compared to Displacer Test

Regenerator Test - Crankshaft, displacer, 1x heat exchanger, and regenerator, partial enclosure - Measures regenerator flow friction loss compared to Heat Exchanger Test

Power Piston Test - Crankshaft and power piston - Measures Power Piston flow friction and bearing loss compared to Baseline Test

Full Heat Exchanger Test - Crankshaft, displacer, both heat exchangers, regenerator, full enclosure - Measures and confirms heat exchanger loss compared to Regenerator Test

Compression Test - Crankshaft, power piston, both heat exchangers, regenerator, full enclosure - Measures compression loss compared to Full Heat Exchanger Test.

Figure 5.4: Descriptions of the spinning loss tests, the installed components in each test, and the marginal loss component gleaned from each test.

Loss Component	Measured Loss	Predicted Loss
Bearing and Crankshaft Loss	3.9 W	<10 W
Displacer Flow Friction Loss	12.3 W	<20 W
Heat Exchanger Flow Friction Loss	61 W	24.7 W
Regenerator Flow Friction Loss	102.5 W	115 W
Power Piston Flow Friction Loss	22.4 W	<50 W
Compression Loss	72 W	54.7 W

Table 5.5: Measured and predicted spinning losses for various loss components, with the experiments described in Figure 5.4

frequency, and compared to repeated versions of the other tests under the same conditions in order to isolate the compression loss. By subtracting the losses from these tests and attritbuting the difference to the effect of specific components, individual component losses can be disaggregated. These disaggregated loss measurements from these tests are listed in Table 5.5.

A few important comments should be made regarding the losses presented in Table 5.5.

First, certain losses could not be determined precisely during the design process. These are chiefly due to the difficulty in calculating bearing losses, which can vary based on minute details or features in the fabrication or assembly process. Instead, these bearing losses had upper bounds that were estimated in accordance with conservative empirical formula. The results show that measured bearing losses were indeed within the bounds given.

Second, most measured losses matched their design values. This validates much of the design effort to quantify and account for losses. However, the mesh flow friction loss stands out as being signficantly greater in measurement than in design. This discrepancy is not entirely unforeseen. During design, the calculation of this loss is made assuming uniform flow throughout the mesh. However, this is not entirely accurate, as higher flow occurs closer to the displacer piston, both in the air channel and through the mesh. These areas of higher flow generate greater losses than the reduction in losses elsewhere due to lower flow rate, due to the quadratic scaling of flow loss with velocity. The total effect is to increase the losses from this component. This effect cannot be easily accounted for, however, without incorporating fluid dynamics modeling into the loss calculation. A second unaccounted effect is due to the fact that the design analysis for mesh flow friction loss assumes uniformity in the structure of the mesh. In the actual assembly of the mesh in the heat exchanger, non-uniformity can occur due to differing fiber alignment between layers. This introduces additional flow frictional loss, as the working fluid is impeded in moving through layers of fiber. For a more accurate design, fluid simulations could be incorporated into the design process.

The sum total of these spinning losses, however, remains close to design predictions. This indicates that the design process for losses at least represents a reasonable estimate of actual performance.

5.5 Forward and Reverse Operation

The most complete experiments for verification of the design were performed by running the fully assembled engine in forward and reverse directions, which respectively correspond to heat pump and generation modes. These tests fully engage the Stirling cycle conversion of the engine, static losses, and spinning losses. Running in heat pump mode requires input power to move heat from the cold side to the hot side, while running in generation mode converts heat moving from the hot side to the cold side into output work. The two modes are thus inverses of each other and complimentary. The experiment was designed to take advantage of this and exercise both modes throughout a single test. First, the engine was driven in heat pump mode to build up a reservoir of heat at the hot side; then it was started in the forward direction to move the stored heat back from the hot side to the cold side. This dual-mode procedure is also how the engine could be used in a thermal-electric energy storage system.

During this phase of testing, driving the engine at full pressuriation was a significant challenge. The current required for starting up the engine taxed the drive hardware, sometimes exceeding the ratings of the IGBT modules and causing failures. After repeated stress from startup, the displacer piston began to scrape the internal cylinder, limiting the ability to test at higher power. As a result, the heat pump and generation tests were conducted at half pressurization and half-frequency, at 16.2 bar and 9.6 Hz. Even though this was not at the full-rating of the engine, this still allows complete measurement and characterization of the engine, and the design performance was re-evaluated at exactly these conditions for an experimental comparison.

In evaluating the full operation of the engine, one of the most useful metrics is the P-V curve. The P-V curve that the engine traces through represents the action of the Stirling Cycle, and comparison with the simulated P-V curve is a useful qualification of the model. The area within the curve is per-cycle work developed by the Stirling Cycle, as predicted by the adiabatic simulation. The experimental P-V curve is produced from measurements of pressure and extraction of engine volume, which is calculated by an observer looking at the three-phase electrical vector, in conjunction with a once-around encoder to align with mechanical phase angle and synchronize on every cycle. The pressure was measured with a Honeywell A-5 Mid 100 psi -range gauge, which is a differential transducer measuring between the engine internal pressure and the pressure vessel ambient pressure. The engine volumes were calculated by using the observer estimate of the electrical angle, and then using the once-around encoder, which was positioned to correspond to the zero-crossings in the first phase. This allows extraction of the mechanical angle, and therefore the engine volume, which is well-defined the by rigid pistons. Selected time-domain waveforms of the pressure, encoder, voltages and currents are displayed in Figure 5.5.

Combining the measured pressure and volume into a P-V diagram provides insight into the thermodynamic behavior of the engine. Comparing to the simulated P-V diagram offers a high degree of validation of the model and adiabatic dynamic simulation of the engine, and also offers insight into the performance of the engine. P-V diagrams of the engine operating in forward (generation) mode are shown in Figure 5.7, and P-V diagrams of the engine operating in reverse (heat pump) mode are shown in Figure 5.6. The graphs show both the measured P-V trajectory as a scatter plot as well as the simulated P-V trajectory at the operating conditions of the test.

As seen in Figure 5.7 and 5.6, there is agreement between experimentally derived P-V curves and the predicted curves from the Stirling engine model and simulation. The set of P-V curves shows a variation over temperature differential that is predicted by the simulation. At lower temperatures differentials, the P-V curve is narrower since there is less developed work in each cycle of the engine. The noise in the measured P-V curve is due to a combination of sensor noise in the pressure, voltage, and encoder sensors, numerical errors in analog to digital conversion, and errors in the observer estimating the engine position. At lower temperature differential, the signal-to-noise ratio is lower and the measured P-V curve matches less closely to the simulated curve.

These experiments enabled comparison of experimentally measured work with predicted work from the design phase. The input electric power to the engine is measured at the electric terminals of the motor/generator, as AC voltages and currents, which together give the electric power flowing into or out of the machine, depending on direction of operation.

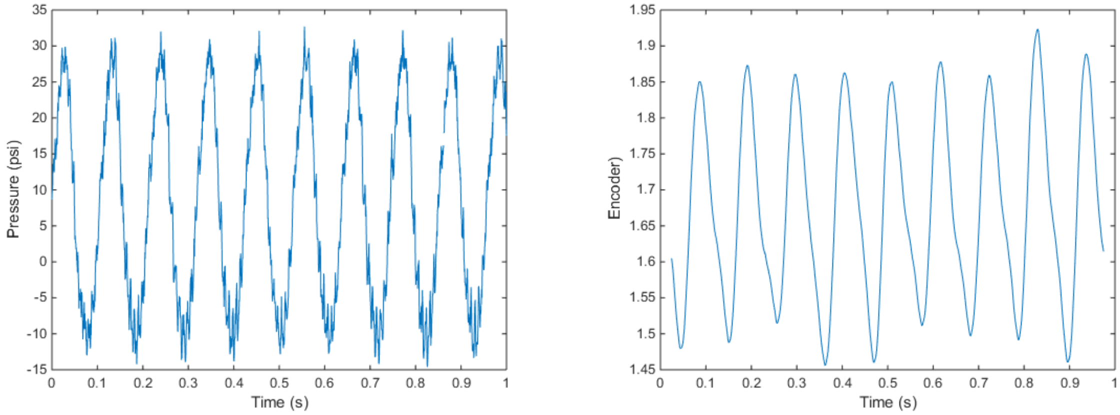

(a) Measured Pressure Waveform (b) Measured Encoder Output (filtered)

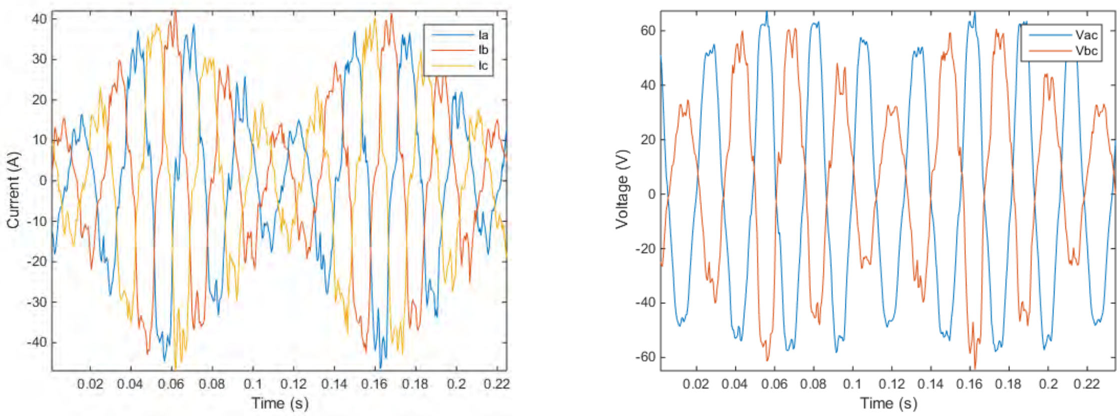

(c) Measured Three-Phase Currents (d) Measured Voltages

Figure 5.5: Representative time-domain waveforms from measurements during engine test

Driving the engine in heat pump mode requires power to overcome losses on top of the power required to power the Stirling cycle engine itself. In other words, the input power required to drive the engine in heat pump mode is the sum of the Stirling cycle work and losses. In generation mode, the power extracted is equal to the Stirling cycle work, minus the same losses. Therefore, engine losses are a burden in both directions. The engine work can be determined in either direction by disaggregating the measured losses, which have been measured in separate experiments. After subtracting these losses, the measured engine work is listed in Table 5.7 and Table 5.6 over different temperature differentials.

The measured Stirling cycle power, disaggregated from losses, matches the prediction values from the design phase over most of the operating points tested. At lower temperature differentials, the measured power values diverge more significantly from predicted values. This is possibly due to greater relative effect of measurement error on the calculated values, as the output work at these operating points has a reduced signal-to-noise ratio.

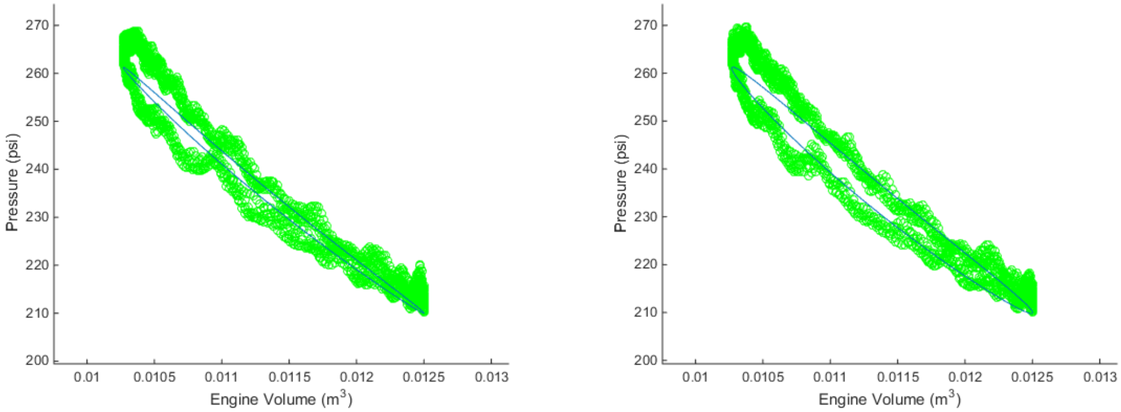

(a) PV diagram with 20 °C temperature differential

(b) PV diagram with 30 °C temperature differential

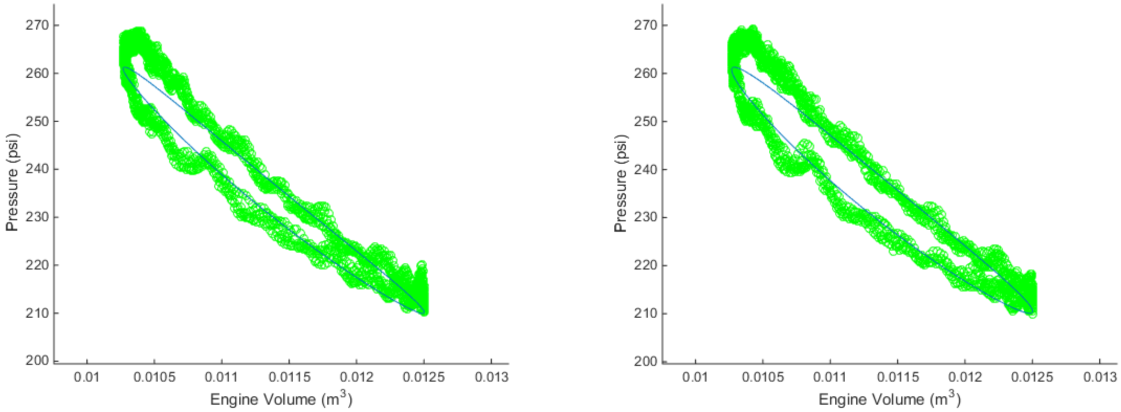

(c) PV diagram with 40 °C temperature differential

(d) PV diagram with 50 °C temperature differential

Figure 5.6: P-V diagrams for heat pump mode are shown with data from measurements plotted together with predicted curves at that operating point, over different operating points of temperature differential.

The measured electrical work at the motor terminals for both heat pump operation and engine operation include mechanical losses. The electrical power in these two modes can be combined for further analysis, as shown in Table 5.8. The difference between electrical power subtracts out losses, which are roughly equal in both modes when at the same operating point, giving a combined power value that is representative of the round trip power level in cycling the engine as an energy storage device.

Since these tests exercise the full operation of the Stirling engine in forward engine mode and reverse heat pump mode, they provide confidence in the methodology presented in Chapter 3 for analyzing, designing, and optimizing the Stirling engine. A shortcoming of

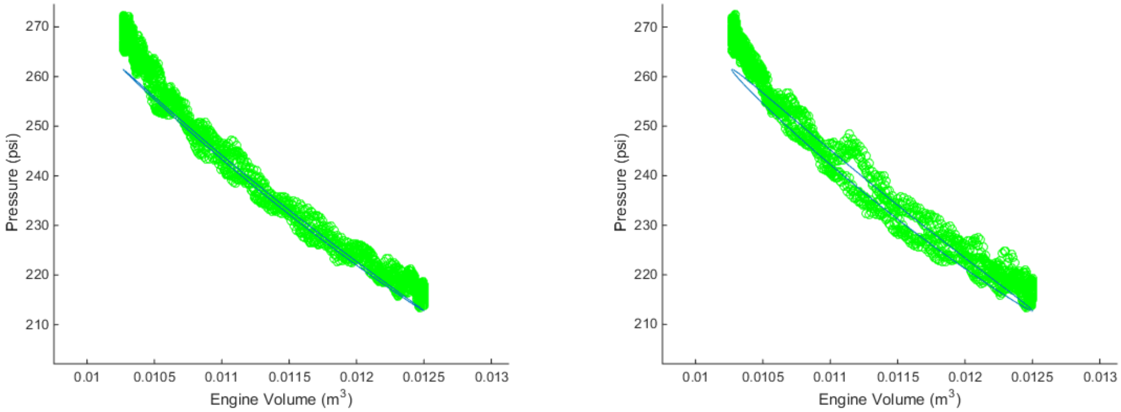

(a) PV diagram with 20 °C temperature differential

(b) PV diagram with 30 °C temperature differential

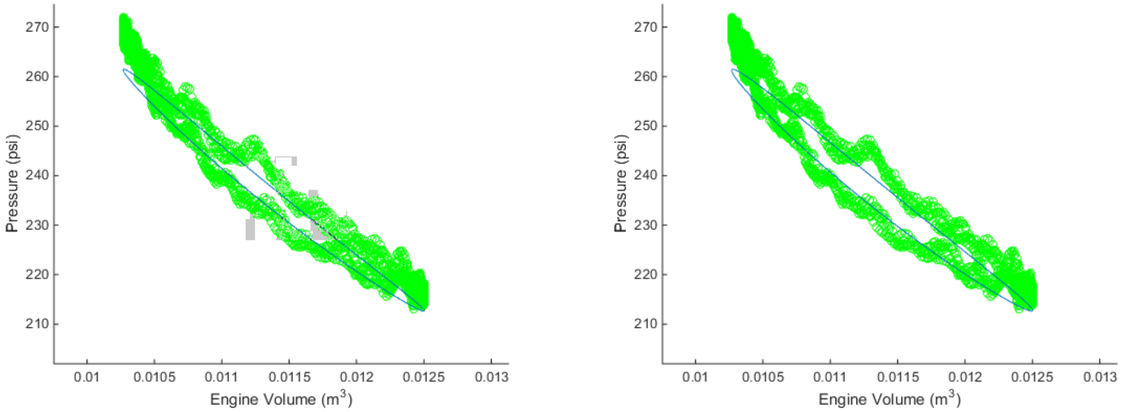

(c) PV diagram with 40 °C temperature differential

(d) PV diagram with 50 °C temperature differential

Figure 5.7: P-V diagrams for engine mode are shown with data from measurements plotted together with predicted curves at that operating point, over different operating points of temperature differential.

these tests is that they were not conducted at the full level of pressuriation and speed that were presumed for the design of the engine. This would require redesign of certain mechanical components or configurations, in particular to lessen the difficulty of startup at high pressure. However, beyond validating the design process, this prototype also provides important lessons for potential changes in mechanical design to address this issue, which will be discussed in Section 6.1.

PV Work in Heat Pump Mode

ΔT	Measured	Predicted
20 °C	80.3 W	120.4 W
30 °C	132.2 W	187.4 W
40 °C	225.1 W	252.2 W
50 °C	325.1 W	317.4 W

Table 5.6: Measured Stirling cycle work during heat pump operation compared to predicted values from the design process.

PV Work in Engine Mode

ΔT	Measured	Predicted
20 °C	37.6 W	45.9 W
30 °C	105.1 W	118.7 W
40 °C	171.2 W	188.9 W
50 °C	244.6 W	253.6 W

Table 5.7: Measured Stirling cycle work during engine operation compared to predicted values from the design process.

Engine and Heat Pump Combined Power

Engine Electrical Power Out	120.2 W
Heat Pump Electrical Power Out	−449.4 W
(Engine - Heat Pump) / 2	284.8 W

Table 5.8: Combined electrical power of heat pump and engine mode at 50 °C

Chapter 6

Conclusion

6.1 Future Work

To continue this research, there are both technical and commercial areas in which future work would be fruitful. In the technical domain, the Stirling engine prototype built could be improved in a number of ways. The startup process was difficult as was described previously, and could be improved simply be changing the neutral resting position of the pistons. The displacer piston design presented repeated mechanical problems, and could be greatly improved with more mechanical engineering attention, in particular with respect to alignment, bearings, and tolerances. The experimental prototype also took liberties with the method of pressurization, enclosing the engine in an external pressure chamber, which simplified the design, but is likely cost-prohibitive. Further engineering to integrate the pressure containment into the engine itself would be necessary to develop a viable commercial model.

In the commercial space, further research is needed into the specific market applications that would be most suited for initial deployment. While the potential addressable market for the technology is large, much of that market is not commercially accessible until the system is further along the cost curve. Identifying the most promising early markets would be of key strategic value. In addition, reducing the cost of certain components in the prototype design, such as the copper mesh material, would greatly improve the commercial viability of the system.

6.2 Final Words

The Stirling engine described in this dissertation points toward the potential for a distributed system that can efficiently and reliably generate renewable electricty combined with heat. The application space for Stirling systems is large, from residential generation in a modern grid setting to microgrids in areas lacking a reliable grid. The combined benefits of electricity generation, energy storage, and heat energy are a attractive combination. The potential for this technology to play a role in decarbonizing humanity's energy portfolio is compelling.

The primary goal of this dissertation is to demonstrate the potential for a Stirling engine system as a clean energy technology and to prove a design methodology that can be used for continued development of such a system. To that end, the design process was proven out in experimental tests as a way to design and optimize a Stirling engine system. The prototype built and tested delivered for the purposes of experimental validation of the design process, and challenges and lessons from this iteration can guide a path forward for future development.

Bibliography

[1] U.S. Energy Information Administration. How much electricity is lost in transmission and distribution in the united states? `http://www.eia.gov/tools/faqs/faq.cfm?id=105&t=3`.

[2] International Energy Agency. International energy agency.

[3] Galen L. Barbose and Naïm Darghouth. Tracking the sun viii: The installed price of residential and non-residential photovoltaic systems in the united states, 2015.

[4] AIT/FIA Information Center. World-wide fuel list, 2012.

[5] McKinsey & Company. Mckinsey on sustainability and resource productivity, 2012.

[6] W.C. Duesterhoeft, Max W. Schulz, and Edith Clarke. Determination of instantaneous currents and voltages by means of alpha, beta, and zero components. *American Institute of Electrical Engineers, Transactions of the*, 70(2):1248–1255, 1951.

[7] Pacific Gas & Electric. Self-generation incentive program, 2016.

[8] Sandra I. Erwin. How much does the pentagon pay for a gallon of gas? *National Defense Magazine*, April 2010.

[9] Alliance for Rural Electrification. Alliance for rural electrification.

[10] Gene H. Golub and Charles F. van Van Loan. *Matrix Computations (Johns Hopkins Studies in Mathematical Sciences)(3rd Edition)*. The Johns Hopkins University Press, 3rd edition, 10 1996.

[11] Mike M. He, Evan M. Reutzel, Xiaofan Jiang, Randy H. Katz, Seth R. Sanders, David E. Culler, and Ken Lutz. An architecture for local energy generation, distribution, and sharing. *IEEE Energy2030 Conference Proceedings*, Nov 17-18 2008.

[12] Caterpillar Inc. Caterpillar diesel generation sets, 2013.

[13] Frank P. Incropera. *Fundamentals of Heat and Mass Transfer*. John Wiley & Sons, 2006.

[14] Jeff St. John. The numbers behind tesla and solarcitys home energy storage play, 2013.

[15] J. Jorgenson, P. Denholm, and M. Mehos. Estimating the value of utility-scale solar technologies in california under a 40 *National Renewable Energy Laboratory*, May 2014.

[16] Aron Kirschner, Roger Chen, Matt Lucas, Sarah Buchwalter, and Shai Ginsburg. Distributed generation from a high-efficiency, low-cost stirling engine, 2012.

[17] Lawrence Livermore National Laboratory. Estimated u.s. energy use in 2012. `https://flowcharts.llnl.gov/`.

[18] Chen Li and G.P. Peterson. The effective thermal conductivity of wire screen. *International Journal of Heat and Mass Transfer*, 49(2122):4095 – 4105, 2006.

[19] H. Lesani M. Sadeghierad, A. Darabi and H. Monsef. Design analysis of high-speed axial-flux generator. *American J. of Engineering and Applied Sciences*, 2008.

[20] Tanaka Makoto, Yamashita Iwao, and Chisaka Fumitake. Flow and heat transfer characteristics of the stirling engine regenerator in an oscillating flow. *JSME international journal*, 33(2):283–289, 05-15 1990.

[21] A. Der Minassians and S. R. Sanders. A magnetically-actuated resonant-displacer free-piston stirling machine. *5th International Energy Conversion Engineering Conference and Exhibit (IECEC)*, June 25-27 2007.

[22] Artin Der Minassians. *Stirling Engines for Low-Temperature Solar-Thermal-Electric Power Generation*. PhD thesis, University of California - Berkeley, 2007.

[23] no one. none. *none*, 2013.

[24] D. Rastler. Electricity energy storage technology options. *Electric Power Research Institute*, December 2010.

[25] D. Rastler. Grid energy storage. *U.S. Department of Energy*, December 2013.

[26] Manol Rekinger and Frauke Thies. Global market outlook for solar power 2015-2019, 2015.

[27] Nancy Skinner. California assembly bill 2514, 2010.

[28] Israel Urieli and D.M. Berchowitz. *Stirling Cycle Engine Analysis*. Adam Hilger, Bristol, UK, 1984.

[29] Jun Xu and R.A. Wirtz. In-plane effective thermal conductivity of plain-weave screen laminates. *Components and Packaging Technologies, IEEE Transactions on*, 25(4):615–620, 2002.